Spring 6-13-2019

Geothermometry of H6 and L6 Chondrites and the Relationship between Impact Processing and Retrograde Metamorphism

Michael Tyler Ream
Portland State University

Geothermometry of H6 and L6 Chondrites and the Relationship between Impact Processing and Retrograde Metamorphism

by

Michael Tyler Ream

A thesis submitted in partial fulfillment of the
requirements for the degree of

Master of Science
in
Geology

Thesis Committee:
Alexander Ruzicka, Chair
Martin Streck
John Bershaw

Portland State University
2019

ABSTRACT

Ordinary chondrites are the most common type of meteorite to fall to Earth and are composed of lithified primitive nebular materials which have experienced variable extents of thermal metamorphism and shock processing. They were subjected to radiogenic heating by incorporation of unstable short-lived radionuclides such as ^{26}Al in the early solar system.

The relationship between metamorphism and impact processing in ordinary chondrites is not fully understood. An unresolved issue in the study of ordinary chondrites is whether their original parent bodies were fragmented by impacts into rubble-pile bodies while they were still hot, or whether they retained their onion-shell structures until they had shed their radiogenic heat. Heat is lost more quickly due to catastrophic impacts because warm material from the interior is exposed directly to the space environment until the impact debris re-accretes into a rubble-pile body, and is then distributed evenly between the surface and the interior of the new rubble-pile body. The extent of retrograde metamorphism possible in ordinary chondrites would therefore largely be dictated by the extent to which their parent bodies were broken up by impacts. Disaggregation caused by an impact would record fast cooling between the temperature at the time of breakup and the temperature at the time of re-accretion.

In this thesis project, five H6-chondrites (Butsura, Estacado, Kernouve, Portales Valley, Queen's Mercy) and five L6-chondrites (Bruderheim, Holbrook, Leedey, Morrow County, Park) were subjected to three different thermometry analyses (pyroxene,

olivine-spinel, and metallographic) to determine their cooling profiles and evaluate whether they are more consistent with onion-shell or rubble-pile thermal models. This study is the first to make use of all three thermometry systems on the same set of samples. Cooling rates for pyroxene and olivine-spinel thermometry systems are determined using the formulation of Dodson (1973) as modified by Ganguly & Tirone (1999). Cooling rates for the metallographic system are determined using the method developed by Wood (1967) as modified by Willis & Goldstein (1981). At temperatures higher than ~600 degrees C, all samples experienced cooling rates which are orders of magnitude faster (100's to 1000's of degrees C/kyr) than what is predicted for onion-shell thermal evolution (10's of degrees C/Myr) by e.g. Monnereau et al. (2013). At temperatures below ~600 degrees C, i.e. those recorded by the metals, cooling rates are much slower in comparison to the silicate/oxide systems, with the exception of Park, which continued to cool quickly. The discrepancy between high- and low-temperature cooling rates for both H- and L-chondrites can best be accounted for by a catastrophic impact which occurred while each body was still near its peak metamorphic temperature, followed by re-accretion into a rubble-pile, which would then cool slowly due to the poor thermal conductivity of rubble-piles. Shock heating does not appear to affect silicate-oxide thermometers.

Acknowledgements

I would like to thank my advisor, Alex Ruzicka, for his patience and insights through all of the many twists and turns encountered in the course of this project. I would also like to thank Rick Hugo for helping me with the SEM's personality swings, my thesis committee members Martin Streck and John Bershaw, and my office mates in S18 for keeping my spirits up.

TABLE OF CONTENTS

LIST OF TABLES

LIST OF FIGURES

CHAPTER 1: INTRODUCTION

Ordinary chondrites

Ordinary chondrites are the most common type of macroscopic extraterrestrial material to fall to Earth, accounting for approximately 85% of all observed falls. They are subdivided into three groups – the H-, L-, and LL-chondrites, which are surmised to originate from different parent bodies based on chemical, mineralogical, and isotopic evidence. The asteroid 6 Hebe is thought to be the H-chondrite parent body, or at least a major fragment of it, due to strong spectral similarities (Gaffey & Gilbert, 1998), though this has recently been disputed (Marset et al., 2017). The Gefion asteroid family has been identified as the probable remains of the L-chondrite parent body (Nesvorny et al., 2009), which may have been catastrophically fragmented sometime during the Ordovician (Keil et al., 1994).

Heating

The presence of abundant short-lived radionuclides in the proto-solar nebula, most notably ^{26}Al ($t_{1/2}$ = 0.717 Myr) and ^{60}Fe ($t_{1/2}$ = 2.6 Myr), and the incorporation of these nuclides into contemporaneously forming mineral species, led to widespread endogenic heating. This heating was intense enough in the earliest stages of planetesimal formation to cause melting, and hence igneous differentiation into a silicate mantle surrounding an iron core, in bodies which had already accreted by this time. The ordinary chondrites were not among this first generation of planetesimals, as they are widely suspected never to have undergone melting due to their quasi-solar

chemical compositions. The H-chondrite parent body may have undergone partial differentiation in its core and produced the IIE iron meteorites (Ruzicka 2014). Peak metamorphic temperatures for ordinary chondrites are in the range ~870-930 degrees Celsius (Slater-Reynolds and McSween 2005, Henke et al., 2012, Monnereau et al., 2013). Melting in the FeNi-FeS system begins in the 900-1000 ^{o}C range (Tomkins 2009). During the first ~2Myr of solar system formation formation, ^{26}Al heating would have been intense enough to melt any accreting bodies of any significant size (Bizzaro et al., 2005, Kleine et al., 2005, Hevey and Sanders, 2006, Kruijer et al., 2012). Chondrule ages suggest that formation of most still-chondritic bodies occurred after this, when ^{26}Al was still abundant enough to cause metamorphism but not large-scale melting (Kita and Ushikubo, 2012, Sanders and Scott, 2012). Timescales of accretion were probably no longer than 0.2 Ma (Monnereau et al., 2013). Thermal models along with radiometric ages are generally in agreement with this broad-scale picture (Trieloff et al., 2003, Henke et al., 2012, 2013, Harrison and Grimm, 2010). Impacts also provided localized heating via intergranular friction of porous material or proximity to impact-derived melts (Rubin 2004).

Metamorphism and petrographic types

The degree to which a chondrite sample has undergone this thermal metamorphism is known as the petrographic type, which ranges from 3 to 6 or sometimes 7 (van Schmus and Wood, 1967). Pristine, unaltered nebular material is assigned to type 3, with type number increasing with increasing metamorphic alteration

(van Schmus and Wood, 1967). Types 1 and 2 are used to denote the extent of hydrothermal alteration, for which there is little evidence in ordinary chondrites and which is primarily used for carbonaceous chondrites. In a body which is not being disrupted by large impacts, higher petrographic types would correlate with greater burial depths, and with slower cooling rates and younger cooling ages. Another possibility is that there were multiple parent bodies (Yomogida and Matsui 1984), which may have experienced different degrees of metamorphism due to different sizes and earlier or later accretion dates, and which also could have been fragmented to varying extents.

There are two contrasting models of the correlation of petrographic type with burial depth within a parent body, the *onion-shell* model (Trieloff et al., 2003; Kleine et al., 2008; Harrison and Grimm, 2010; Monnereau et al., 2013), and the *rubble-pile* model (Scott and Rajan, 1981; Taylor et al., 1987; Williams et al., 2000; Scott et al., 2014), shown schematically in fig. 1 (Scott & Rajan 1981).

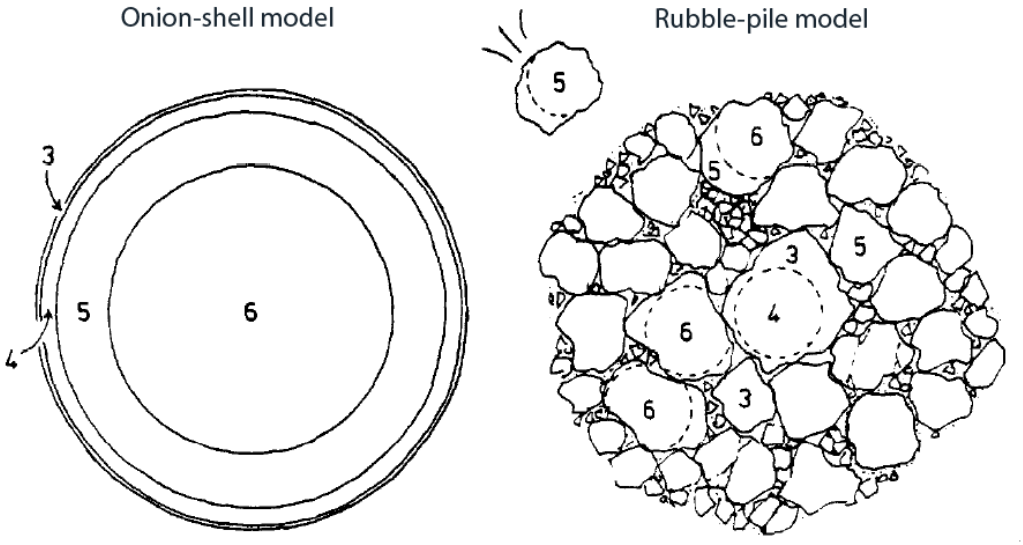

Figure 1. From Scott & Rajan 1981, Figure 11 in that paper. Schematic contrast between the onion-shell and rubble-pile models. The numbers denote petrographic type.

ONION-SHELL MODEL

In the onion-shell model, there is an inverse relationship between petrographic type (which can then be used as a proxy for burial depth) and cooling rate, since heat loss is progressively more inhibited by overburden at greater depths (e.g., Scott & Rajan, 1981). The concept central to the simple onion-shell model is the preservation of this metamorphic stratification throughout the entire asteroid (e.g., Harrison and Grimm, 2010; Monnereau et al., 2013).

Trieloff et al., (2003) conducted ^{206}Pb-^{207}Pb, whole-rock ^{40}Ar-^{39}Ar, and ^{244}Pu age analyses on eight unshocked H-chondrite samples, two of which, Estacado and Kernouve (both H6), were also analyzed in this study. Only weakly shocked chondrites were used, in order to avoid any potential interference in the thermometry systems via shock

heating (Trieloff et al., 2003). These ages were all found to be younger with increasing petrographic type, which is consistent with onion-shell cooling (Trieloff et al., 2003). Slower cooling corresponds to younger ages in such systems because of the longer time necessary to cool to that system's closure temperature (Trieloff et al., 2003).

^{182}Hf-^{182}W isochrons measured by Kleine et al. (2008) show a similar decrease in age with increasing petrographic type (Kleine et al., 2008). Modeling of W closure temperatures (i.e. the temperature below which diffusion has effectively ceased; explained in detail in following chapters) in clinopyroxene produced a closure temperature of 875(±75) ^{o}C for H6 chondrites Kernouve and Estacado (Kleine et al., 2008). These temperatures were found as a function of grain size and cooling rate using the Dodson (1973) formulation (Kleine et al., 2008). They found that clinopyroxene cooling rates of ~10 ^{o}C/Myr were most consistent for H6 chondrites with grain size ranges of 5-30 µm (Kleine et al., 2008). This is close enough to the peak temperature of ~950 C that it is either effectively dating the time that cooling from peak heating commenced, or that the body remained at its peak temperature for long enough for grain coarsening to increase the closure temperature, or Tc, of the ^{182}Hf-^{182}W system to the contemporaneous temperature before cooling actually started (Kleine et al., 2008).

Type 6 material also could have been excavated to the surface without necessarily scrambling an onion-shell structure (Harrison and Grimm 2010). Material affected by impacts could cool more rapidly than it otherwise would, either by

excavation to the surface in an ejecta blanket or simply by closer proximity to the surface because of overburden reduction (Ciesla et al., 2013).

Modeling of onion-shell thermal evolution

Early onion-shell thermal evolution models such as Miyamoto et al. (1981) were able to reproduce the approximate proportions of different petrographic types found in meteorite falls but were inconclusive regarding slower metallographic cooling rates observed in lower petrographic types by Wood (1967). Harrison and Grimm (2010) were able to construct an onion-shell cooling model which was consistent with data gathered from elsewhere in the literature, including ^{206}Pb-^{207}Pb, ^{40}Ar-^{39}Ar, and modeled ^{182}Hf-^{182}W age data and olivine-spinel, metallographic, and ^{244}Pu fission-track cooling rate data. They noted that regolith metal grains may simply be cooled by comminution and not reflect transport from a deeper interior, and hence may not hold any relevance to global-scale thermal history. They did not use any information about high-temperature cooling rates except those taken from Kleine et al. (2008) and Kessel et al. (2007). For Kernouve (H6) and Estacado (H6), the two samples which this study and Harrison and Grimm (2010) have in common, their model predicts cooling rates of approximately 50 ^{o}C/Ma through a temperature of approximately 800 ^{o}C. They did not incorporate any pyroxene data.

Insulating effect of regolith

The thermal conductivity of loose regolith is much lower than for rocky, consolidated material (Luan and Goldreich 2015). In an onion-shell body, the slower escape of heat from the interior would result in a restriction of lower petrographic types towards the surface of the body, which would be composed mostly of type 6 rock. This would allow for type 6 material to be excavated by impacts more easily due to its proximity to the surface. However, the modelled burial depths for the H6 samples Estacado and Guarena are still too great, even in the presence of regolith, for their parent body to have survived an impact capable of excavating them (Monnereau et al., 2013).

RUBBLE-PILE MODEL

Impact disruption

Impacts between objects were ubiquitous in the early solar system, many of them catastrophic (Bottke et al., 2005). It seems unlikely that such large bodies would have been able to avoid at least a few major collisions with other bodies of comparable size or of large enough relative velocity that would result in large-scale excavation of buried material or even total disaggregation of the asteroid (Taylor et al., 1987; Williams et al., 2000; Scott & Rajan, 1981). Kleine et al. (2008) acknowledge that other H-chondrites cooled too quickly at lower temperatures to be consistent with an onion-shell structure and are better explained by impact-related disturbances. This necessarily leads

to consideration of the opposite extreme to the onion-shell model – the rubble-pile model (Scott & Rajan, 1981).

A rubble pile asteroid is one which has been disrupted by a collision and subsequently re-accreted back together by self-gravitation (e.g., Keil et al., 1994; Wilson et al., 1999), such as the asteroid 25143 Itokawa (Fujiwara et al., 2006). Disrupted asteroids/planetesimals do not disperse completely, because not all fragments will achieve escape velocity from the body's center of mass, but rather remain in more or less the same orbital path and eventually re-accrete under their own gravitational self-attraction into rubble pile structures (Taylor et al., 1987). If collisional disruption occurred in an ideal onion-shell asteroid while temperatures were still high, and hence while metamorphic processes were still underway, then cooling rate should lose its dependence on petrographic type if the new distribution of material in the rubble pile was mixed (Scott & Rajan, 1981, Taylor et al., 1987, Williams et al., 2000; Scott et al., 2014). Another possible scenario is the accretion of many small bodies, or planetesimals, from the same nebular source reservoir, which were all previously internally heated to varying extents, which then accrete together themselves in a rubble pile, locally preserving some trace of their original metamorphic stratification (Scott & Rajan, 1981). The planetesimals can also have undergone collisional disruption of their own. The result in this case is effectively a pile of fragments of onion shells.

The lower thermal conductivity of regolith and megaregolith might mean that a rubble-pile undisturbed by subsequent impact disruptions would in fact cool more

slowly than its onion-shell equivalent (Luan & Goldreich, 2015). The thermal conductivity of a rubble pile would be dependent on the surface area of the irregular contacts between the rubble particles, and hence is much less efficient in the absence of interstitial fluids to facilitate conduction (Luan & Goldreich, 2015). Another consideration regarding the influence of regolith on cooling behavior should also account for the "Brazil nut effect", or granular convection segregating large boulders towards the surface, which is suspected to occur in the near-surface regions of rubble-pile asteroids but not the deep interiors (Perera et al., 2016). This would presumably create a thermal lid which traps heat in the rubble-pile interior for longer, thus slowing the cooling even further.

The cooling history of type 6 material in a rubble-pile body would be markedly different than type 6 material in an undisturbed onion-shell, in that heat is lost much more quickly due to exposure of hot material from the interior to the space environment, shown schematically in fig. 2. An onion-shell would cool slowly throughout its history (Monnereau et al., 2013, Harrison and Grimm, 2010), whereas a rubble-pile will cool quickly after its break-up and very slowly once it has accreted back together, shown schematically in fig. 3.

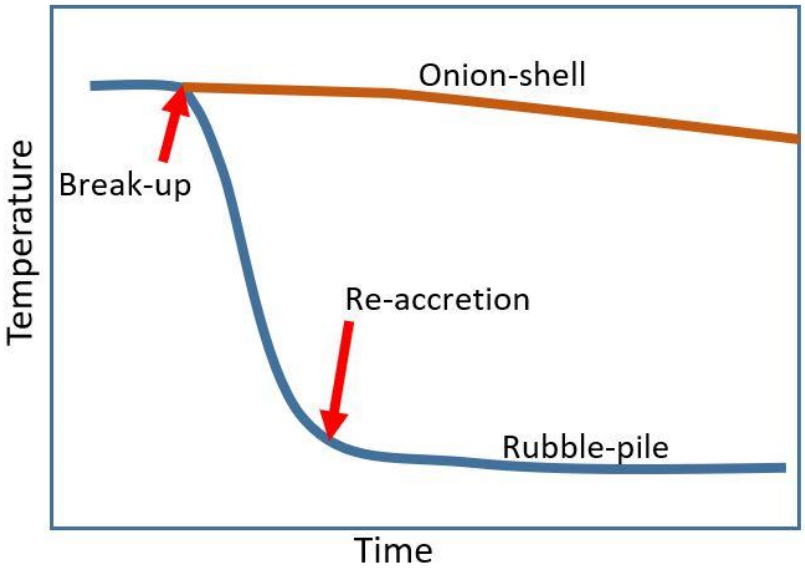

Figure 2. Schematic diagram showing the change in temperature with time for an originally onion-shell parent body which is disaggregated at or near its peak temperature and re-accreted back together into a rubble-pile.

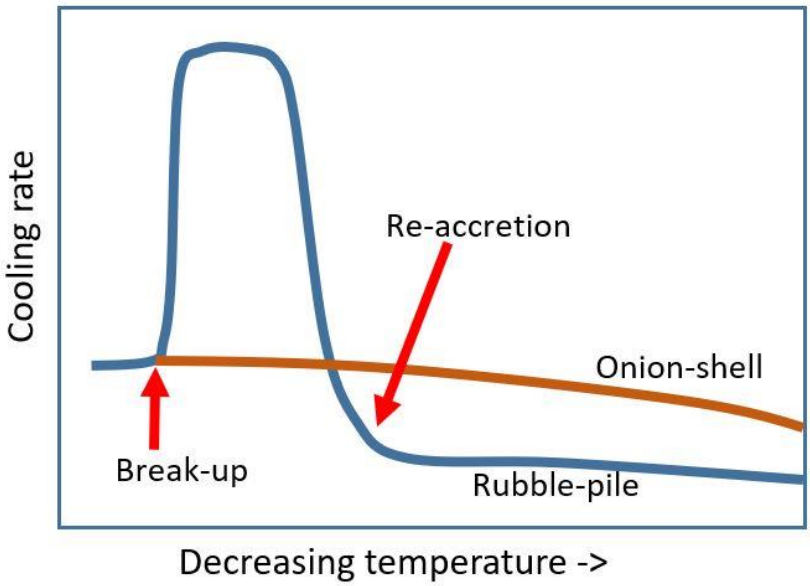

Figure 3. Schematic diagram showing cooling rate behavior through parent-body break-up followed by re-accretion. Cooling is very fast while material is dispersed in space but slows down after re-accretion due to the poor thermal conductivity of loose material in the absence of fluids.

Low bulk densities of asteroids

A large proportion of asteroids have anomalously low bulk densities compared to their mineralogical compositions, a sign that many asteroids have significant macroporosity (Britt et al., 1987), either as rubble piles such as Itokawa (Fujiwara et al., 2006) or as contiguous but heavily fractured bodies in the case of 433 Eros (Wilkinson et al., 2002). Type 5-6 LL-chondrite material is already confirmed to be present on the surface of the rubble-pile asteroid 25143 Itokawa (Nakamura et al., 2011).

Lack of cooling rate/petrographic type correlation

No correlation was previously found between petrographic type and metallographic cooling rate for H, L, or LL chondrites, as shown in fig. 4 (Taylor et al., 1987). This is despite contradictory findings from ^{244}Pu fission track data from H chondrites indicating an onion-shell H chondrite parent body (Pellas 1981, Pellas & Storzer, 1981). However, this may have been due simply to small sample size. Therefore, either the ordinary chondrite parent bodies are re-accreted masses of disrupted, originally onion-shell material, or agglomerations of variably sized and metamorphosed planetesimals which formed from the same nebular source reservoir (Taylor et al., 1987). Breakup and reassembly of onion-shell structures could still have occurred before the system cooled to below ~650 ^{o}C (the temperature at which kamacite begins to coexist with taenite at typical chondritic bulk metal compositions), which is more likely than accretion of planetesimals directly from the nebula according to Grimm (1985), since objects a few meters in size can retain their heat if they quickly clump back

together but not if they have to accrete directly from the nebula, which would take much longer (Grimm 1985). Metallographic cooling rates in Scott et al. (2014) were slightly higher on average for H4's compared to H5's and H6's, and H3's did not have a large enough sample size to define a meaningful average but 2 of the 3 were well within the ranges of the other types. Fig. 5 shows metallographic cooling rate data from the matrix material of regolith breccia sample Cangas de Onis, which contains metal grains spanning a wide range of cooling histories that were mixed on the scale of a single sample (Williams et al., 1985).

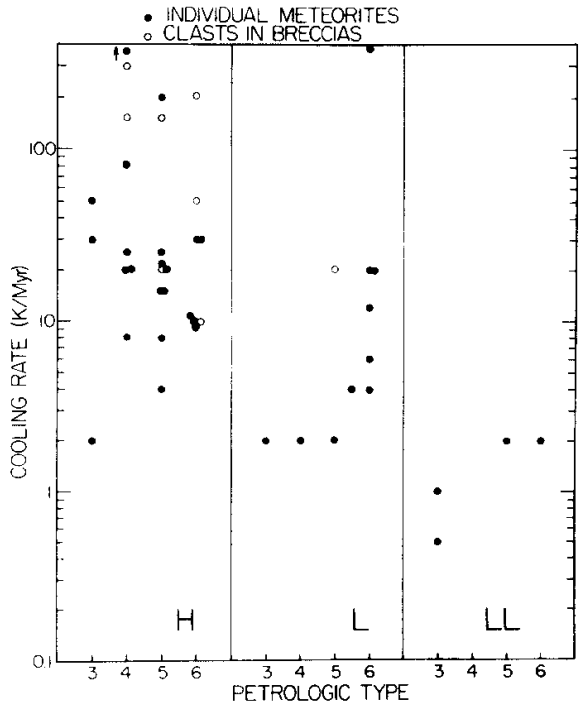

Figure 4. From Taylor et al 1987, fig. 5 in that paper: Showing the lack of correlation between petrographic type and metallographic cooling rate.

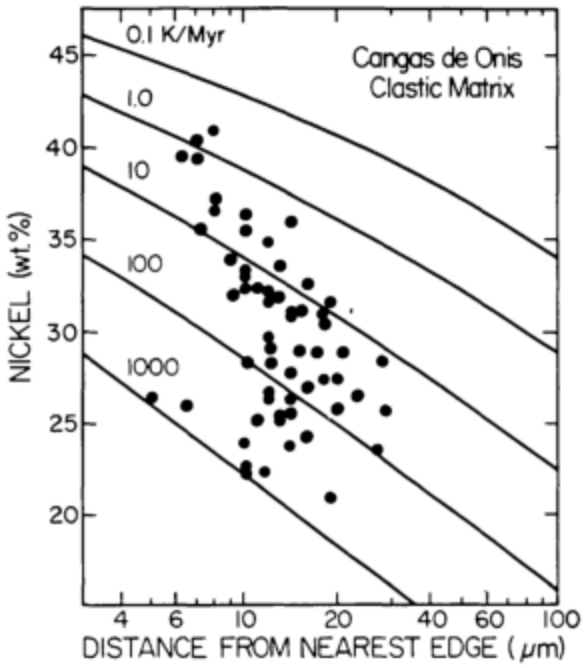

Figure 5. From Williams et al. 1985, fig. 3 in that paper: showing the wide ranges of cooling rates measured from metal grains in the matrix material of the Canga de Onis H-chondrite regolith breccia.

Isotopic evidence for rubble-pile

Excesses of ^{4}He implanted by solar wind beyond what was produced by U and Th decay over 4.5 Gyr of solar system history in many regolith breccias show that material from a wide range of depths must have found its way to the surface, as solar wind penetration depth is generally ~ 1 micron (Taylor et al., 1987). For this to be possible, fragmentation of the host body is necessary, since the burial depths of >40 km of type 6 material calculated by Wood (1967) would create a crater so large (following the conventional lunar depth-to-diameter ratio of 0.2) that it is comparable to the diameter of the body itself, which is implausible (Taylor et al., 1987). Another possible scenario is that one fragment contains a large proportion of the mass of the original object that did

not re-accumulate another regolith layer by subsequent re-accretion (Taylor et al., 1987). A wide range of petrographic types would then be exposed at the newly-excavated surface (Taylor et al., 1987). However, this requires a very specific set of conditions and hence is unlikely (Taylor et al., 1987). Measurable shock effects occur only in close proximity to the site of impact, meaning that disruption-and-reassembly is consistent with large amounts of unshocked material (Stoffler 1982).

Purpose and scope

The scope of this study is to ascertain the cooling histories of the H- and L-chondrite parent bodies through the range ~900 ^{o}C to ~500 ^{o}C, and whether these histories are more consistent with an onion-shell or a rubble pile model during this stage in early solar system evolution. This will serve to place constraints on the development of collisional dynamics in the still-forming solar system. We accomplish this using three thermometry techniques which are valid in different temperature ranges on the same set of samples, which has not previously been done.

The aim of this project is to assess the cooling histories of ordinary chondrite samples through the application of geothermometry and mineral-chemical diffusion models. Since the onion-shell and rubble-pile models predict different distributions of cooling histories for meteorites, by constraining the cooling histories of a sample suite of meteorites, I provide insight into the extent of large-scale collisional processing in the early solar system, and its relationship to endogenic heating.

CHAPTER 2: INSTRUMENTATION AND SAMPLES

SAMPLES

10 polished thin sections were chosen for analysis in this study, five H6-chondrites (Butsura, Estacado, Kernouve, Portales Valley, and Queen's Mercy) and five L6-chondrites (Bruderheim, Holbrook, Leedey, Morrow County, and Park). The specific thin sections used for study are listed in Table 1.

Table 1. Names and thin section numbers of the samples used in this study.

H-Chondrites		L-Chondrites	
Sample Name	Thin Section #	Sample Name	Thin Section #
Butsura	CML 0620-1B	Bruderheim	CML-0618-2B
Estacado	CML 0295-3A	Holbrook	CML 0302-6A
Kernouve	CML 0666-B	Leedey	CML 0504-1A
Portales Valley	CML 0056-3	Morrow County	CML 0497-2B
Queen's Mercy	USNM 1560-2	Park	CML 0617-2A

INSTRUMENTATION

Electron microscopy was performed on the samples using a Zeiss Sigma Field Emission Variable-pressure Scanning Electron Microscope (SEM) with an attached high-efficiency Si drift (XMax50) EDS detector. Accelerating voltages of 15 keV and beam currents of 5-10 nA were used to collect back-scattered electron (BSE) imagery and energy-dispersive spectroscopy (EDS) maps, point analyses, and linescan data. Quantitative chemical data were obtained from point analyses and linescan data by converting count rates to concentrations using energy and beam calibration on a pure Cu

standard and factory quantitative standardizations for elements of interest. Oxygen concentrations were calculated by stoichiometry for all phases except metals.

EDS map images (2048x1536 pixel BSE images, 1024x768 pixel EDS images, together obtained in ~20 minutes) were gathered from locations determined from reflected-light photomosaics in order to determine locations for future spot data acquisition. These photomosaics were obtained using a Leica DM2500 petrographic microscope. Chromite-rich areas were the primary targets for EDS imagery, because sufficient amounts of pyroxenes were found to be already present in these areas. Chromites were located using reflected-light photomosaics of the thin sections which were constructed prior to applying the carbon coat. Clinopyroxenes were too small to detect optically, so EDS maps were necessary to locate them. Once the locations of suitable pyroxene and olivine-chromite pairs were delineated in the EDS images (see figs 6 & 7 for an example), point analyses were gathered from those mineral pairs during a subsequent session. Analytical times of 20 seconds were used for each point analysis. The pairs for which good data was recovered for both mineral phases were used for closure temperature and cooling rate calculations. Analyses with weight percent totals less than 97% or greater than 102% were not used for thermometry calculations. Analyses with cation weight percent, normalized atom percent, and cation oxide weight percent totals were used as appropriate. Atom percent totals were used to calculate stoichiometries when necessary. If different analyses of the same phase have many zero values alongside non-zero values for concentration of a given chemical species, then it is

reasonable to assume that the non-zero amounts are close to the detection limit of the SEM for that species (Ruzicka et al., 2017). An upper limit of concentration might then be defined to be the mean of those values (Ruzicka et al., 2017). Detection limits are estimated to be ~ 0.02 – 0.05 wt% for most elements. Elements which were mostly below the detection limits for the SEM included P, S, K, and Ni in silicates and chromite, Al in olivine, and Ca in chromite.

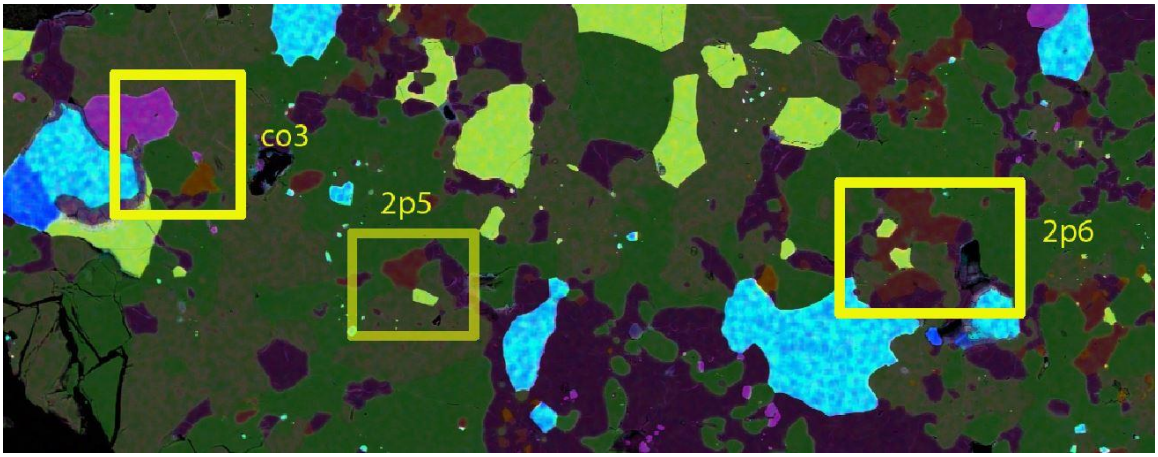

Figure 6. An example of an EDS map (Estacado area 1) showing delineated mineral pairs. "coX" = chromite-olivine pair X, 2pX = pyroxene pair X. Green = olivine, pink = chromite, brownish green = orthopyroxene, dark red = clinopyroxene.

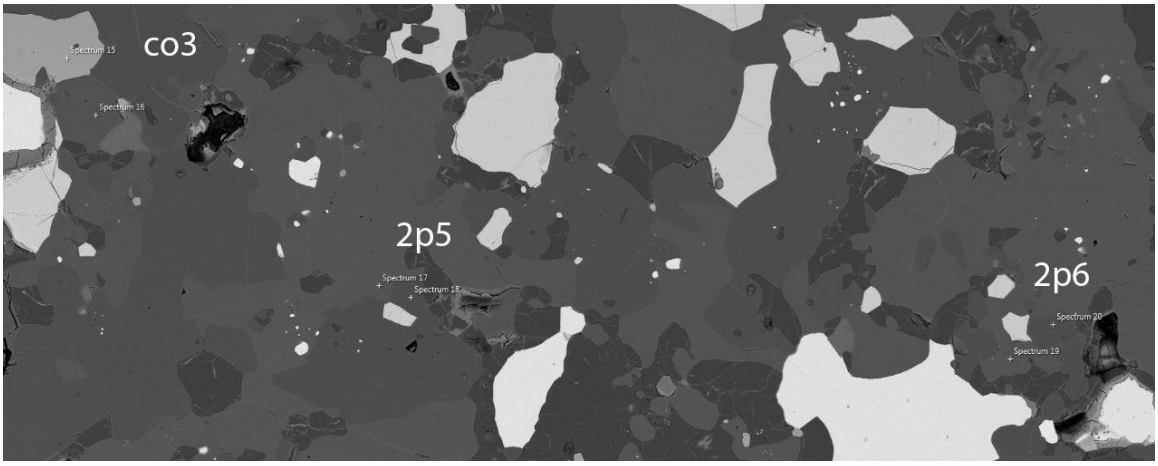

Figure 7. BSE image with spot data for chromite-olivine pair co3 (left) and pyroxene pairs 2p5 (center) and 2p6 (right).

Metal grains were identified in the SEM by changing the image settings to a low (~43%) brightness and a high (~52%) contrast (fig. 8). This would facilitate identification of taenite grains, because taenite has the highest mean atomic number of all the phases found in abundance in chondrites and hence is the brightest in a BSE image.

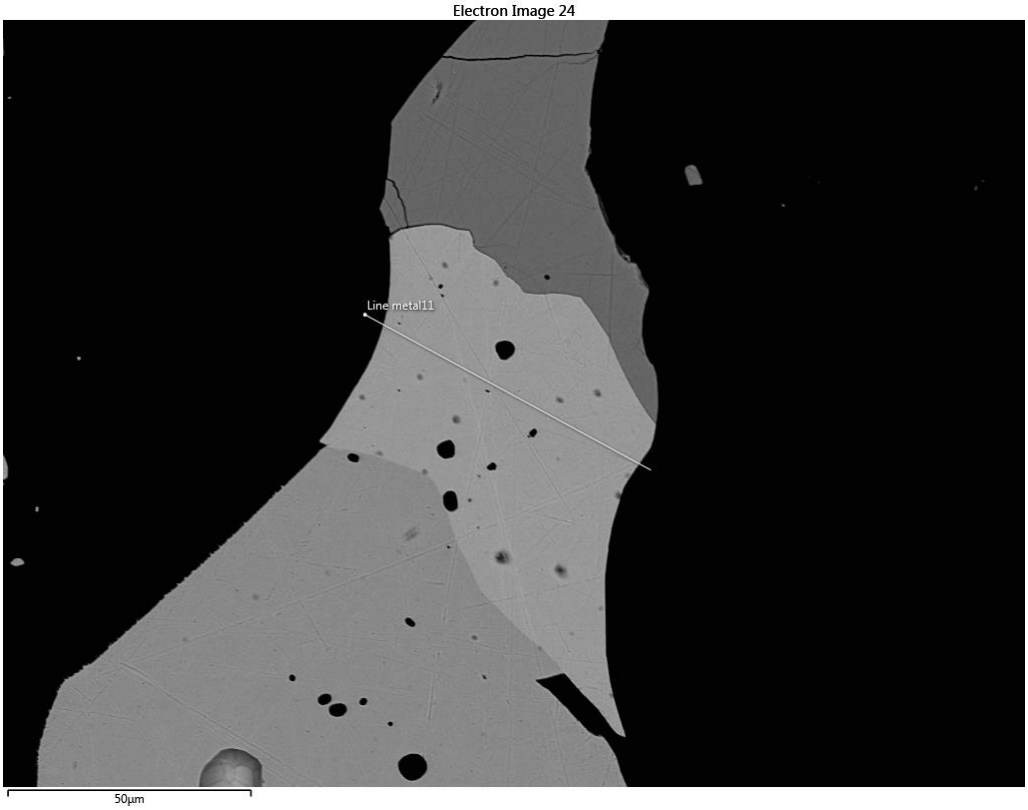

Figure 8. Example of brightness and contrast settings used to locate metal grains in BSE mode. The linescan is taken from a taenite grain (middle) between a kamacite grain (bottom) and a troilite grain (top).

CHAPTER 3: METHODS

GEOTHERMOMETRY

The closure temperature of a mineral is the temperature below which some measurable property of the mineral no longer changes in some systematic way as a function of temperature, such as equilibrium distribution of a chemical species in a multiple-phase system, and therefore ceases to record information about the temperature history of the mineral (Zhang 2008). It is the temperature below which the configuration of that particular property of the system is effectively frozen into place (Zhang 2008). The closure temperatures of interest here concern the rates of diffusive transport of cation species (Ca^{2+}, Mg^{2+}, Fe^{2+}) or elemental species (Fe, Ni) through the interiors of pyroxenes, olivines, chromite, taenite, tetrataenite, and kamacite and how they are influenced both by temperature and cooling rate.

The closure temperature of a mineral grain will be related to its cooling rate (Zhang 2008). Diffusion kinetic factors necessarily introduce a lag between the true temperature and the temperature recorded by chemical concentrations (Zhang 2008). A slower cooling rate will maintain higher temperatures for longer, which will allow more diffusional exchange, since diffusion is faster at higher temperatures (Zhang 2008). Rapid decreases in temperature will not allow a similar degree of adjustment of chemical equilibria within the necessary timeframe, and hence the closure temperature will be higher because it did not have sufficient time to equilibrate (Zhang 2008). Slower cooling rates therefore lead to lower closure temperatures (Zhang 2008). As diffusion

rates differ between minerals, investigating different minerals will allow cooling rates to be determined at different temperatures.

As each of the three geothermometers (pyroxene, olivine-chromite, and metallographic) used in this analysis are sensitive to different ranges of temperature, they will provide information on cooling history over a range in temperatures. If the H- and L-chondrite parent bodies did not experience collisional disruption while still hot, one would expect high petrographic-type material to have experienced either similar cooling rates to those modeled in e.g. Monnereau et al. (2013) or Harrison and Grimm, (2010); or systematic changes in cooling rate with respect to temperature, such as a slower cooling at lower temperature in the case of non-linear asymptotic cooling, for a body cooling to some low background temperature. Since all of the samples in this study are of petrographic type 6, if they had remained inside the metamorphosed core of an onion-shell body for the entire time that radiogenic heat was retained, they should all have cooled slowly throughout their histories.

If, however, collisional disruption and re-accretion did occur, faster cooling rates than that predicted by modeled onion-shell thermal evolution would be recorded below the temperature which the original onion-shell body had reached in its deep interior at that time. Material which was buried at depth within the asteroid during peak metamorphism and subsequently excavated by an impact and left to cool on or near the surface of the newly-formed rubble pile would cool quickly for the remainder of its thermal history. Alternatively, material which was subject to impact disruption and then

was transported to the warm interior of a rubble pile would cool first quickly, then slowly.

Since all grains in an un-brecciated sample will all have undergone the same thermal history, the highest closure temperature recorded necessarily constitutes a lower bound on the peak metamorphic temperature experienced by the system (Kessel et al., 2007). A negative correlation may also be observable between closure temperature and grain size, since larger grains would be more resistant to re-equilibration (Kessel et al., 2007). This, however, requires a cooling rate which is both sufficiently slow to allow compositional re-adjustment to be underway before closure and sufficiently fast that grains do not re-adjust completely.

PYROXENES, OLIVINE, AND CHROMITE

CLOSURE TEMPERATURE DETERMINATIONS

Pyroxene thermometry

Clinopyroxene and orthopyroxene closure temperatures were calculated using the formulation of Nakamuta et al. (2017), which itself is an extension of the classic Lindsley & Anderson, (1983) thermometer, which accounts for the kosmochlor ($NaCrSi_2O_6$) component commonly found in extraterrestrial pyroxenes. It is based on high petrographic type LL chondrites with clinopyroxene Na and Cr contents (0.019 – 0.024 Cr^{3+} cations per 6 oxygens and 0.035 – 0.041 Na^{+} cations per 6 oxygens) comparable to the samples analyzed here (see Appendix A for clinopyroxene data). Na and Cr in clinopyroxene are present in the approximate ranges of 0.3-0.4 wt% (0.03-0.04

cations per 6 oxygens) and 0.4-0.7 wt% (0.015-0.03 cations per 6 oxygens), respectively. These are above the detectability limits using the criteria given in Chapter 2 above.

Kosmochor is not addressed as a component in orthopyroxenes, but Na and Cr are used in the charge-balance consideration regarding the amount of ferric iron (Nakamuta et al., 2017). Na is mostly absent from orthopyroxene; Cr is typically in the 0.05 – 0.1 wt% (or 0.001 – 0.007 cations per 6 oxygens) range. They are however included in Appendix B for completeness because the formulation calls for them.

This new thermometer has been experimentally verified to have an error of ≤20 ^{o}C (Nakamuta et al., 2017) and produces consistently lower closure temperatures, by 50 ^{o}C or more, than the original Lindsley & Anderson (1983) thermometer (Nakamuta et al., 2017).

Olivine-chromite thermometry

Closure temperatures for the olivine-spinel system were calculated using an online tool (http://melts.ofm-research.org/CORBA_CTserver/Olv_Spn_Opx/index.php) based of the work of Sack & Ghiorso, (1991b), as well as the formulation developed by Wlotzka (2005). The temperatures calculated by the two formulations are in very good agreement, as seen in fig. 9. Both are based on the exchange of Fe and Mg divalent cations between the two phases and depend on the Cr content of the spinel. The Wlotzka (2005) formulation is simpler and less time-consuming to use, so that is what was chosen to be used for this study. This thermometer contains terms for Fe^{3+}, however

Fe^{3+} content of spinel can be assumed to be zero in the reducing conditions present in ordinary chondrites.

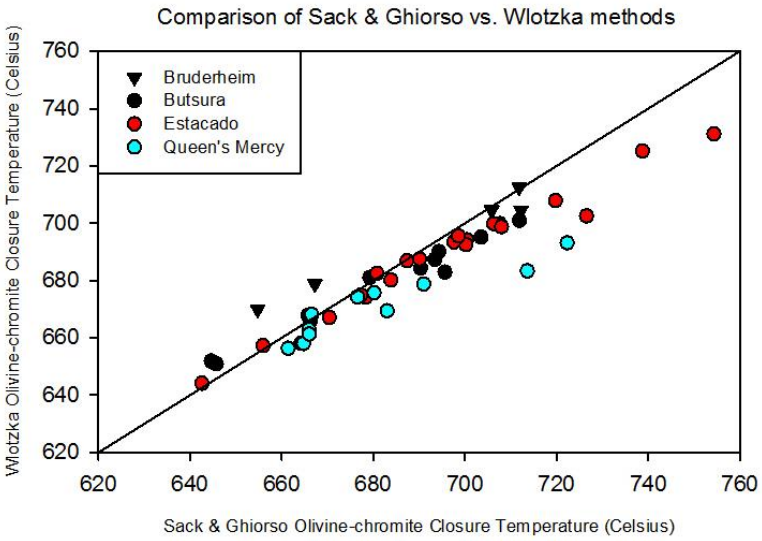

Figure 9. A comparison of the results of calculation of the closure temperature of the olivine-chromite system using both the formulation of Sack & Ghiorso (1991b) and the formulation of Wlotzka (2005) with a selection of 4 of the 10 total samples. An x = y line is included for reference.

Wlotzka (2005) relates chromian spinel and olivine compositions to closure temperature with the following equation:

$$T_c = \frac{5099 * Y_{Cr} + 917}{\ln(K_D) + 0.282 + 2.402 * Y_{Cr}} - 273$$

where T_c is the closure temperature in Celsius, $Y_{Cr} = \frac{Cr}{Cr+Al}$, and the distribution coefficient, K_D, is defined as:

$$K_D = \frac{\left(\frac{Mg}{Fe}\right)_{olivine}}{\left(\frac{Mg}{Fe}\right)_{spinel}}$$

(Wlotzka 2005) which increases as temperature decreases. Concentration units for both olivine and chromite are in stoichiometry as normalized to 4 oxygens.

DIFFUSION PARAMETERS

Diffusion in orthopyroxene

The inter-diffusion rates of Fe^{2+} and Mg^{2+} cations in orthopyroxene as determined by Ganguly & Tazzoli, (1994) was used for this study. See Table 2 below for values of pre-exponential factors and Table 2 for activation energies used. The value of D_0 in units of cm^2/sec for inter-diffusion of Fe and Mg in orthopyroxene is computed from the equation:

$$log_{10}\left(D_{Fe-Mg}^{opx}\right) = -5.54 + 2.6X_{Fe} - \frac{12530}{T}$$

where $X_{Fe} = \frac{Fe}{Fe+Mg}$ (in atomic %) and T is the temperature in Kelvins.

Diffusion in clinopyroxene

The rates of self-diffusion of Ca^{2+} and Mg^{2+} in diopside were experimentally determined by Zhang et al. (2010). The inter-diffusion relationship between two cation species is described by the equation:

$$D(Ca-Mg) = \frac{D(Ca) * D(Mg)}{X_{Ca}D(Ca) + X_{Mg}D(Mg)}$$

Where X_{Ca} and X_{Mg} are the mole fractions of Ca and Mg, respectively, and D(Ca) and D(Mg) are the self-diffusion coefficients for Ca and Mg, respectively. This expression assumes no deviation from thermodynamic ideality and hence is a simplification (Zhang et al., 2010) Diffusion rates are anisotropic in diopside, however, lacking crystallographic

orientation data, the average values of diffusion coefficients for each of Ca and Mg were used the calculation of inter-diffusion rates. The Fe component of the ternary clinopyroxene solid solution was ignored in these calculations, and compositions were treated as lying on the enstatite-diopside join of the pyroxene quadrilateral.

Diffusion in olivine

Chakraborty (1997) determined experimentally the rates of Fe-Mg inter-diffusion in olivine with composition Fo_{86}, which is close to olivine compositions of Fo_{75-79} for L-chondrites and Fo_{80-84} for H-chondrites.

Diffusion in chromite

Coefficients of self-diffusion of Fe and Mg in aluminous spinels were determined in Liermann & Ganguly, (2002). The inter-diffusion coefficients for Mg-Fe in spinel are determined in a manner analogous to that used above for diopside, by assuming the ideal case and using self-diffusion rates to calculate inter-diffusion rates.

Uncertainties in diffusion rates

Experimental uncertainties of diffusion rates in these mineral species are not negligible, and when propagated through the relevant equations, become the dominant source of uncertainty in the cooling rates thus derived. The diffusion coefficients of Mg^{2+} and Fe^{2+} in chromite are an especially large source of uncertainty, as they were determined not for chromian spinels but for aluminous spinels in Liermann and Ganguly, (2002). The true diffusion rates of Mg^{2+} and Fe^{2+} in chromite may be an order of

magnitude higher (Liermann & Ganguly, 2002) or even several hundred times higher (Ozawa 1984).

Table 2. Pre-exponential factors (D_0) of diffusion coefficients used in this study. Units are m^2/sec. [1] = Zhang et al. (2010), [2] = Chakraborty (1997), [3] = Ganguly & Tazzoli, (1994), [4] = Liermann & Ganguly, (2002). †: Orthopyroxene diffusion is compositionally dependent, value shown here is for a representative X_{Fe} of 0.2. ‡: Spinel diffusion is also compositionally dependent, value shown here is for a representative X_{Fe} of 0.86.

Units: m^2/sec	Clinopyroxene			Orthopyroxene	Olivine	Chromite
	a-axis	b-axis	c-axis			
Ca	19.9±32.2 $*10^{-9}$ [1]	3.02±8.97 $*10^{-7}$ [1]	2.4±5* 10^{-10} [1]	n/a	n/a	n/a
Mg	7±8$*10^{-15}$ [1]	1.23±2.63 $*10^{-11}$ [1]	1.44±2.26 $*10^{-13}$ [1]	n/a	n/a	1.9±1.4 $*10^{-9}$[4]
Fe	n/a	n/a	n/a	n/a	n/a	1.8±2.8 $*10^{-9}$ [4]
Fe-Mg interdiffusion	n/a	n/a	n/a	9.55±0.11 $*10^{-10}$ [3] †	5.38±0.89 $*10^{-9}$ [2]	1.89±3.41 $*10^{-9}$ [4] ‡

Table 3. Energies of activation (E), in units of calories per mole, for diffusion used in this study. [1] = Zhang et al. (2010), [2] = Chakraborty (1997), [3] = Ganguly & Tazzoli, (1994), [4] = Liermann & Ganguly, (2002).

Units: cal/mol	Clinopyroxene			Orthopyroxene	Olivine	Chromite
	a-axis	b-axis	c-axis			
Ca	76195 ±4226 [1]	83533 ±7663 [1]	63327 ±5495 [1]	n/a	n/a	n/a
Mg	35731 ±5316 [1]	55136 ±5478 [1]	42101 ±42065 [1]	n/a	n/a	48303 ±1888 [4]
Fe	n/a	n/a	n/a	n/a	n/a	47204 ±4493 [4]
Fe-Mg interdiffusion	n/a	n/a	n/a	57338 ±2000 [3]	54015 ±4302 [2]	n/a

COOLING RATE DETERMINATION

Pyroxenes, olivine, and chromite

Dodson (1973) is a seminal work used for determination of the cooling rate of a mineral system depending on diffusion parameters, closure temperatures, grain geometry, and activation energies. Dodson derived the following mathematical relationship between closure temperature, diffusion parameters, and the cooling rate at that temperature:

$$\frac{E}{RT_c} = \ln\left(-\frac{ART_c^2 D_0}{a^2 E(\frac{dT}{dt})_{@T_c}}\right)$$

where $A=e^G$ is a geometrical factor which has a different exponent G depending on grain geometry (spherical, cylindrical, or planar) as well as normalized position *x* within the grain (*x*=0.25, 0.50, or 1.00), R is the gas constant, T_c is the closure temperature of the system in Kelvins, D_0 is the diffusion coefficient at "infinite temperature" (i.e. the pre-exponential factor of the Arrhenius equation), *a* is the grain radius, and E is the energy of activation for diffusion. Since most silicate/oxide grains do not clearly fit into any of the three shape categories, they were simply approximated as spherical, and thus the value of A corresponding to spheres was used for all grains in all samples. The values used for G for spherical grains are taken from Dodson (1986) and are 2.0169, 2.1685, and 4.0082, respectively corresponding to *x* = 0.25 (grain rims), 0.50 (intermediate between grain rims and grain cores), and 1.00 (grain cores).

An underlying assumption of the Dodson formula is that even the cores of grains have undergone sufficient amounts of retrograde metamorphism to substantially affect their composition. In very quickly-cooling or slowly diffusing systems, however, this may not be the case, as grains may only be partially reset in such circumstances. Ganguly & Tirone, (1999) extended Dodson's original formulation to include arbitrarily small amounts of diffusion. The difference lies in determining the value of the factor A, using instead the factor $A' = e^{G+g}$, where g is determined from the value of another parameter, M:

$$M = \frac{RD(T_0)T_C^2}{E\left(\frac{dT}{dt}\right)_{@T_c} a^2}$$

where R is the gas constant, $D(T_0)$ is the diffusion rate at the peak temperature T_0 from which cooling begins, T_c is the closure temperature, E is the activation energy, and a is the diffusion distance. g varies as a function of M, becoming higher as M decreases, and going to zero for M>1. This is important in the case of slow-diffusing systems, large grain sizes, or very fast cooling, all scenarios which result in M being less than 1. This must take into account the normalized position within the crystal as well, since a non-uniform zoning profile will develop in a grain which has not had a chance to undergo diffusion for long enough to completely re-equilibrate.

This introduces a complication in the calculation procedure, in that in order to obtain a cooling rate from the Dodson (1973) equation, a cooling rate must already be known. Therefore, an iterative method was used. First a trial value of dT/dt was used to

calculate a value of M (with the other terms being held constant), which was then used to look up the corresponding value of g in Table 1 of Ganguly and Tirone, (2001). Modifying the value of A accordingly, the difference between the right-hand side (RHS) and left-hand side (LHS) of the Dodson equation was calculated. A value of dT/dt which produced a value of RHS – LHS which had at least two zeros past the decimal was deemed to be sufficiently close to the true value. Mean closure temperature and distances to grain edges for each grain position of rim, intermediate, and core were used in the final calculations. Peak temperature T_0 was taken to be 930 ^oC according to Slater-Reynolds and McSween, (2005), as temperatures higher than this would cause melting at metal-troilite interfaces, for which there is generally no clear evidence. Effects of reducing T_0 were examined as well and are discussed below.

GRAIN SIZE CONSIDERATIONS

Grain size is also an important parameter, as it is a squared term in the Dodson equation and can greatly affect the value of dT/dt. This is not as straightforward as simply measuring the radius of a cross-section of a spherical grain, as virtually all grains have irregular shapes. The method used here to find a representative size for each grain is to use the mean value of the distances to the furthest and nearest edges of the grain from the location of the EDS spot. The ratio of the distance to the nearest edge to this mean was used to decide whether to designate the spot location as either in the rim ($x \leq 0.25$), intermediate ($0.25 < x < 0.5$), or core ($0.5 \leq x \leq 1$) position. Distances were measured using Adobe Photoshop's measure tool by using the image's scale bar to

convert pixels to microns. Chromite, orthopyroxene, and clinopyroxene grain sizes were measured from BSE images which were acquired while spot data was gathered. Olivine grains, however, were not always amenable to this method, as olivine is often the matrix mineral in ordinary chondrites and grain boundaries are very difficult to distinguish from fractures in BSE images. It was therefore necessary to locate the grains optically and measure them from cross-polarized light micrographs.

METALLOGRAPHIC THERMOMETRY

Metallographic thermometry does not make use of the Dodson-Ganguly formulation and instead relies on the work of Wood (1967) and Willis and Goldstein, (1981a) to determine cooling rates, and the P-free Fe-Ni sub-solidus phase diagram of Reisener and Goldstein, (2003a) to determine closure temperatures. The Ni content of the taenite or tetrataenite rim changes depending on the closure temperature, becoming more Ni-rich as the grain cools.

Reisener & Goldstein describe the phase transitions undergone by cooling P-free Fe-Ni alloys in their two 2003 (2003a, 2003b) papers. Nucleation of kamacite occurs at taenite-taenite grain boundaries, which consumes one taenite grain and forces the excess Ni into the other, resulting first in a taenite grain with a tetrataenite rim, and then ultimately a tetrataenite grain partially surrounded by kamacite, as observed in, for example, Queen's Mercy. A single taenite grain which is not in contact with any other taenite grains will not undergo this transformation – it turns to a martensite by diffusionless transformation instead. The original cooling rate curves from Wood (1967)

were revised by Willis & Goldstein, (1981a), and these revised curves were what were employed in this work. The more slowly a metal grain of a given size cools, then the longer it remains at a temperature which is high enough to allow significant inward diffusion of Ni to take place. Hence the Ni content of more slowly-cooled grains will be higher. Cooling rates determined for metal grains are through the temperature interval recorded by the cores and rims of the grains, as opposed to the cooling rate through a single closure temperature as is the case for the Dodson (1973) formula. Loss of Ni into the surrounding silicates is negligible (Petry et al., 2004), so this can be considered a closed system.

Scatter in the data is expected, since the grains are nonspherical and the plane of the thin section does not necessarily cut through the thickest part of each metal grain. Since the Ni content is the lowest in the center of a grain, this will result in an artificially high Ni content for a grain whose apparent size is smaller than its true size. The higher cooling rates are therefore more likely to be accurate (Taylor et al., 1987). Above a certain cooling rate, the Ni content will level off above a particular grain size, as there would not have been sufficient time for Ni to penetrate further into the grain interior (Taylor et al., 1987). This can also happen as a result of shock-induced heating, because of its short duration compared to cooling from peak heating. The uncertainty in metallographic cooling rates as estimated by Wood (1967) is a factor of 2.5. See Appendix F for the full array of metallographic cooling rate plots obtained in this study.

ERROR PROPAGATION

When errors were not given in source papers such as Nakamuta et al. (2017) for pyroxene closure temperatures, they were calculated via the standard methods of error propagation in arithmetic calculations. Standard deviations of compositions were used when making calculations from chemical data. The error propagation equations used were the following, with σ_i being the standard deviation of each quantity *i*:

For addition/subtraction, if

$$x = a + b - c$$

Then

$$\sigma_x = \sqrt{{\sigma_a}^2 + {\sigma_b}^2 + {\sigma_c}^2}$$

For multiplication/division, if

$$x = \frac{a * b}{c}$$

Then

$$\sigma_x = x * \sqrt{\left(\frac{\sigma_a}{a}\right)^2 + \left(\frac{\sigma_b}{b}\right)^2 + \left(\frac{\sigma_c}{c}\right)^2}$$

For exponentiation, if

$$x = a^b$$

Where b is constant, then

$$\sigma_x = b * x * \frac{\sigma_a}{a}$$

For the natural logarithm, if

$$x = \ln(a)$$

Then

$$\sigma_x = \frac{\sigma_a}{a}$$

With an additional factor of 0.434 present if the logarithm is base 10 instead.

For the natural antilogarithm, if

$$x = e^a$$

Then

$$\sigma_x = x * \sigma_a$$

With an additional factor of 2.303 present if it is instead the base-10 antilogarithm.

CHAPTER 4: RESULTS

PYROXENE SYSTEM

Compositional zoning

There is little overall rim-core zoning in either ortho- or clinopyroxenes, as evidenced by similar compositions as a function of the distances from the grain rims of EDS spot data (see Appendix H). This can be taken to mean either that cooling was so rapid that not even the grain edges had a chance to exchange cations with their environment, or that cooling was so slow that equilibrium was re-achieved at lower temperatures and all intermediary zoning profiles were flattened.

H-chondrites show a decrease in enstatite content with proximity to grain rims in clinopyroxenes and a corresponding increase in enstatite content in orthopyroxenes. L-chondrites have more flattened enstatite profiles in pyroxenes in comparison and show very little trend. H-chondrites show a weak decrease in wollastonite content with proximity to grain rims in orthopyroxenes, with a corresponding increase for clinopyroxenes. L-chondrites are only weakly zoned at best, and suggest the opposite trend, with a decrease in wollastonite in clinopyroxenes and an increase in wollastonite in orthopyroxenes. However, this may simply be an artifact of grain sizes clustering in that range, with an outlier which happens to have a slightly lower wollastonite content.

Pyroxene closure temperatures

Closure temperatures for orthopyroxenes fall mostly within the 700 – 900 ^{o}C range, as seen in fig. 10. Portales Valley is an exception in that, while most of its closure temperatures for both clino- and orthopyroxenes overlap with those of the other H-chondrites, it shows higher temperatures than the others as well, a sign of its higher peak metamorphic temperatures (Ruzicka et al., 2005). The compositional data for pyroxenes in H-chondrites is consistent with retrograde metamorphism: in orthopyroxene, both an increase in enstatite and a decrease in wollastonite towards grain rims in orthopyroxene indicate a lower closure temperature (Nakamuta et al., 2017, Lindsley 1983); likewise, a decrease in enstatite and an increase in wollastonite in clinopyroxenes also indicate a lower closure temperature. L-chondrites show no particular trend on closure temperatures with distance to grain rims, in keeping with its more flattened compositional profiles.

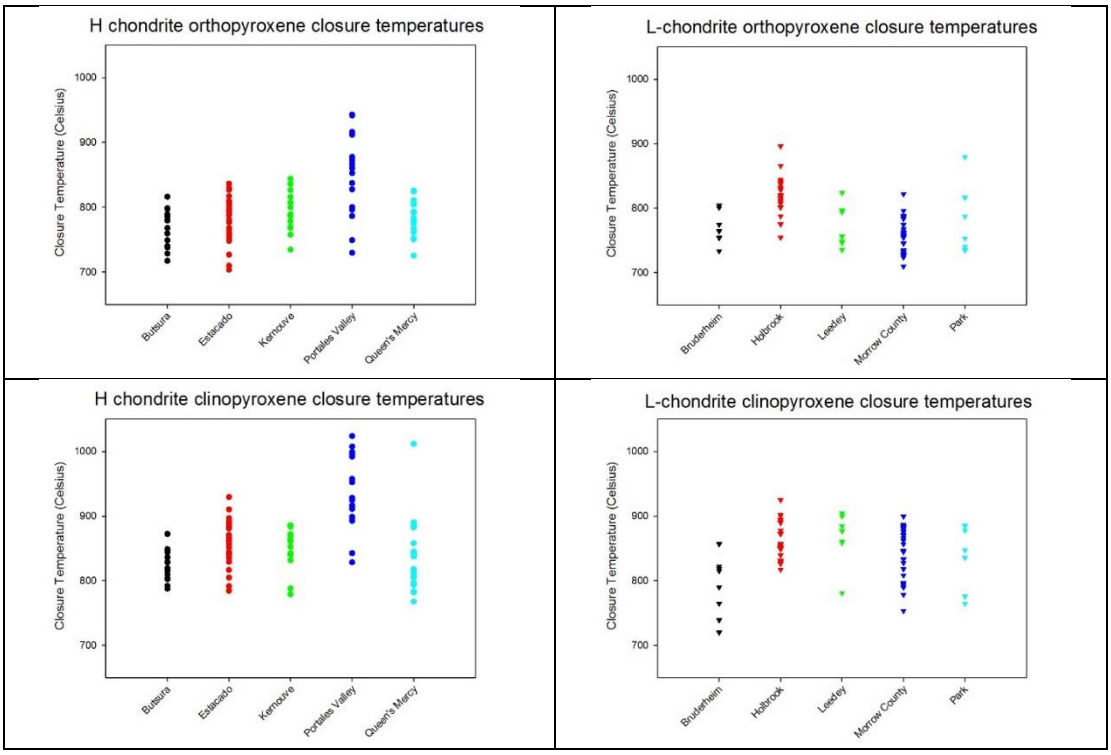

Figure 10. Individual closure temperatures calculated for the pyroxene system for all samples.

OLIVINE-CHROMITE SYSTEM

Compositional zoning

Although data scatter, the olivines in the H-chondrites show a downward trend in fayalite content with proximity to grain rim, whereas the chromites have an upward trend in the same compositional parameter $X_{Fe} = \frac{Fe}{Fe+Mg}$ (figs 11 & 12). The zoning profiles in both the olivines and the chromites reflect their response to cooling from equilibrium – the lower Fa% in olivine grain rims compared to the cores produces a higher value of K_D, resulting in a lower closure temperature (see Chapter 3); the higher X-Fe in chromite rims as opposed to chromite cores likewise results in a higher K_D. For the H-chondrites, there is a decrease in the value of $Y_{Cr} = \frac{Cr}{Cr+Al}$ with proximity to grain

rim as well (fig. 11). A decrease in Y-Cr also corresponds to a decrease in closure temperature according to the Wlotzka (2005) formulation (see isotherms in figs 14 & 15). K_D varies inversely with Y-Cr on the isotherm plots, which suggests that they both are affected by variations in closure temperature (figs 14 & 15). Zoning plots also show that these variations have a relationship to distances to grain rims as well. The lower closure temperatures of the grain rims compared to those of the grain cores is consistent with a cooling process, in which grain rims more readily exchange chemical species with the surrounding environment. The olivine-chromite system in the H-chondrites therefore appears to have been subject to retrograde metamorphism.

The L-chondrites do not show a similar degree of core-rim compositional variation. Perhaps notable are the differences between samples, namely, that olivines in Holbrook are more ferroan and that chromites in Park are less ferroan. Olivines and chromites in L chondrites in general are slightly more ferroan, as with pyroxenes. Some zoning has been documented in olivines in type 5-6 chondrites (Kessel et al., 2007). Forsterite content in olivine increases by about 2% in close proximity to the adjacent chromite, but chromites do not show similar zoning, perhaps implying that Mg-Fe inter-diffusion is faster in chromite than in olivine (Kessel et al., 2007).

Olivine-chromite closure temperatures

The results for the olivine-chromite system are broadly similar to those obtained by the pyroxene system, within their respective ranges of applicable temperatures. There is more discernible zoning within the olivine and chromite grains, which can be

observed better by combining data from multiple samples. The trends are likewise stronger for H chondrites than for L. See Appendices C & D for the raw data. Closure temperatures determined using the Wlotzka (2005) formulation are shown in fig. 13. In the L-chondrites, Park has the highest closure temperature of ~780 C and has the highest range overall. In the L-chondrites, the ranges for olivine and chromite are from ~670 C to ~780 C. Estacado has the highest closure temperature among the H-chondrites at ~730 C. In the H-chondrites, the ranges for olivine and chromite are from ~640 C to ~740 C.

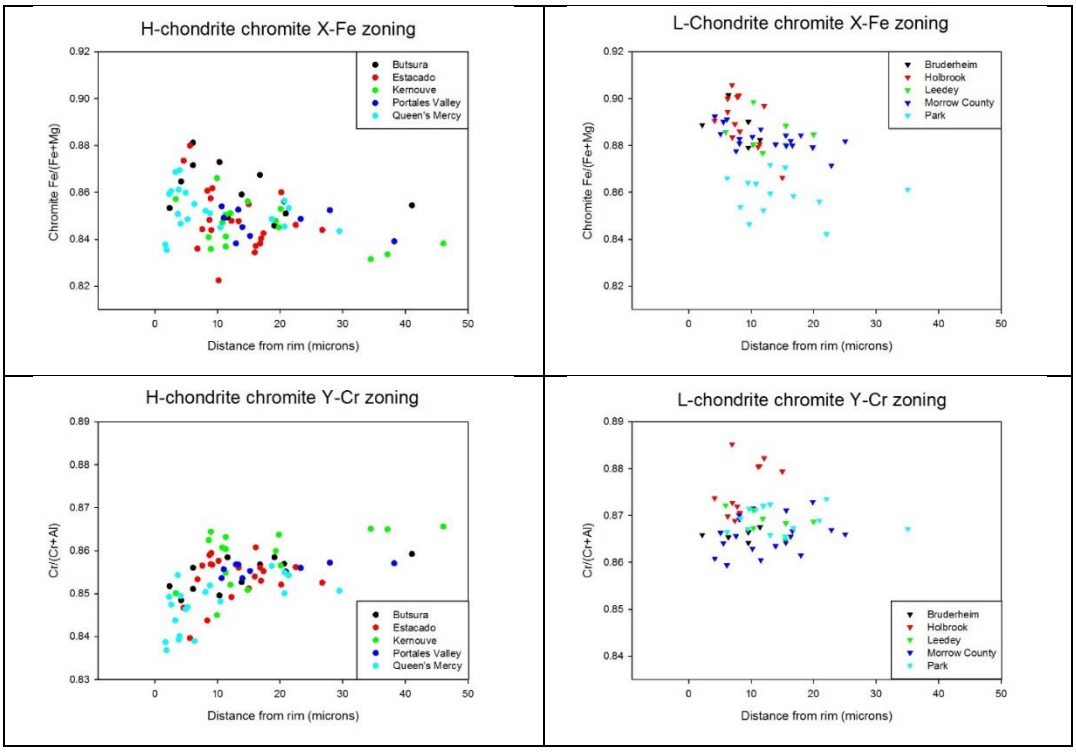

Figure 11. Compositional zoning profiles for Fe and Cr chromites. The upward trend in X_{Fe} and the downward trend in Y_{Cr} with proximity to the grain rim are both indicators of the start of lower-temperature equilibration.

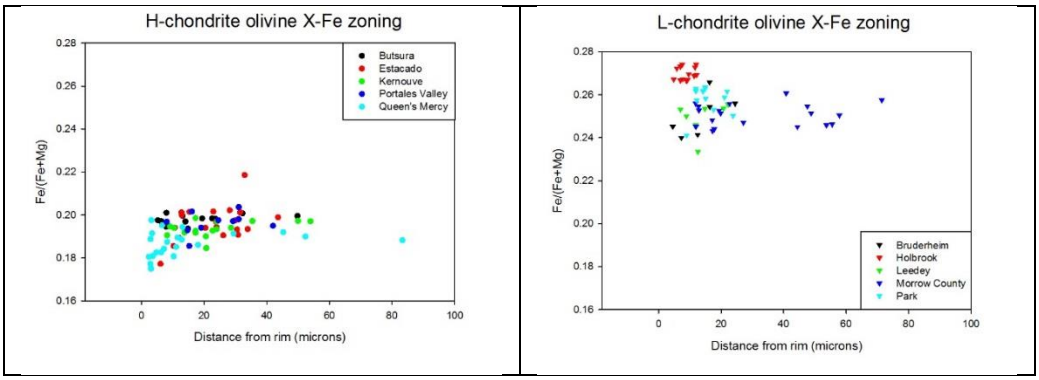

Figure 12. Compositional zoning profiles for Fayalite content in olivines.

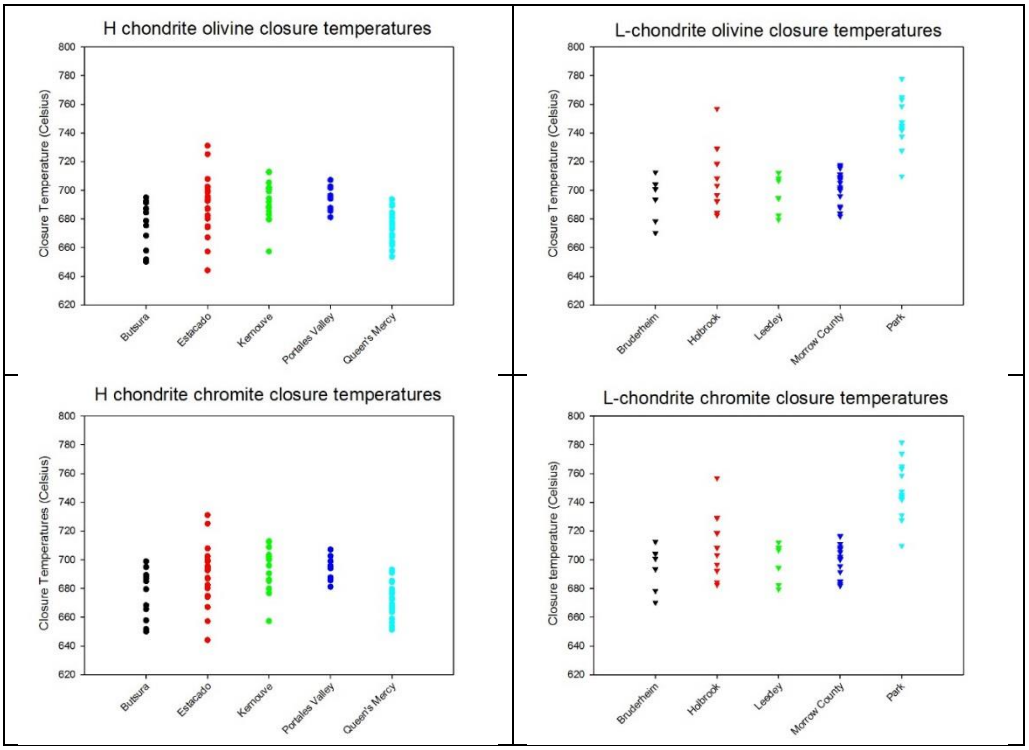

Figure 13. Individual closure temperatures calculated for the olivine-chromite system for all samples.

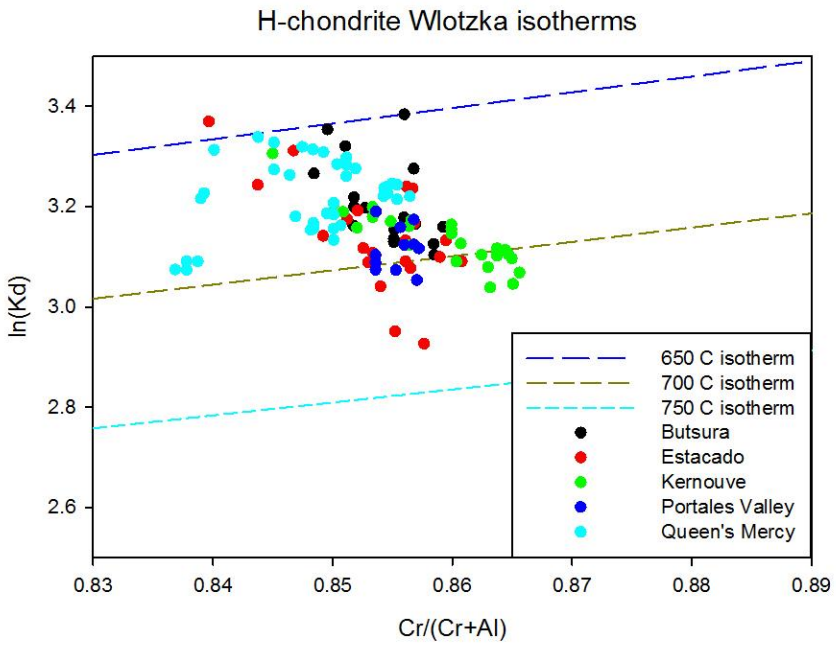

Figure 14 Wlotzka isotherm plot for the 5 H-chondrite samples. K_d in this case is equal to $(Mg/Fe)_{chromite}$ / $(Mg/Fe)_{olivine}$. The concentration units are stoichiometries normalized to 4 oxygens in the case of chromite and mole fractions calculated from normalized atom % data in the case of olivine.

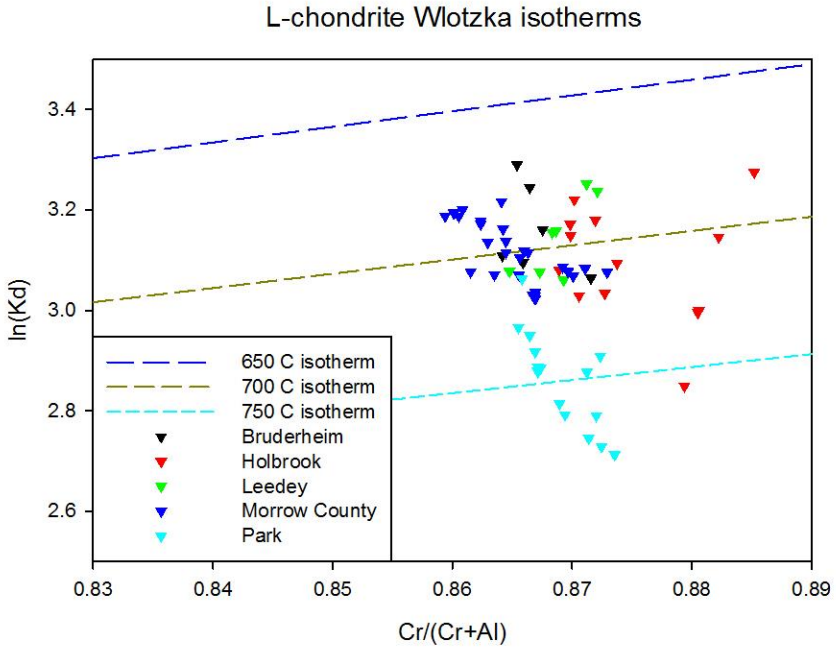

Figure 15 Wlotzka isotherm plot for the 5 L-chondrite samples. K_d in this case is equal to $(Mg/Fe)_{chromite}$ / $(Mg/Fe)_{olivine}$. The concentration units are stoichiometries normalized to 4 oxygens in the case of chromite and mole fractions calculated from normalized atom % data in the case of olivine.

COOLING RATES

Metallographic cooling rates

Metallographic cooling rates were obtained for each sample. A typical example of the M-shaped Ni profile is provided in fig. 16. Appendix F contains the full suite of metallographic cooling rate plots. The H-chondrites are all slowly-cooled through metallographic temperatures and generally do not exceed 10 C/Myr. The range in metallographic cooling rates is shown in fig. 17 by Queen's Mercy, the slowest, and Butsura, the fastest. They tend to plot more coherently than their L-chondrite counterparts, which is probably a consequence of the more strongly shocked nature of the L-chondrite samples (discussed below). The L-chondrites have a much wider range in metallographic cooling rates, with the fastest being Park, which cooled at ~1000 ^{o}C/Myr. Leedey, the most slowly-cooled, is well within the range of H-chondrites at ~3 ^{o}C/Myr (fig. 18). Bruderheim and Morrow County plot at approximately 10 ^{o}C/Myr, and Holbrook plots at approximately 90 ^{o}C/Myr. Park cooled much more quickly at low temperatures compared to the other samples, and is thought to have been deposited at the surface or very near the surface of the re-accreted L-chondrite rubble-pile (Ruzicka et al., 2015).

Horizontal error bars on metallographic cooling rate plots are determined from the distance from the Ni-rich peak in a linescan to the apparent edge of the grain in the linescan. The true edge of the grain lies between these two points, as the sloped profile (such as that seen in fig. 16 between ~8 and ~10 μm) is not the true Ni concentration

profile but an artifact of interaction volume at grain boundary effects in the SEM. The grain was assumed to terminate midway between the top and bottom of the sloped profile, and the width if the sloped profile was taken to be the uncertainty in the grain radius. Vertical error bars were calculated using the standard deviation of the values which lay in the lowest 15% of Ni concentrations for the whole grain profile.

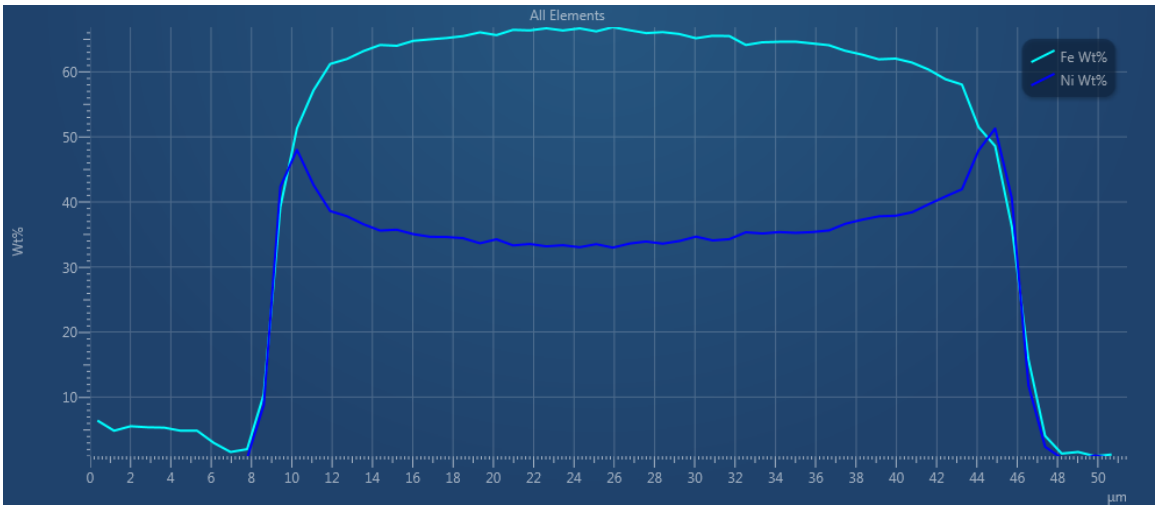

Figure 16. Queen's Mercy linescan 9, showing a slowly-cooled grain with the typical M-shaped profile consisting of tetrataenite rims surrounding a taenite grain with a zoned interior.

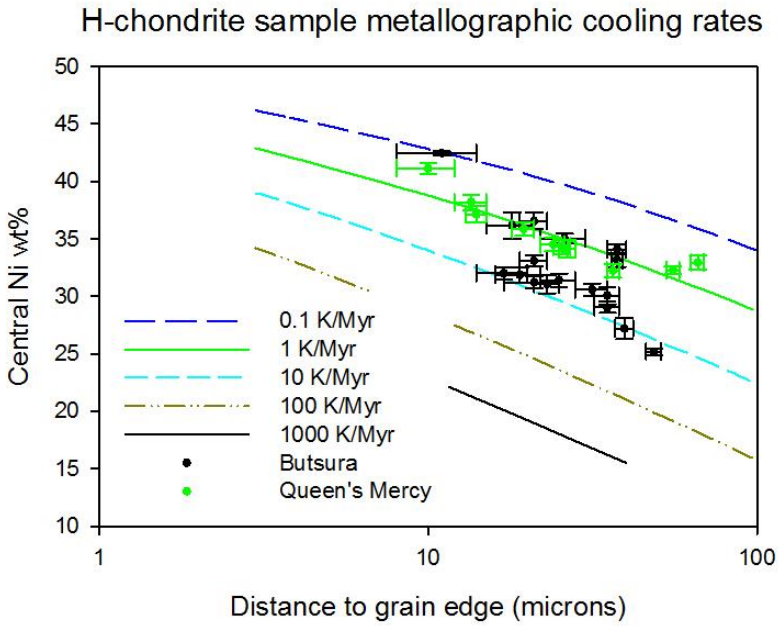

Figure 17. Wood plot showing the range of cooling rates recorded by the H-chondrites. Queen's Mercy is an especially "coherent" plot, in that the fastest cooling rates recorded plot approximately parallel to a ~1-2 K/Myr isoline. Butsura's cooling rates are approximately 10 K/Myr.

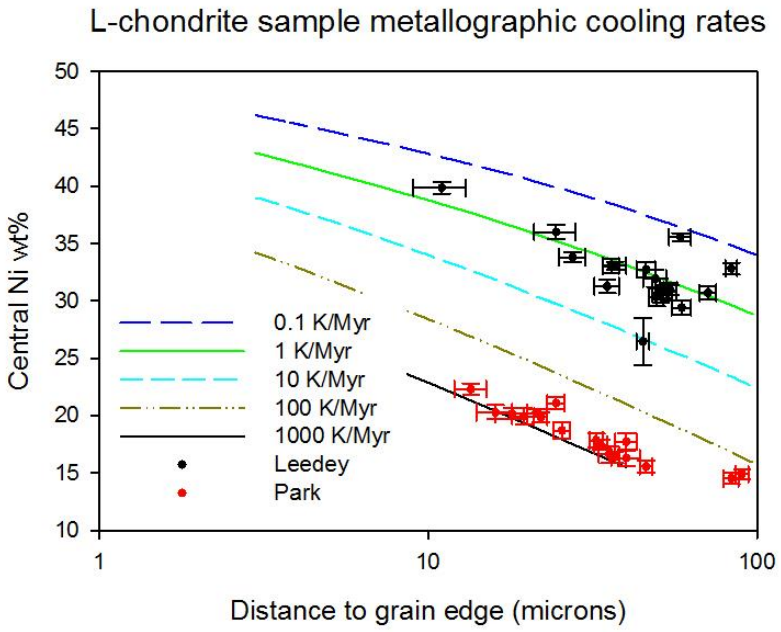

Figure 18. Wood plot showing the range of metallographic cooling rates recorded by the L-chondrites. Park shows, by far, the fastest cooling recorded by metals in this study. Leedey's cooling rates are approximately 4 K/Myr, Park's are ~1000 K/Myr.

Silicate/oxide cooling rates

The Dodson (1973) formula, as well as the Ganguly & Tirone, (1999) extension distinguishes between different normalized positions within the grain, in that an exponential factor in the numerator takes on a different value depending on whether the spot data were acquired from the rim, the core, or intermediate between rim and core (see Chapter 3 for more detail). As this may introduce mathematical artifacts into the calculated cooling rates (see below), the data in figs 19-25 are color-coded according to this scheme. Cooling rates determined from grain core, intermediate (or "int" for brevity in plot legends), and rim positions are colored green, red, and black, respectively. Represented below are cooling rates calculated from the average closure temperatures and mineral compositions for each grain position category. Each data point from the pyroxene and olivine-chromite systems represents a cooling rate as it cooled though that closure temperature. The distances to the grain's rims were used, rather than the characteristic grain sizes, because this probably constitutes a better measure of diffusion distances, as the extent of resetting of closure temperature was likely not sufficient to have substantially affected most grain cores in this case, as assumed by the original Dodson (1973) formulation. Since there are two closure temperatures associated with metallographic thermometry (see Chapter 3), the cooling rate is as measured through a temperature interval (taenite grain core vs. tetrataenite grain rim) rather than through a single temperature. Figs 19-25 show averages of each closure temperature for each metal grain, as well as averages of cooling rates for the same. The "onion-shell cooling"

curve is from a digitization of the temperature vs. cooling rate curve modeled for Estacado in Harrison & Grimm, (2010).

Cooling rate plots for the same samples (Butsura, Queen's Mercy, Leedey, and Park) as in figs 17 & 18 above, along with two others, are shown here. Appendix G contains cooling rate plots for the remainder of the samples, as well as plots showing cooling rates calculated using the original Dodson (1973) formula for each individual measurement. A reference onion-shell cooling curve, taken from Harrison and Grimm (2010), modeled for Estacado, is included in each cooling rate plot for comparison.

Cooling rates from two different starting temperatures were determined, 960 ^{o}C, a reasonable peak temperature of most type 6 chondrites, and a lower temperature which varies between samples, being in the range 827 ^{o}C – 902 ^{o}C. The latter peak temperatures were chosen for each sample to be within a few degrees of the average maximum closure temperature for that sample. Variation in T_0 to temperatures lower than 960 ^{o}C did not produce any significant change in calculated cooling rates for orthopyroxene, olivine, and chromite. Only clinopyroxenes were noticeably affected by this change, and even that effect does not change the conclusions which can be drawn from the data.

Summarizing the results in figs 19-25 and in Appendix G, clinopyroxenes have mostly higher closure temperatures than orthopyroxenes, though there is overlap present. Clinopyroxenes also display, in most instances, cooling rates slower than their orthopyroxene counterparts. Cooling rates determined for grain cores are for the most

part higher than those determined for grain rims for a given closure temperature. Orthopyroxene and olivine produce cooling rates which are generally in good agreement, on the order of 100 – 1000 ^{o}C/kyr, in that they plot within the same margin of error. The only exception is Park (fig. 25), and that is only for intermediate grain positions in orthopyroxene. Chromite produces cooling rates which are consistently one to two orders of magnitude faster than for olivine, despite occurring within the same temperature range. Overall, the results obtained for the H and L-chondrites are very similar, with the principal difference being that there is more variability in metallographic cooling rates for the L-chondrites.

Errors in pyroxene closure temperatures are given as ±20 ^{o}C according to Nakamuta et al. (2017). Error bars for the olivine-chromite thermometer are averages of errors in compositions (i.e. standard deviations of concentrations for each sample) propagated through the Wlotzka (2005) formula for individual measurements. Errors in cooling rates for silicate and oxide systems were based on those given in the literature for diffusion parameters (see Tables 2 & 3), and on those already calculated for composition and closure temperature. They were propagated through the original Dodson (1973) formula by solving it for dT/dt. In each case, the errors in cooling rate were proportional to the cooling rate itself by a factor which ranged from 2.4 – 4.7, depending on the mineral and sample. It is that factor which is used to compute the positions of the error bars in these plots.

COOLING RATES FOR SELECTED H-CHONDRITES

The H-chondrite Estacado is shown as well in figs 19 & 20, as an illustrative example of the good agreement between the cooling rates obtained for orthopyroxene and olivine, the systematically lower cooling rates obtained for clinopyroxene, the anomalously high cooling rates obtained for chromite. Cooling rates obtained for a lower peak temperature are displayed as well in fig. 20, and are not perceptibly different, with the exception of clinopyroxene grain cores.

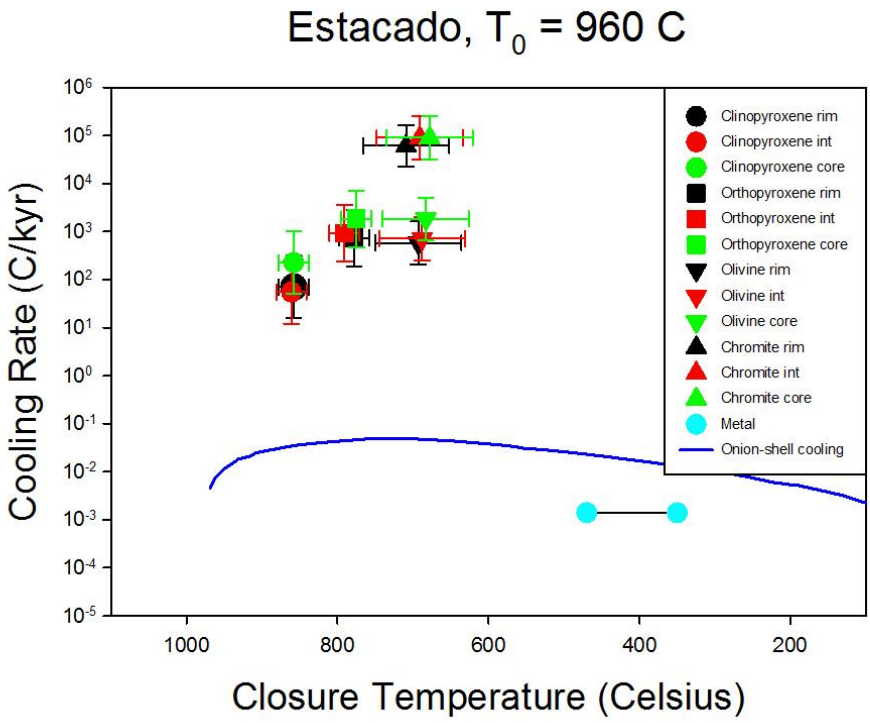

Figure 19. Cooling rate plot for Estacado with a starting temperature of 960 degrees C.

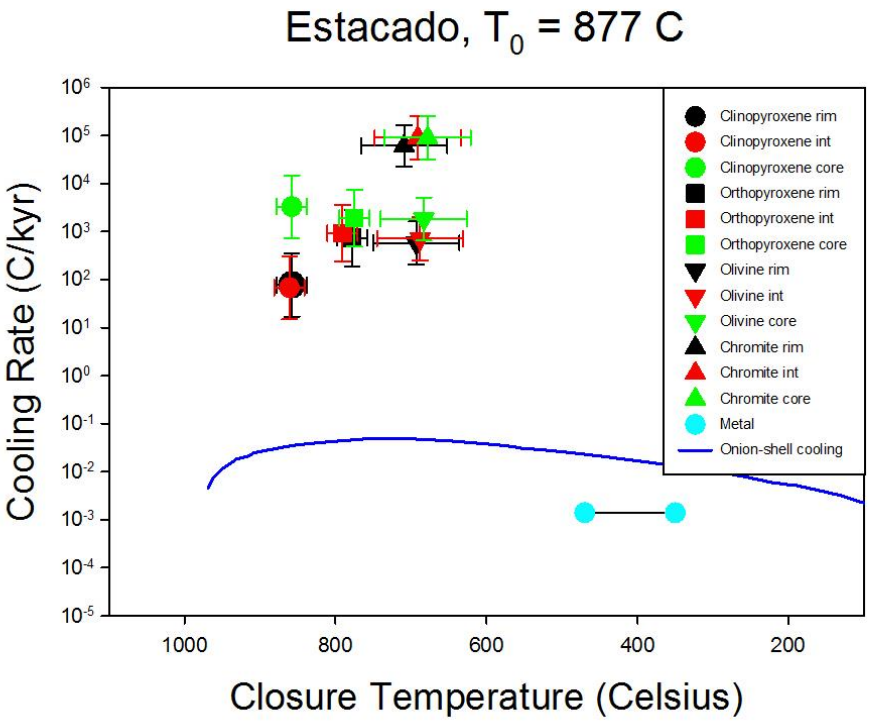

Figure 20. Cooling rate plot for Estacado with a starting temperature of 877 degrees C.

Butsura and Queen's Mercy are shown in figs 21 & 22. While slightly more scattered, the results are essentially the same as for Estacado. In Queen's Mercy there is some overlap in closure temperature between clinopyroxene and orthopyroxene.

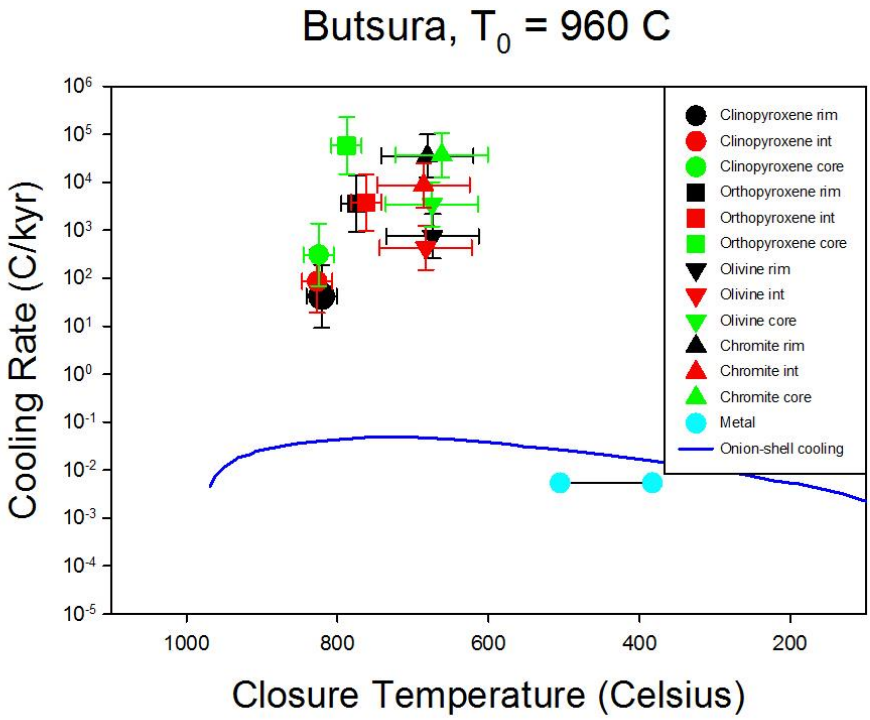

Figure 21. Cooling rate plot for Butsura with a starting temperature of 960 degrees C.

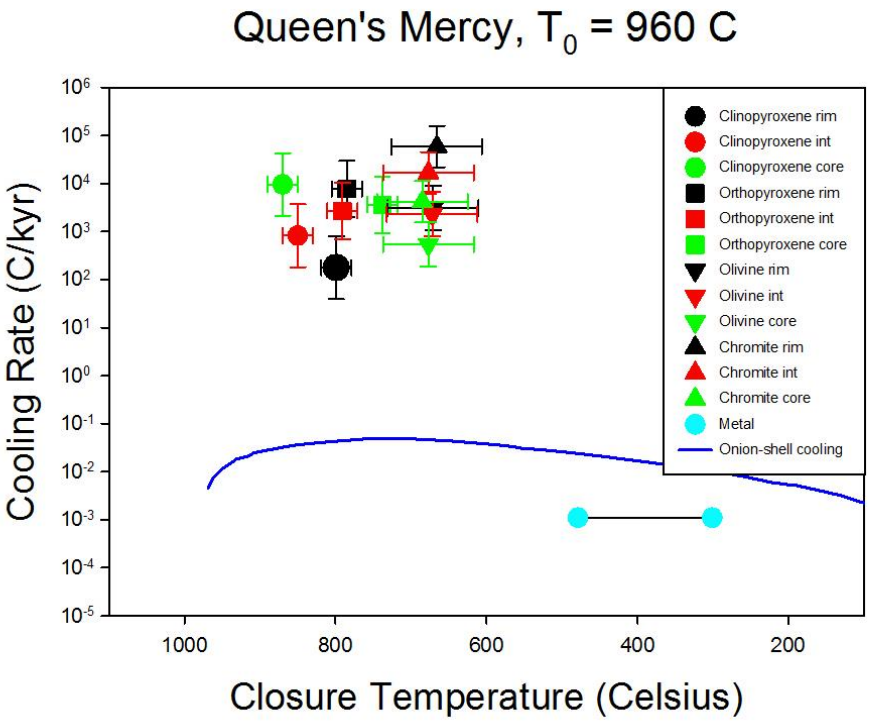

Figure 22. Cooling rate plot for Queen's Mercy with a starting temperature of 960 degrees C.

COOLING RATES FOR SELECTED L-CHONDRITES

Although the data is somewhat sparse for Leedey (spot data from every grain position were not always available) in fig. 23, there is good agreement between cooling rates obtained for olivine and orthopyroxene.

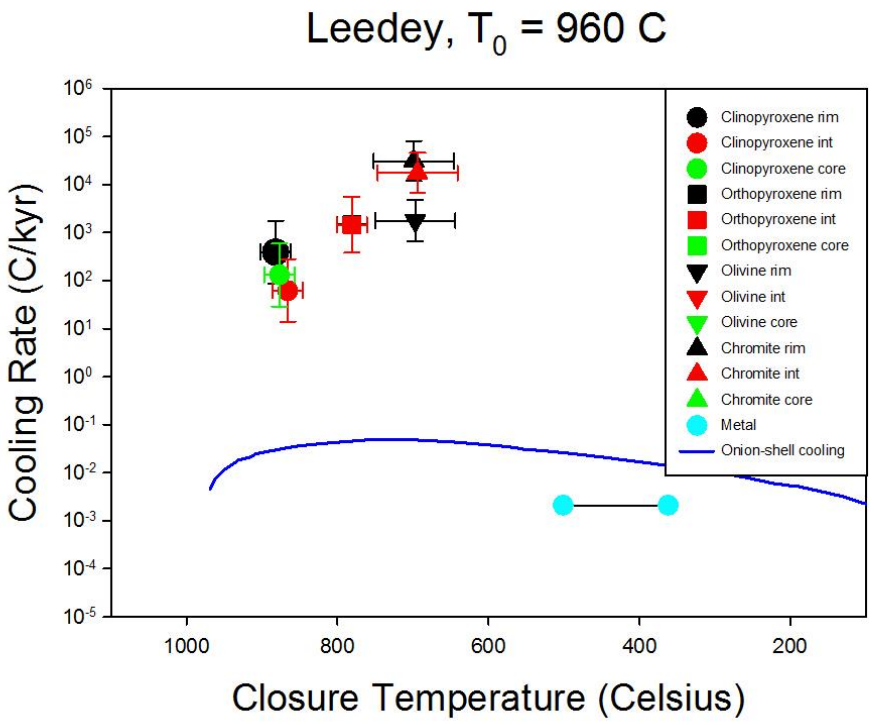

Figure 23. Cooling rate plot for Leedey with a starting temperature of 960 degrees C.

Also shown is the L-chondrite Morrow County (fig. 24), the most strongly shocked of the samples, to illustrate that shock effects do not appear to disrupt thermometry information in silicate or oxide systems. The only noticeable effect shock appears to have is the partial re-equilibration of metal grain rims, leading to a narrower apparent closure temperature range (see Chapter 5 below).

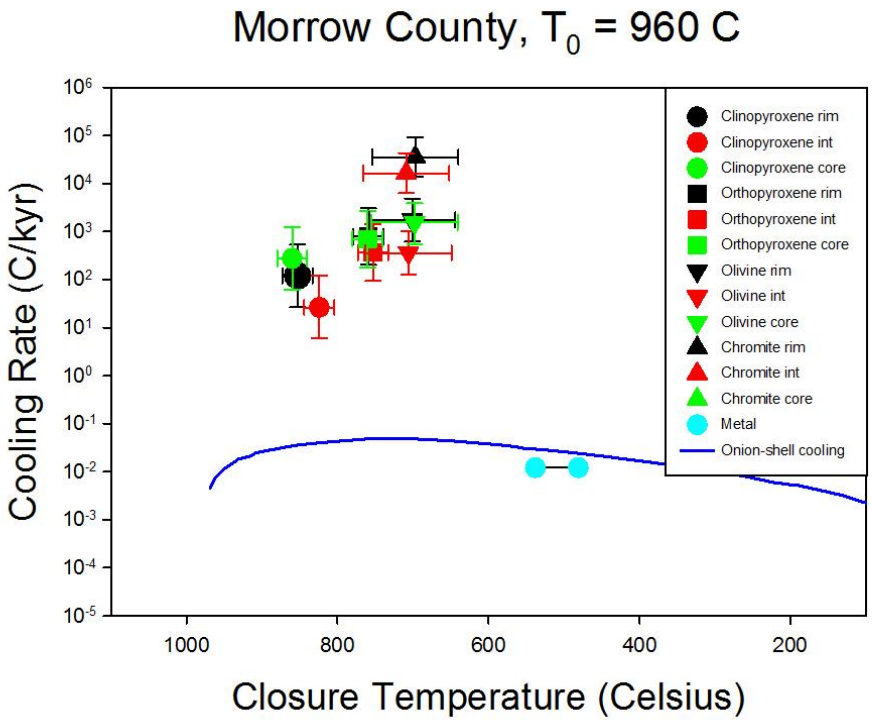

Figure 24. Cooling rate plot for Morrow County with a starting temperature of 960 degrees C.

Park's cooling rates, shown in fig. 25, is the sole exception to slow cooling at low temperatures. Park outpaced onion-shell style cooling throughout its history. There is also more scatter in its silicate-oxide cooling rates.

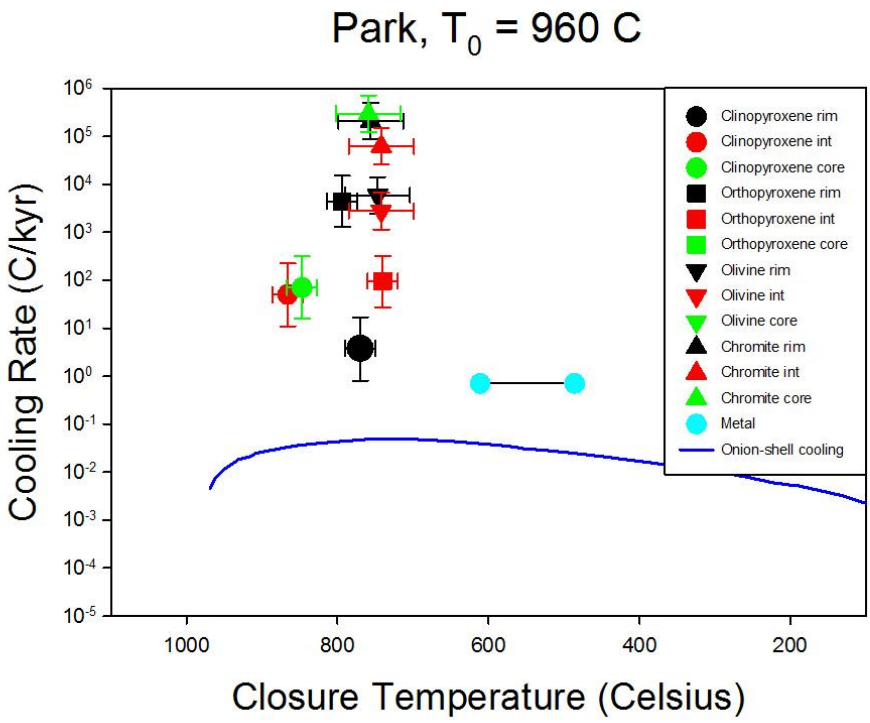

Figure 25. Cooling rate plot for Park with a starting temperature of 960 degrees C.

CHAPTER 5: DISCUSSION

Artifacts of the Dodson formula

It is noteworthy that in many of these cooling rate calculations, the grains from which spots were taken from the cores of the grains plot systemically higher, often by an order of magnitude or more. In the Dodson formula, the value of the exponent *G* changes depending on the normalized position within the grain, increasing towards the core. The term for grain radius is also in the denominator of the equation, resulting in faster cooling rates for smaller grains, all else being equal. Another factor to consider is that grains from which data was gathered from the cores were often the smallest, rather than the largest, as smaller grains have less area from which to select a location for an EDS point analysis in order to avoid grain-boundary interference effects. These factors combine to mean that data taken from grain cores, shown in green in Figures 19-25, is often skewed towards artificially high values and are thus of more questionable veracity than for rim or for intermediate grain positions.

Clinopyroxene/orthopyroxene discrepancy

The cooling rates recorded by clinopyroxenes are consistently lower than orthopyroxene and olivine by approximately an order of magnitude. A potential explanation for this is that clinopyroxene inter-diffusion rates may be faster than what is given by Zhang et al. (2010), as that study did not account for the effect of Fe, which would allow for more possibilities of ion swapping, both for Ca and Mg. Calculations of cooling rates based on clinopyroxenes may therefore be less meaningful than those

based on orthopyroxenes, which display a greater, though still weak, extent of zoning (see Appendix H).

Olivine/chromite discrepancy

Cooling rates calculated from chromite plot consistently higher, by as much as two orders of magnitude, than cooling rates within the same range of closure temperatures calculated for olivine. This is despite a similar range in grain sizes and diffusion distances for both mineral species. The uncertainty associated with diffusion rates of Fe and Mg in chromite are considerable, with estimates ranging from a factor of 1.55 in the case of Fe in aluminous spinel (Table 2, Liermann & Ganguly, 2002) to potentially as large as a factor of several hundred (Ozawa 1984). Contrasting this to the Fe-Mg inter-diffusion rates as given by Chakraborty (1997), for which there is only a factor of ~0.17 uncertainty (see Table 2), olivine is therefore the more reliable species from which to calculate cooling rates.

Discrepancy between high- and low-temperature cooling rates

The same "gross mismatch" between high- and low-temperature cooling rates noted by Ganguly et al. (2013, 2016) for H-chondrites is observed in all 5 of my H-chondrite samples, namely, that cooling rates for H chondrites are much faster (~1-1000 ^{o}C/kyr) in the temperature range of ~700-1000 ^{o}C as recorded by the pyroxene and olivine-chromite systems than those recorded by metals at <600 ^{o}C (~10^{-4}-10^{-2} ^{o}C/kyr). The 5 L-chondrite samples also, for the most part, display such a cooling path, with the exception of Park, which cooled quickly (~1 ^{o}C/kyr for metals) throughout its history. The

cooling rates recorded by silicate and oxide phases at high temperatures are simply too fast to be consistent with those predicted by onion-shell cooling models such as Monnereau et al. (2013) and Harrison & Grimm, (2010).

High-temperature cooling rates predicted by an onion-shell parent body model can be estimated from the temperature vs. time curves constructed in Monnereau et al. (2013). This model predicts cooling rates of approximately 10 ^{o}C/Myr through temperatures of ~600-1000 ^{o}C. This is in disagreement with the results found here, as well as the results found in Ganguly et al. (2013) and Ganguly et al. (2016), which used a different methodology. The data in this study are instead in support of the two-stage cooling model of Ganguly et al. (2013, 2016), in which the H and LL chondrite parent bodies were disrupted by impact(s) while they were at or near peak metamorphic temperatures, and were cooled quickly at high temperatures due to temporary dispersal into the vacuum of space. Lowered cooling rates below ~600 ^{o}C would then reflect re-accretion and burial of the ejecta material while it was still warm. At representative cooling rates of ~1 ^{o}C/yr, corresponding to the cooling rates determined for orthopyroxene and olivine, an object which is initially at ~900 ^{o}C will take ~300 years to cool through temperatures recorded by silicates and oxides. This rough timescale of rubble-pile re-accretion can be used to approximate the number of orbital periods necessary to re-assemble a rubble-pile after a catastrophic impact using Kepler's 3rd law:

$$\frac{R^3}{P^2} = 7.469 * 10^{-6}$$

where R is an object's semi-major axis (i.e. the long axis of an elliptical orbit) in astronomical units (AU) and P is its orbital period in days. The asteroid belt mostly lies between 2 to 3 AU distance from the sun, corresponding to orbital periods of ~2.75 to ~5 terrestrial years, respectively. Assuming a 1 ^{o}C/year cooling rate in the space environment and a temperature loss of 300 ^{o}C, re-accretion would then occur over ~110 orbital periods at 2 AU and ~60 orbital periods at 3 AU.

Parent body disruption temperature

The impact disruption necessary to create such mismatched cooling histories would necessarily have occurred above 600 ^{o}C. Otherwise, metals would record fast cooling rates, and silicates and oxides would record slow cooling rates indicative of onion-shell cooling at depth within the host planetesimal – cooling profiles opposite to what were obtained here. The weaker zoning trends seen in the L-chondrites might indicate that its disruptive impact occurred at higher temperatures, thus cutting off retrograde metamorphism sooner than in the case of the H-chondrites.

SHOCK EFFECTS

On otherwise geologically inert small bodies, the only large-scale process occurring after early radiogenic metamorphism is the occasional impact with another body. Many meteorites therefore display unambiguous evidence of shock processes, since there is nothing else to overprint shock signatures. Shock can strongly deform mineral fabrics and is readily seen using optical microscopy techniques developed by Stoffler et al. (1991). Shock heating can reset low-temperature thermometers and

chronometers, such as by annealing of ^{244}Pu fission tracks and driving away radiogenic Ar. Samples of chondrites which are both high petrographic type and low shock stage are decidedly in the minority, especially for the L-chondrites. Shock stage, on average, tends to be higher for L-chondrites (Stoffler et al., 1991). As a consequence, considerably less data, both thermometric and radiometric, are available on the L-chondrites with regard to the early portion of their history. The metamorphic histories of the H-chondrites have been better studied (e.g. Taylor et al., 1987, Scott et al., 2014, Ganguly et al., 2013 & 2016) than that of the L-chondrites.

Shock effects for a suite of 30 H-chondrite (types 3-6) samples with maximum shock stages of S3 were evaluated by Scott et al. (2014) using the method of Stoffler et al. (1991) and no correlation was found between either shock stage or petrographic type. The conclusions of Trieloff et al. (2003) are therefore an artifact of small sample size, as the effects of shock, at least up to stage S3, do not affect measured cooling rates (Scott et al., 2014). This is also borne out by ^{40}Ar-^{39}Ar ages which do not fit with the model of Trieloff et al. (2003) (Scott et al 2014). When shock effects are detected in silicates according to the standard method of Stoffler et al. (1991), reheating is almost always recorded by the metals as well (Bennet and McSween, 1996a) in shock stages 4-6, some of the time in shock stage 3, and none in S1-S2. When only the shock stage S1 chondrites are considered, there is even more overlap between the cooling rates for the different petrographic types (Scott et al., 2014).

Shock re-heating

Re-heating due to shock effects also plays a role in the observed Ni profiles, as is seen in the case of Morrow County, the most strongly shocked (S5) sample used in this study. A large proportion of the metal grains measured in Morrow County were martensites. The Ni profiles were also flattened in the rims when compared to grains in the other samples, such as seen in fig. 26. This is probably due to Ni moving back into the now-shrinking kamacite grain according to the sub-solidus Fe-Ni phase diagram of Reisener and Goldstein, (2003a) (since it is beginning to re-equilibrate at the higher temperature induced by shock) and since grain-boundary diffusion is faster than grain-body diffusion, the rims will see this effect first. The short duration of the heating event ensures that subsequent cooling occurs too quickly to erase this altered profile. Despite these effects, however, metallographic data for Morrow County plotted coherently at approximately 10 ^{o}C/Myr. Thus, while shock heating certainly has effects such driving away Ar (Rubin 2004) and annealing ^{244}Pu fission-decay tracks (Pellas & Storzer, 1981), it does not (at least up to shock stage S5) appear to consistently reset metallographically recorded cooling rates. In Holbrook, which was shocked to stage S4, this effect is also present, but to a lesser extent than in Morrow County.

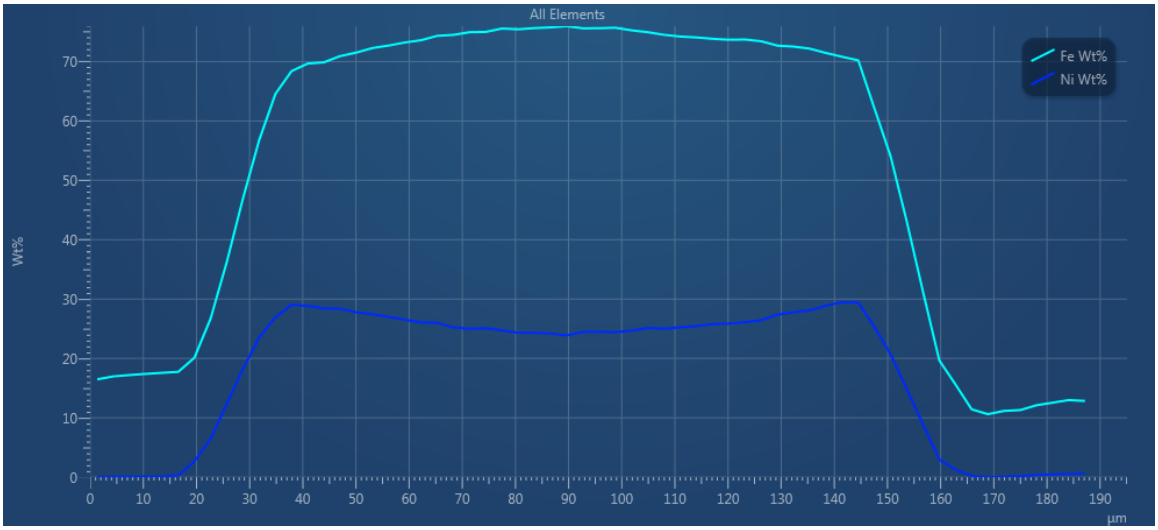

Figure 26. Morrow County linescan 5, showing the effect of shock heating on Ni profiles. The formerly tetrataenite rims have been smoothed out to taenite but the central Ni content of the taenite grain core remains apparently unaffected.

Evidence for syn-metamorphic shock:

Impact events capable of causing shock metamorphism were occurring while both H- and L-chondrite parent bodies were still hot (Rubin and Jones, 2003, Rubin 2004, Ruzicka et al., 2015, Ruzicka and Hugo, 2018). There is crystallographic evidence of annealing of shock features in olivine for otherwise apparently low-shock samples (Ruzicka et al., 2015, Ruzicka & Hugo, 2018). Given this evidence of impact processing, it becomes pertinent to investigate whether this is more consistent with an onion-shell or a rubble-pile parent body during this early stage of the parent body histories. The presence of proposed high-shock-stage indicators such as chromite-plagioclase pods and metal-troilite intergrowths, coupled with the absence in many cases of optical indicators such as planar fractures and undulose/mosaicized extinction in olivine, show that shock events were common when the parent bodies were still warm, and that shock features

were partially annealed away (Rubin 2003, 2004). Selecting only low shock stage samples as Trieloff et al. (2003) did may skew the results towards erroneously low cooling rates both as an artifact of small sample size (Scott et al., 2014) and selectively bias towards sampling of deep interiors which would have escaped the brunt of shock processing.

Microstructures of olivine and troilite grains in Kernouve, Portales Valley, and Park show evidence of shock disturbance at high (700 – 1000 ^{o}C) temperatures which was partially annealed away (Ruzicka et al., 2015, Ruzicka & Hugo, 2018), probably by burial in warm material (Ruzicka & Hugo, 2018). Morrow County, Bruderheim, and Leedey, by contrast, do not show evidence of microstructural annealing and appear to have undergone shock at low temperatures followed by rapid cooling (Ruzicka et al., 2015). This is despite the findings in this study which indicate that all samples were cooled quickly from high temperatures and slowly at low temperatures, with minor though detectable shock disturbance of metal in some samples. This would seem to indicate that while crystallography is reset by later cold-shock events, major-element chemistry of pyroxene, olivine, and chromite phases is not, unlike other more thermally-sensitive systems such as ^{40}K-^{40}Ar and ^{244}Pu fission-tracks. This widens the array of possible samples that this type of thermometric analysis can potentially be used for.

TWO-STAGE COOLING MODEL

A marked contrast between high- and low-temperature cooling rates has already been observed with Kernouve, an H6 chondrite sample used in this study. The pyroxene cooling rates obtained by Ganguly et al. (2013) for two H6 chondrites, Kernouve and Guarena, are 100 ^{o}C/Kyr, 3-4 orders of magnitude higher than what is predicted by Monnereau et al. (2013) for deeply buried material in an onion-shell parent body. However, Kernouve is already known to have cooled metallographically at a rate of 10 ^{o}C/Myr at ~550 ^{o}C (Krot et al., 2012). A major slowdown in cooling rates must therefore have occurred at some temperature above 500 ^{o}C but no higher than 700 ^{o}C (Ganguly et al., 2013), likely by some change in the physical environment (Ganguly et al., 2013). These data can be combined with phosphate ^{207}Pb-^{206}Pb ages (Gopel et al., 1994) and feldspar ^{39}Ar-^{40}Ar ages (Trieloff et al., 2003) in order to construct cooling paths for types 4, 5, and 6 (Ganguly et al., 2013), shown in fig. 27 (Ganguly et al., 2013). The type 4 chondrite Forest Vale had rapid cooling throughout its history, the two type 5 chondrites Allegan and Richardton initially cooled rapidly and then were disrupted slightly below 700 ^{o}C until cooling through ^{39}Ar-^{40}Ar closure; for the type 6 chondrites, the young ages both from ^{207}Pb-^{206}Pb and ^{39}Ar-^{40}Ar require a period of slower cooling after this 700 ^{o}C disruption, as type 6 cooling rates were essentially the same as those for type 5.

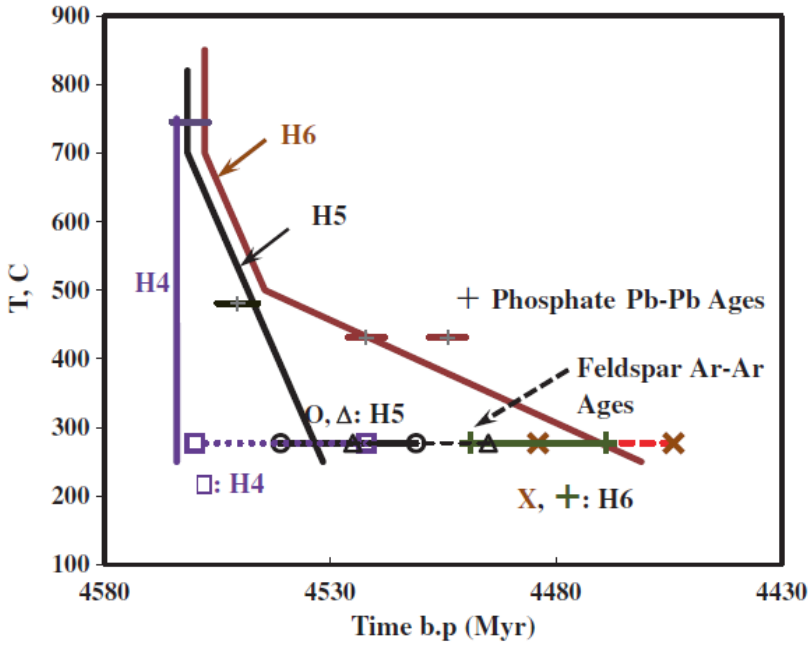

Figure 27. From Ganguly et al 2013, fig. 11 in that paper. Time-integrated cooling pathways for an H4 chondrite (Forest Vale), two H5 chondrites (Allegan and Richardton) and two H6 chondrites (Kernouve and Guarena); showing rapid early cooling of type 6 material followed by slowed cooling at around 500 °C.

The range of olivine-spinel equilibration temperatures is also the same for H- and L-chondrites of types 4, 5, and 6 (Wlotzka 2005). Olivine-spinel data from Kessel et al. (2007) also clearly show the similarity of the closure temperature ranges for petrographic types 4-6. Olivine-spinel closure temperatures for types 3.7 to 3.8 chondrites are lower, averaging 650-660 °C (Wlotzka 2005). This is both a higher and more restricted range of temperatures than would be expected from onion-shell style cooling behavior, such as that modeled by Miyamoto et al. (1981) (Wlotzka 2005). This suggests that the main factor between the increasing textural integration of increasing petrographic types is longer net heating durations rather than higher peak temperatures (Wlotzka 2005). An implication of this is that type 3 chondrites are where the majority of

metamorphic evolution occurs, such as Fe-Mg equilibration between mafic silicates, since the main difference between types 4 to 6 lies in textural maturity, which places limits on the van Schmus and Wood, (1967) classification scheme (Wlotzka 2005).

A two-stage model is therefore necessary to explain this temperature information by the random distribution of fragments of different petrographic types in a rubble pile which formed while the asteroid was still hot (Ganguly et al., 2013, Wlotzka 2005). An early disruption of an onion-shell body accounts for early fast cooling (Ganguly et al., 2013, Wlotzka 2005). The remaining fragments of the parent body may then have been reassembled in different configurations during subsequent impacts before being covered in a thermally insulating blanket of newly accreted nebular material or surface ejecta, accounting for the observed slowdown in cooling for the H5 and H6 material (Ganguly et al., 2013). The newly formed rubble pile would have had a maximum temperature of ~825 ^{o}C (Wlotzka 2005). Types 4 and 5 would be expected to continue to undergo metamorphism to type 6 if they are transported to a higher temperature region than before (Wlotzka 2005). There should be, however, in a rubble pile with a random new fragment distribution with respect to the original onion shell, type 4 to type 6 material which would have re-equilibrated at the lower temperatures in the exterior regions of the rubble pile (Wlotzka 2005), and thus have recorded slower cooling rates due to this more extensive compositional re-adjustment (Wlotzka 2005).

Olivine and Cr-spinel could still equilibrate at these temperatures, as seen in types 3.7 and 3.8, but this is outside the temperature range observed for these samples

(Wlotzka 2005). Therefore, types 4 to 6 were somehow not re-equilibrated to the type 3.7 to 3.8 regions with a closure temperature of ~650-660 ^{o}C (Wlotzka 2005). This would mean that the late-accreting nebular material would not then have been mixed into the rubble-pile interior by impact processing, and thus remain isolated from higher type material (Ganguly et al., 2013). Such low-type material would instead serve as a regolith blanket which insulates the interior of the rubble pile while remaining relatively unaffected by metamorphism (Ganguly et al., 2013).

Table 4 lists cooling rates and closure temperatures deemed most reliable in this study. Values listed for each sample are the averages of values obtained for rim and "int" grain positions (excepting olivines in Leedey, for which there is only data for grain rims), with grain cores having been discarded for reasons explained above. Orthopyroxene and olivine were used instead of clinopyroxene and chromite, respectively, for reasons outlined above. Uncertainties in metallographic cooling rates are taken to be a factor of 2.5 (Wood 1967). Errors in olivine closure temperatures are averages of errors calculated from individual measurements.

Table 4. Averaged cooling rates, in units of Celsius per thousand years, for orthopyroxene, olivine, and metal, at their respective temperatures. Values of cooling rate and closure temperature obtained for rim and intermediate positions in orthopyroxene and olivine are averaged together to produce the values listed here. Errors for pyroxene closure temperatures are from Nakamuta et al (2017). Errors in cooling rates for both pyroxene and olivine are standard deviations of cooling rates calculated for individual mineral pairs using the original Dodson (1973) formulation. Errors in olivine closure temperatures are averages of errors propagated through the Wlotzka (2005) formulation using standard deviations of stoichiometric compositions for each sample. Errors in metallographic closure temperatures are standard deviations from individual measurements. Metallographic cooling rates are averages of those obtained for individual metal grains.

	Orthopyroxene		Olivine		Metal	
Sample name	T (Celsius)	Cooling rate (C/kyr)	T (Celsius)	Cooling rate (C/kyr)	T range (Celsius)	Cooling rate (C/kyr)
H-chondrites						
Butsura	769±20	3700±642	679±61	590±44	505±35 - 383±97	0.0054
Estacado	785±20	833±135	691±57	648±305	470±34 - 350±36	0.0014
Kernouve	799±20	2400±1180	692±59	740±148	429±47 - 307±77	0.0012
Portales Valley	858±20	2825±582	696±41	630±24	489±40 - 340±72	0.0019
Queen's Mercy	788±20	5200±2070	672±60	2700±1700	479±30 - 301±63	0.0011
L-chondrites						
Bruderheim	771±20	1460±474	698±51	1850±78	508±7 - 381±21	0.0098
Holbrook	822±20	5340±3000	702±59	8250±1076	549±32 - 433±28	0.039
Leedey	781±20	1460±424	697±53	1770±20	501±27 - 362±64	0.0021
Morrow County	756±20	578±111	704±57	1055±71	538±18 - 481±21	0.012
Park	767±20	2250±26	745±43	4325±181	611±21 - 486±38	0.7

CHAPTER 6: CONCLUSIONS

H- and L-chondrites show broadly similar histories, in that they were quickly cooled at high temperatures, and slowly cooled at lower temperatures, with L-chondrites being more variable in the latter respect. These cooling histories are much too fast at high temperatures to be consistent with modelled thermal evolutions of onion-shell bodies composed of ordinary chondrite material with short-lived radioactive nuclide decay as their primary heat source. The results of this project are therefore firmly in support of the two-stage cooling model of ordinary chondrite thermal evolution as proposed by Ganguly et al. (2013). Peak temperature has little effect on closure temperature or calculated cooling rate. Shock does not affect silicate or silicate-oxide thermometers, and while it shows effects in Fe-Ni profiles in metal grains, does not destroy cooling rate information.

References

Bennet, M.E. and McSween, H.Y. 1996a, Shock features in iron-nickel metal and troilite of L-group ordinary chondrites. Meteoritics and Planetary Science, vol. 31, pp. 255-264.

Bizzaro, M. et al., 2005, Rapid timescales for accretion and melting of differentiated planetesimals inferred from ^{26}Al-^{26}Mg chronometry. The Astrophysical Journal, vol. 632, pp. 41-44.

Britt, D.T. et al., 1987, Asteroid Density, Porosity, and Structure. Asteroids III, pp. 485-500.

Bottke, W.F. et al., 2005, The fossilized size distribution of the main asteroid belt. Icarus, vol. 175, pp. 111-140.

Ciesla, F.J. et al., 2013, Thermal consequences of impacts in the early solar system. Meteoritics and Planetary Science, vol. 48, no. 12, pp. 2559-2576.

Chakraborty, S., 1997, Rates and mechanisms of Fe-Mg interdiffusion in olivine at 980^{o} – 1300 ^{o}C. Journal of Geophysical Research, vol. 102, no. B6, pp. 12,317-12,331, June 10th, 1997.

Dodson, M.H., 1973, Closure in geochronological and petrological systems. Contributions to Mineralogy and Petrology, vol. 40, pp. 259-274.

Dodson, M.H., 1986, Closure profiles in cooling systems. Kinetics and Transport in Silicate and Oxide Systems, pp. 145-154, Materials Science Forum, Min. Soc. U.K.

Dohmen, R. et al., 2007, Fe–Mg diffusion in olivine I: experimental determination between 700 and 1,200 C as a function of composition, crystal orientation and oxygen fugacity. Physics and Chemistry on Minerals, vol. 34, pp. 389-407.

Folco, L. et al., 1996, Unshocked equilibrated H-chondrites: A common low-temperature record from orthopyroxene iron-magnesium ordering. Meteoritics and Planetary Science, vol. 31, pp. 388-393.

Fujiwara, A. et al., 2006, The rubble-pile asteroid Itokawa as observed by Hayabusa. Science, vol. 312, pp. 1330-1334.

Gaffey, M.J. & Gilbert, S.L., 1998, Asteroid 6 Hebe: The probable parent body of the H-type ordinary chondrites and the IIE iron meteorites. Meteoritics and Planetary Science, vol. 33, pp. 1281-1295.

Ganguly, J. and Tazzoli, V., 1994, Fe^{2+}-Mg interdiffusion in orthopyroxene: Retrieval from the data on intra crystalline exchange reaction. American Mineralogist, vol. 79, pp. 930-937.

Ganguly, J. and Tirone, M., 1999, Diffusion closure temperature and age of a mineral with arbitrary extent of diffusion: theoretical formulation and applications. Earth and Planetary Science Letters, vol. 170, pp. 131-140.

Ganguly, J. and Tirone, M., 2001, Relationship between cooling rate and cooling age of a mineral: Theory and applications to meteorites. Meteoritics and Planetary Science, vol. 36, pp. 167-175.

Ganguly, J. et al., 2013, H-chondrite parent asteroid: A multistage cooling, fragmentation, and re-accretion history constrained by thermometric studies, diffusion kinetic modeling and geochronological data. Geochimica et Cosmochimica Acta, vol. 105, pp. 206-220.

Ganguly, J. et al., 2016, Cooling rates of LL, L, and H chondrites and constraints on the duration of peak thermal conditions: Diffusion kinetic modeling and implication for fragmentation of asteroids and impact resetting of petrologic types. Geochimica et Cosmochimica Acta, vol. 192, pp. 135-148.

Grimm 1985, Penecontemporaneous metamorphism, fragmentation, and reassembly of ordinary chondrite parent bodies. Journal of Geophysical Research, vol. 90(B2), pp. 2022-2028.

Gopel, C. et al., 1994, U-Pb systematics of phosphates from equilibrated ordinary chondrites. Earth and Planetary Science Letters, vol. 121, pp. 153-171.

Harrison, K.P. and Grimm, R.E., 2010, Thermal constraints on the early history of the H-chondrite parent body reconsidered. Geochimica et Cosmochimica Acta, vol. 74, pp. 5410-5423.

Henke, S. et al., 2012, Thermal history modelling of the H-chondrite parent body. Astronomy and Astrophysics, vol 545, article no. A135.

Hevey, P.J. and Sanders, I.S., 2006, A model for planetesimal meltdown by ^{26}Al and its implications for meteorite parent bodies. Meteoritics and Planetary Science vol. 41, no. 1, pp. 95-106.

Kessel, R. et al., 2007, The thermal history of equilibrated ordinary chondrites and the relationship between textural maturity and temperature. Geochimica et Cosmochimica Acta, vol. 71, pp. 1855-1881.

Kiel, K. et al., 1994, Catastrophic fragmentation of asteroids: evidence from meteorites. Planetary and Space Science, vol. 42, no. 12, pp. 1109-1122.

Kita, N.T. and Ushikubo, T., 2012, Evolution of protoplanetary disk inferred from ^{26}Al chronology of individual chondrules. Meteoritics and Planetary Science, vol. 47, No. 7, pp. 1108-1119.

Kleine, T. et al., 2008, Hf-W thermochronometry: Closure temperatures and constraints on the accretion and cooling history of the H chondrite parent body. Earth and Planetary Science Letters, vol. 270, pp. 106-118.

Krot, T.A. et al., 2012, Thermal histories of H3-H6 chondrites and their parent asteroid from metallographic cooling rates and cloudy taenite dimensions. 75th Annual Meteoritical Society Meeting, Abstract #5372.

Kruijer, T.S. et al., 2012, Hf-W chronometry of core formation in planetesimals inferred from weakly irradiated iron meteorites. Geochimica et Cosmochimica Acta, vol. 99, pp. 287-304.

Liermann, H.P. and Ganguly, J., 2002, Diffusion kinetics of Fe^{2+} and Mg in aluminous spinel: Experimental determination and applications. Geochimica et Cosmochimica Acta, vol. 66, no. 16, pp. 2903-2913.

Lindsley, D.H., 1983, Pyroxene thermometry. American Mineralogist, vol. 68, pp. 477-493.

Luan, J. and Goldreich, P., 2015, Thermal conductivity of rubble piles. The Astrophysical Journal, vol. 814, no. 1.

Marset, M. et al., 2017, 3D shape of asteroid (6) Hebe from VLT/SPHERE imaging: Implications for the origin of ordinary H-chondrites. Astronomy and Astrophysics.

Miyamoto, M. et al., 1981, Ordinary chondrite parent body: An internal heating model. Proceedings of the Lunar and Planetary Science Conference, 12th Edition, pp. 1145-1152.

Monnereau, M., et al., 2013, Thermal history of the H-chondrite parent body: Implications for metamorphic grade and accretionary time-scales. Geochimica et Cosmochimica Acta, vol. 119, pp. 302-321.

Nakamura, T. et al., 2011, Itokawa dust particles: A direct link between S-type asteroids and ordinary chondrites. Science, vol. 333, pp. 1113-1116.

Nakamuta, Y. et al., 2017, Effect of $NaCrSi_2O_6$ component on Lindsley's pyroxene thermometer: An evaluation based on strongly metamorphosed LL chondrites. Meteoritics and Planetary Science, vol. 52, no. 3, pp. 511-521.

Nesvorny, D. et al., 2009, Asteroidal source of L-chondrite meteorites. Icarus, vol. 200, pp. 698-701.

Ozawa, K., 1984, Olivine-spinel geospeedometry: Analysis of diffusion-controlled Mg-Fe^{2+} exchange. Geochimica et Cosmochimica Acta, vol. 48, pp. 2597-2611.

Pellas, P. and Storzer, D., 1981, ^{244}Pu Fission track thermometry and its application to stony meteorites. Proceedings of the Royal Society of London, vol. A 374, pp. 253-270.

Perera, V. et al., 2016, The spherical Brazil Nut Effect and its significance to asteroids. Icarus, vol. 278, pp. 194-203.

Petry, C. et al., 2004, Experimental determination of Ni diffusion coefficients in olivine and their dependence on temperature, composition, oxygen fugacity, and crystallographic orientation. Geochimica et Cosmochimica Acta, Vol. 68, No. 20, pp. 4179-4188.

Reisener, R.J. and Goldstein, J.I., 2003a, Ordinary chondrite metallography: Part 1. Fe-Ni taenite cooling experiments. Meteoritics and Planetary Science, vol. 38, no. 11, pp. 1669-1678.

Reisener, R.J. and Goldstein, J.I., 2003b, Ordinary chondrite metallography: Part 2. Formation of zoned and unzoned metal particles in relatively unshocked H, L, and LL chondrites, Meteoritics and Planetary Science, vol. 38, no. 11, pp. 1679-1696.

Rubin, A.E. and Jones, R.H., 2003, Spade: An H chondrite impact-melt breccia that experienced post-shock annealing. Meteoritics and Planetary Science, vol. 38, no.10, pp. 1507-1520.

Rubin, A.E., 2004, Post-shock annealing and post-annealing shock in equilibrated ordinary chondrites: Implications for the thermal and shock histories of chondritic asteroids. Geochimica et Cosmochimica Acta, vol. 68, no. 3, pp. 673-689.

Ruzicka, A. et al., 2005, Portales Valley: petrology of a metallic-melt meteorite breccia. Meteoritics and Planetary Science, vol. 40, no. 2, pp. 261-295.

Ruzicka, A., 2014, Silicate-bearing iron meteorites and their implications for the evolution of asteroidal parent bodies. Geochemistry, vol. 74, pp. 3-48.

Ruzicka, A. et al., 2015, Deformation and thermal histories of ordinary chondrites: Evidence for post-deformation annealing and syn-metamorphic shock. Geochimica et Cosmochimica Acta, vol. 163, pp. 219-233.

Ruzicka, A. et al., 2017, Petrogenesis of Miller Range 07273, a new type of anomalous melt breccia: Implications for impact effects on the H chondrite asteroid. Meteoritics and Planetary Science, vol. 52, no. 9, pp. 1963-1990.

Ruzicka, A. and Hugo, R., 2018, Electron backscatter diffraction (EBSD) study of seven heavily metamorphosed chondrites: Deformation systematics and variations in pre-shock temperature and post-shock annealing. Geochimica et Cosmochimica Acta, vol. 234, pp. 115-147.

Sack, R.O. and Ghiorso, M.S., 1991b, Chromian spinels as petrogenetic indicators: Thermodynamics and petrological applications. American Mineralogist, vol. 76, pp. 827-847.

Sanders, I.S., and Scott, E.R.D., 2012, The origin of chondrules and chondrites: Debris from low-velocity impacts between molten planetesimals? Meteoritics and Planetary Science, vol. 47, no. 12, pp. 2170-2192.

Scott, E.R.D. and Rajan, R.S., 1981, Metallic minerals, thermal histories, and parent bodies of some xenolithic, ordinary chondrites. Geochimica et Cosmochimica Acta, vol. 45, pp. 53-67.

Scott, E.R.D. et al., 2014, Thermal and Impact History of the H chondrite parent asteroid during metamorphism: Constraints from metallic Fi-Ni. Geochimica et Cosmochimica Acta, vol. 136, pp. 13-37.

Slater-Reynolds, V. and McSween, H.Y., 2005, Peak metamorphic temperatures in type 6 ordinary chondrites: An evaluation of pyroxene and plagioclase geothermometry. Meteoritics and Planetary Science, vol. 40, no. 5, pp. 745-754.

Stoffler, D. et al., 1991, Shock metamorphism of ordinary chondrites. Geochimica et Cosmochimica Acta, vol. 55, pp. 3845-3867.

Suzuki, A.M. et al., 2008, Cr and Al diffusion in chromite spinel: experimental determination and its implication for diffusion creep. Physics and Chemistry of Minerals, vol. 35, pp. 433-445.

Taylor, G.J. et al., 1987, Original Structures, and Fragmentation and Reassembly Histories of Asteroids: Evidence from Meteorites. Icarus, vol. 69, pp. 1-13.

Tomkins, A., 2009, What metal-troilite textures can tell us about post-impact metamorphism in chondrite meteorites. Meteoritics and Planetary Science, vol. 44, no. 8, pp. 1133-1149.

Trieloff, M. et al., 2003, Structure and thermal history of the H-chondrite parent body revealed by thermochronometry. Nature, vol. 422, pp. 502-506.

van Schmus, W.R. and Wood, J.A., 1967, A chemical-petrologic classification of the chondritic meteorites. Geochimica et Cosmochimica Acta, vol. 31, pp. 747-765.

Wilkinson, S.L. et al., 2002, An estimate of Eros's porosity and implications for internal structure. Icarus, vol. 155, pp. 94-103.

Williams, C.V. et al., 1985, Petrology of the Cangas de Onis and Nulles regolith breccias: Implications for parent body history. Meteoritics, vol. 20, pp. 331-345.

Willis, J. and Goldstein, J.I., 1981, A revision of metallographic cooling rate curves for chondrites. Lunar Planet. Sci. 12B, 1135-1143.

Wlotzka, F., 2005, Cr spinel and chromite as petrogenetic indicators in ordinary chondrites: Equilibration temperatures of petrologic types 3.7 to 6. Meteoritics and Planetary Science, vol. 40, no. 11, pp. 1673-1702.

Wood, J. A., 1967, Chondrites: Their Metallic Minerals, Thermal Histories, and Parent Planets. Icarus, vol. 6, pp. 1-49.

Yomogida, K. and Matsui, T., 1984, Multiple parent bodies of ordinary chondrites. Earth and Planetary Science Letters, vol. 68, pp. 34-42.

Zhang, X., et al., 2010, Ca-Mg diffusion in diopside: tracer and chemical inter-diffusion coefficients. Contributions to Mineralogy and Petrology, vol. 159, pp. 175-186.

Zhang, Y., 2008, Geochemical Kinetics. Princeton University Press, Princeton, NJ.

APPENDIX A: Clinopyroxene data

This appendix contains compositional data measured from clinopyroxene grains for each sample. Closure temperatures calculated according to the Nakamuta et al. (2017) method are presented also, as well as the position of the spot datum within the grain and the distance to the nearest edge of the grain in microns from the spot datum. All concentrations are given as stoichiometrically normalized to 6 oxygens.

Bruderheim (L6)

pair #	Si	Al	Mg	Ca	Fe	Na	Cr	Ti	Tc (Celsius)	spot position	dist to nearest edge (μm)
2p1	1.992	0.020	0.887	0.883	0.150	0.031	0.014	0.010	790	rim	5
2p3	1.948	0.027	0.864	0.855	0.253	0.030	0.015	0.013	765	rim	3
2p5	1.987	0.023	0.888	0.859	0.158	0.038	0.021	0.014	857	core	7
2p7	1.986	0.022	0.887	0.870	0.158	0.037	0.018	0.012	818	core	9
2p12	1.989	0.021	0.890	0.905	0.126	0.031	0.011	0.011	739	int	6
2p13	1.992	0.021	0.887	0.875	0.150	0.034	0.016	0.010	815	rim	4
2p20	1.990	0.019	0.889	0.872	0.153	0.034	0.018	0.010	822	int	5
2p21	1.992	0.019	0.888	0.909	0.132	0.029	0.011	0.009	720	core	8

Butsura (H6)

pair #	Si	Al	Mg	Ca	Fe	Na	Cr	Ti	Tc (Celsius)	spot position	dist to nearest edge (μm)
2p1	1.985	0.025	0.905	0.873	0.127	0.036	0.020	0.013	844	int	4
2p1	1.985	0.024	0.907	0.873	0.125	0.037	0.020	0.014	846	int	5
2p2	1.988	0.024	0.907	0.873	0.125	0.037	0.018	0.013	846	core	2
2p3a	1.986	0.023	0.907	0.892	0.116	0.035	0.016	0.012	792	rim	4
2p3a	1.987	0.023	0.909	0.883	0.121	0.034	0.018	0.013	818	core	11
2p3b	1.988	0.022	0.907	0.883	0.120	0.035	0.018	0.013	819	int	8
2p4	1.987	0.024	0.907	0.894	0.115	0.033	0.016	0.012	787	int	7
2p4	1.982	0.025	0.909	0.884	0.119	0.036	0.016	0.014	809	rim	2

2p5	1.979	0.032	0.892	0.881	0.114	0.037	0.023	0.019	828	int	3
2p5	1.991	0.023	0.912	0.874	0.120	0.036	0.017	0.013	849	int	3
2p6	1.970	0.024	0.900	0.861	0.168	0.039	0.019	0.013	802	rim	8
2p8	1.988	0.023	0.907	0.885	0.117	0.036	0.016	0.013	816	int	3
2p9	1.989	0.024	0.910	0.878	0.119	0.038	0.018	0.012	836	core	6
2p10	1.988	0.022	0.913	0.889	0.116	0.034	0.014	0.012	803	core	5
2p11	1.989	0.025	0.907	0.864	0.127	0.038	0.020	0.013	872	rim	6
2p13	1.986	0.023	0.908	0.880	0.120	0.035	0.018	0.013	829	rim	8

Estacado (H6)

pair #	Si	Al	Mg	Ca	Fe	Na	Cr	Ti	Tc (Celsius)	spot position	dist to nearest edge (μm)
2p2	1.974	0.038	0.879	0.855	0.170	0.033	0.022	0.013	862	int	8
2p1	1.983	0.024	0.905	0.889	0.115	0.036	0.022	0.013	805	rim	8
2p10	1.988	0.023	0.909	0.850	0.137	0.035	0.026	0.014	910	int	7
2p3	1.984	0.024	0.908	0.859	0.134	0.040	0.025	0.014	881	int	7
2p5	1.984	0.025	0.910	0.868	0.125	0.034	0.024	0.015	862	int	9
2p6	1.986	0.026	0.898	0.865	0.131	0.038	0.027	0.013	867	int	11
2p8	1.994	0.023	0.905	0.859	0.126	0.037	0.021	0.014	889	int	15
2p7	1.982	0.026	0.904	0.882	0.126	0.033	0.023	0.014	817	rim	4
2p9	1.986	0.024	0.905	0.892	0.116	0.029	0.018	0.014	792	rim	6
2p11	1.987	0.022	0.905	0.862	0.138	0.033	0.024	0.013	866	core	9
2p13	1.989	0.024	0.900	0.867	0.131	0.036	0.021	0.013	857	int	4
2p14	1.995	0.019	0.910	0.860	0.131	0.034	0.023	0.010	889	core	10
2p12	1.990	0.022	0.904	0.876	0.123	0.038	0.020	0.013	839	int	7
2p16	1.993	0.022	0.901	0.905	0.100	0.027	0.018	0.011	784	int	5
2p15	1.993	0.023	0.905	0.883	0.112	0.032	0.019	0.013	836	int	6
2p17	1.988	0.023	0.905	0.855	0.128	0.039	0.025	0.014	897	int	7

2p18	1.986	0.025	0.904	0.876	0.119	0.035	0.023	0.015	840	int	10
2p19	1.986	0.024	0.904	0.869	0.124	0.033	0.025	0.015	862	core	13
2p23	1.987	0.026	0.906	0.861	0.127	0.035	0.025	0.015	889	int	15
2p24	1.988	0.022	0.907	0.878	0.124	0.032	0.021	0.013	829	int	12
2p20	1.981	0.022	0.906	0.872	0.126	0.035	0.023	0.014	845	core	9
2p22	1.989	0.023	0.908	0.858	0.126	0.039	0.022	0.016	890	rim	5
2p21	1.987	0.024	0.902	0.859	0.127	0.036	0.027	0.015	891	rim	9
2p25	1.981	0.025	0.908	0.875	0.120	0.036	0.023	0.013	845	core	13
2p26	1.990	0.024	0.905	0.864	0.125	0.036	0.026	0.013	885	int	11
2p27	1.987	0.023	0.909	0.862	0.133	0.035	0.023	0.014	871	int	7
2p29	1.984	0.021	0.910	0.868	0.125	0.040	0.025	0.016	862	int	5
2p28	1.993	0.025	0.908	0.857	0.121	0.034	0.027	0.012	930	rim	7
2p30	1.984	0.025	0.895	0.871	0.135	0.035	0.024	0.015	840	core	11
2p31	1.987	0.022	0.909	0.878	0.119	0.032	0.025	0.014	842	int	10
2p33	1.996	0.020	0.899	0.865	0.126	0.035	0.024	0.012	882	rim	8
2p34	1.994	0.022	0.906	0.875	0.118	0.035	0.021	0.012	851	int	6

Holbrook (L6)

pair #	Si	Al	Mg	Ca	Fe	Na	Cr	Ti	Tc (Celsius)	spot position	dist to nearest edge (μm)
2p3	1.993	0.017	0.883	0.855	0.175	0.037	0.025	0.006	854	int	8
2p5	1.987	0.019	0.890	0.858	0.162	0.035	0.027	0.012	857	rim	4
2p9	1.988	0.025	0.882	0.866	0.157	0.033	0.025	0.010	852	int	11
2p11	1.990	0.016	0.911	0.845	0.168	0.030	0.018	0.010	893	rim	4
2p12	2.001	0.014	0.894	0.837	0.159	0.034	0.021	0.012	925	int	3
2p16	1.985	0.020	0.891	0.857	0.165	0.030	0.021	0.014	856	rim	5
2p17	1.974	0.026	0.892	0.865	0.167	0.035	0.025	0.015	817	int	6
2p14	2.006	0.011	0.896	0.856	0.158	0.032	0.017	0.008	872	int	9

2p21	1.991	0.018	0.888	0.869	0.159	0.036	0.018	0.012	826	int	4
2p22	1.996	0.017	0.883	0.847	0.163	0.034	0.024	0.012	894	core	4
2p24	1.988	0.020	0.891	0.846	0.180	0.035	0.020	0.012	878	rim	5
2p24	1.992	0.021	0.891	0.845	0.168	0.040	0.025	0.007	890	int	3
2p25	1.993	0.019	0.883	0.836	0.181	0.036	0.023	0.011	902	rim	6
2p27	1.978	0.033	0.870	0.859	0.161	0.039	0.028	0.018	850	int	8
2p26	1.992	0.013	0.888	0.859	0.169	0.029	0.020	0.012	849	int	3
2p31	1.994	0.017	0.893	0.839	0.175	0.036	0.020	0.013	900	rim	4
2p32	1.994	0.017	0.892	0.870	0.151	0.034	0.020	0.010	831	int	0
2p37	1.993	0.017	0.884	0.866	0.165	0.036	0.019	0.007	829	core	7
2p35	1.980	0.033	0.867	0.862	0.164	0.036	0.023	0.019	839	core	13
2p38	1.974	0.036	0.875	0.852	0.165	0.033	0.025	0.019	873	rim	4
2p36	1.964	0.031	0.865	0.855	0.178	0.038	0.039	0.022	852	int	3

Kernouve (H6)

pair #	Si	Al	Mg	Ca	Fe	Na	Cr	Ti	Tc (Celsius)	spot position	dist to nearest edge (μm)
2p2	1.991	0.025	0.909	0.860	0.129	0.036	0.021	0.011	886	rim	15
2p3	1.988	0.026	0.903	0.867	0.129	0.038	0.019	0.014	861	rim	12
2p4	1.986	0.024	0.910	0.867	0.126	0.037	0.019	0.013	864	int	7
2p5	1.989	0.024	0.906	0.876	0.121	0.036	0.019	0.013	840	int	7
2p7	1.989	0.025	0.908	0.859	0.131	0.038	0.020	0.012	884	int	11
2p8	1.987	0.022	0.903	0.894	0.115	0.034	0.017	0.013	788	int	9
2p13	1.987	0.022	0.907	0.873	0.128	0.039	0.019	0.013	843	rim	6
2p14	1.987	0.024	0.907	0.862	0.133	0.039	0.021	0.013	872	int	6
2p15	1.986	0.025	0.908	0.868	0.126	0.038	0.020	0.013	861	int	16
2p16	1.987	0.023	0.906	0.897	0.114	0.033	0.013	0.013	779	int	9
2p19	1.987	0.023	0.912	0.865	0.127	0.038	0.021	0.013	869	int	13

2p20	1.987	0.024	0.907	0.871	0.125	0.039	0.021	0.014	852	core	8
2p22	1.986	0.024	0.908	0.878	0.123	0.038	0.018	0.013	832	int	10

Leedey (L6)

pair #	Si	Al	Mg	Ca	Fe	Na	Cr	Ti	Tc (Celsius)	spot position	dist to nearest edge (µm)
2p8	1.997	0.020	0.893	0.868	0.131	0.035	0.020	0.013	861	int	7
2p9	1.985	0.025	0.899	0.851	0.155	0.037	0.025	0.014	885	int	11
2p10	2.010	0.017	0.893	0.854	0.150	0.038	0.020	0.000	905	rim	3
2p13	1.989	0.023	0.882	0.852	0.158	0.035	0.022	0.014	877	core	19
2p20	1.989	0.023	0.886	0.891	0.129	0.033	0.017	0.011	781	int	9
2p21	1.989	0.023	0.888	0.842	0.160	0.038	0.026	0.010	905	int	9
2p22	1.996	0.026	0.882	0.856	0.143	0.039	0.025	0.014	900	int	9
2p25	1.987	0.022	0.892	0.861	0.150	0.036	0.021	0.013	859	rim	5

Morrow County (L6)

pair #	Si	Al	Mg	Ca	Fe	Na	Cr	Ti	Tc (Celsius)	spot position	dist to nearest edge (µm)
2p7	1.974	0.027	0.882	0.827	0.208	0.037	0.021	0.013	880	rim	5
2p6a	1.993	0.021	0.876	0.869	0.147	0.039	0.018	0.015	833	rim	4
2p6b	1.985	0.024	0.894	0.859	0.149	0.037	0.020	0.014	866	core	9
2p5	1.994	0.017	0.894	0.853	0.159	0.036	0.022	0.009	875	int	5
2p8	1.964	0.029	0.864	0.864	0.192	0.028	0.019	0.012	808	int	9
2p8	1.981	0.024	0.884	0.872	0.161	0.036	0.019	0.012	795	int	5
2p9	1.992	0.022	0.886	0.862	0.147	0.038	0.024	0.013	857	int	7
2p9	1.992	0.020	0.881	0.875	0.144	0.036	0.022	0.014	818	int	10
2p11	1.988	0.021	0.886	0.852	0.160	0.036	0.025	0.013	876	rim	5
2p11	1.988	0.021	0.888	0.872	0.146	0.040	0.025	0.012	827	rim	6
2p13	1.972	0.035	0.856	0.823	0.230	0.033	0.025	0.012	900	rim	5

2p13	1.976	0.025	0.877	0.830	0.205	0.036	0.026	0.011	886	core	10
2p12	1.986	0.023	0.891	0.854	0.161	0.038	0.023	0.013	870	int	10
2p12	1.984	0.023	0.889	0.858	0.155	0.040	0.026	0.013	862	int	10
2p10	1.992	0.019	0.885	0.896	0.143	0.031	0.018	0.010	753	int	12
2p10	1.994	0.017	0.885	0.888	0.144	0.028	0.017	0.011	778	core	17
2p17	1.993	0.023	0.884	0.851	0.156	0.037	0.023	0.014	887	core	4
2p15	1.980	0.024	0.882	0.884	0.146	0.035	0.022	0.016	789	int	10
2p16	1.979	0.030	0.884	0.864	0.155	0.035	0.024	0.017	845	int	5
2p14	1.984	0.021	0.888	0.845	0.172	0.039	0.024	0.012	883	core	8
2p20	1.991	0.020	0.888	0.886	0.136	0.035	0.021	0.011	793	rim	4
2p21	1.988	0.022	0.886	0.853	0.162	0.038	0.025	0.012	872	rim	5
2p19	1.989	0.024	0.882	0.883	0.141	0.032	0.019	0.014	796	int	5
2p22	1.986	0.022	0.883	0.862	0.157	0.032	0.023	0.013	847	rim	4

Park (L6)

pair #	Si	Al	Mg	Ca	Fe	Na	Cr	Ti	Tc (Celsius)	spot position	dist to nearest edge (μm)
2p1	1.987	0.021	0.884	0.890	0.140	0.031	0.015	0.013	776	rim	7
2p6	1.987	0.023	0.885	0.862	0.158	0.038	0.018	0.013	847	core	17
2p7	1.986	0.024	0.888	0.845	0.173	0.038	0.021	0.012	885	int	9
2p10	1.989	0.023	0.887	0.868	0.151	0.038	0.018	0.013	836	int	17
2p14	1.987	0.022	0.884	0.848	0.171	0.039	0.020	0.014	878	int	5
2p18	1.980	0.024	0.882	0.881	0.158	0.036	0.017	0.012	765	rim	10

Portales Valley (H6)

pair #	Si	Al	Mg	Ca	Fe	Na	Cr	Ti	Tc (Celsius)	spot position	dist to nearest edge (μm)
2p1	1.987	0.025	0.910	0.849	0.134	0.038	0.029	0.014	916	int	8
2p1	1.986	0.027	0.903	0.876	0.116	0.039	0.025	0.014	843	int	13
2p6	1.989	0.024	0.903	0.855	0.126	0.040	0.027	0.015	898	rim	8
2p4	1.984	0.025	0.906	0.853	0.134	0.044	0.024	0.014	899	rim	10
2p7	1.988	0.025	0.912	0.844	0.138	0.040	0.029	0.013	925	rim	14
2p8	1.987	0.029	0.909	0.818	0.145	0.043	0.032	0.016	999	int	46
2p5	1.988	0.028	0.913	0.820	0.141	0.042	0.031	0.015	998	int	23
2p2	1.991	0.023	0.918	0.834	0.135	0.041	0.026	0.012	952	rim	11
2p9	1.988	0.027	0.919	0.807	0.143	0.045	0.032	0.017	1024	core	15
2p11	1.987	0.029	0.919	0.816	0.148	0.045	0.029	0.014	992	int	10
2p12	1.986	0.025	0.904	0.854	0.137	0.038	0.026	0.015	893	core	14
2p13	1.984	0.033	0.910	0.816	0.144	0.043	0.031	0.018	1007	int	20
2p14	1.981	0.032	0.905	0.850	0.130	0.044	0.026	0.017	911	int	8
2p17	1.988	0.028	0.913	0.819	0.137	0.045	0.030	0.015	996	int	18
2p15	1.984	0.027	0.916	0.829	0.146	0.038	0.028	0.015	958	int	11
2p19	1.985	0.028	0.906	0.855	0.132	0.038	0.024	0.013	893	rim	17
2p20	1.991	0.022	0.908	0.878	0.125	0.033	0.018	0.009	829	rim	10
2p22	1.982	0.022	0.914	0.838	0.142	0.041	0.026	0.013	928	core	9
2p25	1.984	0.025	0.909	0.846	0.139	0.040	0.027	0.017	913	core	22

Queen's Mercy (H6)

pair #	Si	Al	Mg	Ca	Fe	Na	Cr	Ti	Tc (Celsius)	spot position	dist to nearest edge (µm)
2p1	1.998	0.024	0.889	0.867	0.124	0.031	0.015	0.013	882	core	3
2p2	1.934	0.076	0.875	0.878	0.107	0.041	0.044	0.029	885	int	2
2p5	1.987	0.023	0.913	0.875	0.126	0.035	0.016	0.012	839	int	2
2p6	1.989	0.023	0.910	0.888	0.115	0.033	0.016	0.012	808	rim	4
2p8	2.005	0.016	0.916	0.882	0.104	0.035	0.021	0.002	858	int	3
2p8	2.003	0.015	0.915	0.882	0.104	0.038	0.021	0.003	843	int	3
2p9	1.985	0.034	0.901	0.889	0.100	0.036	0.017	0.016	818	rim	2
2p9	1.986	0.033	0.910	0.881	0.107	0.035	0.018	0.014	845	int	1
2p10	2.002	0.061	0.876	0.859	0.098	0.044	0.016	0.010	1012	int	2
2p10	1.994	0.025	0.908	0.893	0.098	0.033	0.016	0.012	814	rim	2
2p11	1.984	0.030	0.905	0.890	0.111	0.035	0.017	0.015	805	rim	2
2p11	1.986	0.023	0.895	0.897	0.123	0.033	0.016	0.012	768	rim	2
2p12	1.985	0.031	0.900	0.893	0.109	0.034	0.015	0.014	797	int	2
2p12	1.986	0.029	0.907	0.898	0.108	0.033	0.013	0.012	782	rim	1
2p13	1.992	0.026	0.904	0.894	0.110	0.035	0.013	0.010	793	int	2
2p13	1.988	0.023	0.913	0.895	0.115	0.031	0.010	0.010	783	int	1
2p14	2.000	0.022	0.911	0.866	0.119	0.032	0.016	0.011	890	core	2
2p15	1.977	0.042	0.900	0.882	0.104	0.040	0.019	0.017	837	core	1

APPENDIX B: Orthopyroxene data

This appendix contains compositional data measured from orthopyroxene grains for each sample. Closure temperatures calculated according to the Nakamuta et al. (2017) method are presented also, as well as the position of the spot datum within the grain and the distance to the nearest edge of the grain in microns from the spot datum. All concentrations are given as stoichiometrically normalized to 6 oxygens. Na is close to the SEM's detection limit in most measurements for orthopyroxene.

Bruderheim (L6)

pair #	Si	Al	Mg	Ca	Fe	Na	Cr	Ti	Tc (Celsius)	spot position	dist to nearest edge (µm)
2p1	1.994	0.008	1.517	0.027	0.427	0.000	0.002	0.005	774	int	5
2p3	1.992	0.009	1.516	0.025	0.428	0.000	0.004	0.005	755	rim	8
2p5	1.992	0.007	1.520	0.026	0.427	0.000	0.002	0.005	765	int	7
2p7	1.987	0.006	1.523	0.030	0.430	0.000	0.003	0.005	801	rim	9
2p12	1.988	0.009	1.519	0.023	0.432	0.002	0.002	0.006	734	int	18
2p13	1.992	0.006	1.523	0.026	0.428	0.000	0.002	0.005	764	int	16
2p20	1.992	0.008	1.521	0.030	0.423	0.000	0.004	0.005	804	int	6
2p21	1.989	0.008	1.521	0.025	0.430	0.000	0.004	0.004	754	int	7

Butsura (H6)

pair #	Si	Al	Mg	Ca	Fe	Na	Cr	Ti	Tc (Celsius)	spot position	dist to nearest edge (µm)
2p1	1.989	0.008	1.605	0.025	0.343	0.000	0.003	0.005	789	int	3
2p1	1.992	0.009	1.603	0.025	0.346	0.000	0.003	0.004	788	core	4
2p2	1.993	0.009	1.591	0.028	0.347	0.000	0.003	0.005	816	rim	4
2p2	1.990	0.008	1.604	0.024	0.342	0.000	0.004	0.005	780	rim	2
2p3a	1.992	0.008	1.601	0.026	0.344	0.000	0.004	0.006	798	rim	3
2p3a	1.992	0.008	1.605	0.021	0.345	0.000	0.002	0.006	749	int	5
2p3b	1.991	0.008	1.598	0.026	0.344	0.000	0.003	0.007	798	int	5
2p4	1.990	0.008	1.604	0.020	0.348	0.000	0.004	0.003	738	rim	5
2p4	1.991	0.008	1.604	0.018	0.349	0.000	0.003	0.005	717	rim	7

2p5	1.992	0.008	1.600	0.024	0.342	0.000	0.004	0.005	780	rim	3
2p5	1.993	0.007	1.599	0.023	0.348	0.000	0.002	0.005	768	int	4
2p6	1.983	0.010	1.582	0.026	0.376	0.000	0.003	0.006	785	rim	6
2p8	1.993	0.008	1.603	0.022	0.344	0.000	0.003	0.005	759	rim	6
2p9	1.993	0.007	1.607	0.019	0.346	0.000	0.003	0.004	729	int	5
2p10	1.991	0.008	1.612	0.020	0.342	0.000	0.002	0.004	740	int	6
2p11	1.990	0.010	1.601	0.026	0.346	0.000	0.004	0.005	797	rim	8
2p13	1.995	0.008	1.601	0.024	0.343	0.000	0.002	0.005	779	rim	4

Estacado (H6)

pair #	Si	Al	Mg	Ca	Fe	Na	Cr	Ti	Tc (Celsius)	spot position	dist to nearest edge (µm)
2p2	1.996	0.009	1.596	0.023	0.348	0.000	0.003	0.003	768	int	8
2p1	1.988	0.014	1.590	0.030	0.344	0.000	0.005	0.008	836	rim	19
2p10	1.989	0.010	1.588	0.030	0.359	0.000	0.004	0.004	830	rim	8
2p3	1.990	0.006	1.602	0.026	0.351	0.000	0.003	0.004	795	int	15
2p5	2.000	0.007	1.591	0.029	0.342	0.000	0.003	0.003	828	rim	8
2p6	1.993	0.010	1.590	0.026	0.349	0.000	0.004	0.006	797	int	9
2p8	1.996	0.008	1.602	0.026	0.343	0.000	0.000	0.004	798	core	36
2p7	1.997	0.005	1.600	0.022	0.347	0.000	0.002	0.006	758	rim	12
2p9	1.988	0.007	1.602	0.027	0.345	0.000	0.006	0.005	807	int	9
2p11	1.990	0.009	1.599	0.026	0.341	0.000	0.005	0.005	800	int	36
2p13	1.985	0.008	1.596	0.027	0.353	0.000	0.005	0.006	804	rim	26
2p14	1.995	0.010	1.600	0.021	0.348	0.000	0.000	0.006	748	int	16
2p12	2.003	0.006	1.590	0.027	0.341	0.000	0.002	0.003	810	rim	11
2p16	1.996	0.007	1.600	0.021	0.343	0.000	0.005	0.006	750	rim	16
2p15	1.993	0.009	1.599	0.024	0.340	0.000	0.002	0.007	781	int	13
2p17	1.994	0.006	1.597	0.019	0.351	0.000	0.003	0.004	727	rim	12

2p18	1.997	0.006	1.599	0.024	0.342	0.000	0.003	0.005	780	int	13
2p19	1.987	0.006	1.608	0.022	0.352	0.000	0.002	0.007	756	core	34
2p23	1.991	0.009	1.600	0.023	0.352	0.000	0.004	0.004	766	core	10
2p24	1.987	0.010	1.596	0.026	0.358	0.000	0.004	0.005	792	core	13
2p20	1.994	0.008	1.595	0.027	0.344	0.000	0.004	0.005	808	rim	11
2p22	1.993	0.008	1.600	0.027	0.341	0.000	0.005	0.006	809	rim	7
2p21	1.996	0.008	1.600	0.026	0.342	0.000	0.002	0.005	799	int	13
2p25	1.992	0.009	1.601	0.028	0.344	0.000	0.002	0.005	817	int	17
2p26	1.989	0.006	1.582	0.018	0.369	0.000	0.000	0.005	710	rim	8
2p27	1.990	0.010	1.598	0.025	0.347	0.000	0.004	0.007	787	int	8
2p29	1.991	0.007	1.604	0.017	0.358	0.000	0.004	0.004	704	rim	10
2p28	1.986	0.017	1.556	0.024	0.392	0.000	0.004	0.004	760	core	6
2p30	1.993	0.008	1.599	0.024	0.350	0.000	0.003	0.005	776	rim	8
2p31	1.994	0.005	1.605	0.021	0.346	0.000	0.004	0.004	749	rim	18
2p33	1.988	0.007	1.602	0.024	0.343	0.000	0.003	0.006	779	int	7
2p34	1.989	0.008	1.603	0.029	0.342	0.000	0.003	0.005	827	int	12

Holbrook (L6)

pair #	Si	Al	Mg	Ca	Fe	Na	Cr	Ti	Tc (Celsius)	spot position	dist to nearest edge (µm)
2p3	1.973	0.018	1.493	0.035	0.443	0.000	0.010	0.012	841	rim	5
2p5	1.996	0.004	1.498	0.029	0.440	0.000	0.004	0.005	788	int	12
2p9	1.992	0.009	1.497	0.028	0.447	0.000	0.003	0.006	775	rim	13
2p11	1.991	0.011	1.497	0.041	0.435	0.000	0.005	0.003	896	int	5
2p12	1.986	0.006	1.509	0.032	0.446	0.000	0.003	0.008	812	rim	8
2p16	1.998	0.000	1.507	0.033	0.447	0.000	0.000	0.000	820	rim	19
2p17	1.988	0.005	1.494	0.036	0.454	0.003	0.004	0.006	844	rim	9
2p14	1.998	0.003	1.506	0.031	0.433	0.000	0.000	0.004	809	int	8

2p21	2.004	0.000	1.494	0.034	0.441	0.000	0.000	0.004	833	int	10
2p22	1.993	0.006	1.501	0.026	0.450	0.000	0.007	0.000	754	int	6
2p24	1.995	0.004	1.501	0.034	0.431	0.000	0.007	0.006	838	int	7
2p25	2.001	0.003	1.489	0.033	0.450	0.000	0.004	0.000	820	int	9
2p27	2.001	0.003	1.503	0.032	0.439	0.000	0.000	0.006	815	int	7
2p26	1.994	0.003	1.488	0.038	0.446	0.000	0.005	0.004	866	int	8
2p31	1.993	0.005	1.487	0.034	0.447	0.000	0.008	0.004	830	rim	12
2p32	2.008	0.000	1.509	0.032	0.431	0.000	0.000	0.000	819	rim	5
2p37	2.000	0.003	1.501	0.034	0.450	0.000	0.000	0.000	828	rim	18
2p35	1.997	0.005	1.504	0.031	0.438	0.000	0.005	0.003	807	int	15
2p38	1.994	0.000	1.502	0.035	0.446	0.000	0.004	0.003	839	int	9
2p36	1.997	0.003	1.493	0.031	0.451	0.000	0.003	0.000	801	int	8

Kernouve (H6)

pair #	Si	Al	Mg	Ca	Fe	Na	Cr	Ti	Tc (Celsius)	spot position	dist to nearest edge (μm)
2p2	1.994	0.008	1.602	0.026	0.340	0.000	0.003	0.004	800	rim	11
2p3	1.994	0.010	1.598	0.025	0.343	0.000	0.002	0.004	789	rim	12
2p4	1.990	0.008	1.598	0.022	0.349	0.000	0.001	0.005	758	core	8
2p5	1.994	0.009	1.592	0.029	0.345	0.000	0.004	0.005	827	core	13
2p7	1.993	0.008	1.595	0.027	0.346	0.000	0.004	0.005	807	int	7
2p8	1.992	0.008	1.601	0.023	0.347	0.000	0.002	0.005	768	int	8
2p13	1.992	0.006	1.601	0.028	0.347	0.000	0.002	0.004	816	rim	10
2p14	1.988	0.007	1.605	0.020	0.356	0.000	0.003	0.005	735	rim	11
2p15	1.993	0.008	1.601	0.023	0.343	0.000	0.002	0.006	770	core	10
2p16	1.992	0.005	1.600	0.031	0.346	0.000	0.003	0.005	844	rim	7
2p19	1.989	0.008	1.607	0.024	0.344	0.000	0.003	0.005	779	rim	10

2p20	1.994	0.007	1.595	0.030	0.344	0.000	0.004	0.005	836	int	6
2p22	1.988	0.009	1.602	0.025	0.349	0.000	0.003	0.005	786	rim	12

Leedey (L6)

pair #	Si	Al	Mg	Ca	Fe	Na	Cr	Ti	Tc (Celsius)	spot position	dist to nearest edge (µm)
2p8	2.000	0.007	1.523	0.024	0.420	0.000	0.005	0.000	749	int	18
2p9	1.991	0.009	1.510	0.029	0.426	0.000	0.002	0.008	794	int	8
2p10	1.994	0.006	1.525	0.024	0.425	0.000	0.003	0.005	746	rim	10
2p13	2.003	0.007	1.514	0.029	0.420	0.000	0.003	0.000	797	core	11
2p20	2.002	0.008	1.502	0.032	0.422	0.000	0.003	0.005	824	int	8
2p21	1.993	0.008	1.518	0.023	0.428	0.000	0.003	0.005	735	int	12
2p22	1.995	0.007	1.508	0.029	0.420	0.000	0.002	0.007	797	int	14
2p25	1.996	0.009	1.512	0.025	0.426	0.000	0.003	0.006	756	rim	5

Morrow County (L6)

pair #	Si	Al	Mg	Ca	Fe	Na	Cr	Ti	Tc (Celsius)	spot position	dist to nearest edge (µm)
2p7	1.995	0.007	1.513	0.028	0.428	0.000	0.002	0.005	783	rim	7
2p6a	1.989	0.006	1.525	0.022	0.432	0.000	0.003	0.005	724	rim	3
2p6b	1.988	0.010	1.506	0.026	0.446	0.000	0.005	0.005	756	rim	4
2p5	1.996	0.004	1.517	0.023	0.432	0.000	0.003	0.005	734	rim	4
2p8	1.996	0.007	1.515	0.028	0.419	0.000	0.003	0.006	788	rim	11
2p9	1.991	0.007	1.512	0.026	0.434	0.000	0.003	0.005	762	int	14
2p9	1.967	0.007	1.499	0.026	0.493	0.000	0.004	0.006	735	int	17
2p11	1.991	0.007	1.512	0.025	0.430	0.000	0.004	0.006	754	int	10
2p11	1.992	0.007	1.514	0.024	0.428	0.000	0.004	0.005	745	int	9
2p13	1.992	0.007	1.528	0.022	0.423	0.000	0.003	0.006	728	rim	14

2p13	1.995	0.007	1.524	0.022	0.424	0.000	0.000	0.007	727	int	21
2p12	1.999	0.007	1.518	0.025	0.417	0.000	0.005	0.006	760	int	16
2p12	1.991	0.009	1.514	0.021	0.441	0.000	0.002	0.005	710	rim	6
2p10	1.996	0.008	1.528	0.022	0.416	0.000	0.002	0.004	731	rim	20
2p10	1.997	0.005	1.523	0.023	0.430	0.000	0.000	0.004	734	core	45
2p17	1.996	0.007	1.524	0.025	0.422	0.000	0.000	0.005	757	int	4
2p15	1.967	0.010	1.507	0.031	0.477	0.000	0.004	0.007	788	int	23
2p16	1.994	0.004	1.521	0.032	0.424	0.000	0.003	0.004	822	rim	18
2p14	2.000	0.007	1.508	0.029	0.422	0.000	0.004	0.005	796	rim	11
2p20	1.991	0.007	1.530	0.026	0.420	0.000	0.005	0.005	768	int	28
2p21	1.997	0.007	1.516	0.027	0.427	0.000	0.003	0.005	774	rim	8
2p19	1.994	0.007	1.514	0.026	0.431	0.000	0.003	0.005	763	int	8
2p19	2.000	0.005	1.516	0.028	0.423	0.003	0.002	0.002	786	core	14
2p19	1.966	0.011	1.485	0.028	0.490	0.000	0.002	0.005	755	int	8
2p22	1.995	0.007	1.515	0.022	0.427	0.000	0.005	0.006	726	int	16

Park (L6)

pair #	Si	Al	Mg	Ca	Fe	Na	Cr	Ti	Tc (Celsius)	spot position	dist to nearest edge (µm)
2p1	1.989	0.007	1.509	0.032	0.437	0.000	0.003	0.005	816	rim	9
2p6	1.993	0.008	1.517	0.023	0.430	0.000	0.003	0.005	734	rim	7
2p7	1.986	0.008	1.513	0.029	0.440	0.000	0.003	0.006	787	rim	6
2p10	1.991	0.007	1.513	0.024	0.439	0.000	0.002	0.006	740	int	24
2p14	1.988	0.009	1.500	0.039	0.435	0.000	0.004	0.006	879	rim	8
2p18	1.993	0.008	1.510	0.025	0.432	0.000	0.003	0.005	753	rim	6

Portales Valley (H6)

pair #	Si	Al	Mg	Ca	Fe	Na	Cr	Ti	Tc (Celsius)	spot position	dist to nearest edge (µm)
2p1	1.988	0.009	1.596	0.025	0.350	0.000	0.006	0.006	786	rim	12
2p1	1.996	0.007	1.597	0.019	0.344	0.000	0.004	0.005	730	core	24
2p6	1.995	0.009	1.584	0.038	0.336	0.000	0.005	0.006	912	rim	13
2p4	1.994	0.007	1.601	0.021	0.345	0.000	0.004	0.004	749	int	21
2p7	1.996	0.009	1.590	0.030	0.342	0.000	0.003	0.005	837	rim	10
2p8	1.990	0.008	1.591	0.035	0.352	0.000	0.005	0.004	878	int	33
2p5	1.995	0.009	1.602	0.026	0.339	0.000	0.004	0.006	800	int	29
2p2	1.989	0.007	1.600	0.029	0.341	0.000	0.004	0.007	828	rim	26
2p9	1.988	0.012	1.586	0.032	0.349	0.000	0.006	0.008	853	rim	7
2p11	1.995	0.009	1.582	0.034	0.346	0.000	0.005	0.005	872	rim	20
2p12	1.992	0.009	1.580	0.042	0.343	0.000	0.005	0.005	943	int	17
2p13	1.991	0.012	1.582	0.033	0.353	0.000	0.004	0.007	860	int	21
2p14	1.995	0.007	1.582	0.042	0.345	0.000	0.004	0.005	942	int	29
2p17	1.988	0.010	1.592	0.026	0.350	0.000	0.008	0.004	796	rim	13
2p15	1.987	0.009	1.588	0.033	0.349	0.003	0.005	0.006	862	int	22
2p19	1.996	0.010	1.593	0.033	0.336	0.000	0.005	0.005	867	rim	15
2p20	1.997	0.008	1.586	0.034	0.345	0.000	0.003	0.005	872	rim	10
2p22	1.991	0.010	1.580	0.039	0.346	0.000	0.005	0.006	916	int	28
2p25	1.992	0.010	1.586	0.034	0.344	0.000	0.006	0.005	873	int	16

Queen's Mercy (H6)

pair #	Si	Al	Mg	Ca	Fe	Na	Cr	Ti	Tc (Celsius)	spot position	dist to nearest edge (µm)
2p1	1.994	0.008	1.613	0.023	0.330	0.002	0.003	0.005	774	int	2
2p2	1.995	0.007	1.604	0.024	0.335	0.000	0.003	0.005	783	rim	8
2p5	1.991	0.008	1.612	0.024	0.341	0.000	0.001	0.004	780	int	5
2p6	1.990	0.006	1.615	0.025	0.334	0.000	0.002	0.004	792	rim	5
2p8	2.001	0.008	1.604	0.026	0.327	0.000	0.003	0.004	805	int	17
2p8	2.003	0.008	1.601	0.022	0.327	0.000	0.003	0.006	766	int	15
2p9	1.992	0.014	1.603	0.028	0.327	0.000	0.004	0.008	824	int	6
2p9	1.994	0.010	1.613	0.028	0.322	0.000	0.004	0.006	826	int	3
2p10	1.997	0.009	1.619	0.018	0.328	0.000	0.003	0.005	725	core	11
2p10	1.997	0.007	1.614	0.023	0.329	0.000	0.004	0.003	775	int	6
2p11	1.987	0.013	1.604	0.025	0.339	0.000	0.004	0.007	791	rim	2
2p11	1.987	0.013	1.610	0.021	0.338	0.002	0.002	0.006	752	int	3
2p11	1.987	0.014	1.591	0.027	0.339	0.000	0.007	0.009	810	rim	1
2p12	1.992	0.009	1.607	0.021	0.341	0.000	0.002	0.005	751	rim	4
2p12	1.994	0.008	1.608	0.027	0.336	0.000	0.002	0.003	811	int	12
2p13	1.990	0.009	1.612	0.022	0.338	0.000	0.003	0.005	761	rim	3
2p13	1.989	0.009	1.608	0.021	0.338	0.000	0.004	0.007	752	core	4
2p14	1.993	0.008	1.615	0.026	0.328	0.000	0.003	0.004	804	rim	3
2p15	1.991	0.010	1.611	0.025	0.332	0.000	0.004	0.005	793	int	7

APPENDIX C: Olivine data

This appendix contains compositional data measured from olivine grains for each sample. Closure temperatures calculated according to the Wlotzka (2005) method are presented also, as well as the position of the spot datum within the grain and the distance to the nearest edge of the grain in microns from the spot datum. Fayalite percent is defined as $\frac{Fe}{Fe+Mg}$ in olivine where the concentrations of Fe and Mg are in normalized atom percent.

Bruderheim (L6)

pair	Fayalite %	Tc (Celsius)	spot position	dist to nearest edge (µm)
co4	24.0	678	rim	7
co5	25.4	670	rim	16
co7	24.5	701	rim	5
co9	26.6	704	int	16
co10	24.1	693	rim	13
co11	25.6	713	rim	24

Butsura (L6)

pair	Fayalite %	Tc (Celsius)	spot position	dist to nearest edge (µm)
co1	19.8	679	rim	5
co1	19.4	675	rim	8
co2	19.8	693	core	24
co2	19.7	691	rim	6
co3	20.0	684	rim	13
co3	20.0	684	rim	50
co4	19.7	658	core	14
co6	20.1	650	rim	8
co8	19.4	652	rim	15
co10	19.8	695	int	19
co11	20.1	687	int	32
co12	19.8	668	int	23

Estacado (H6)

pair	Fayalite %	Tc (Celsius)	spot position	dist to nearest edge (µm)
co2	20.0	703	int	13
co3	19.8	683	core	30
co6	20.1	657	rim	13
co5	20.1	644	int	15
co4	19.4	687	int	20
co7	19.1	694	int	31

co8	19.5	693	int	7
co9	20.2	680	int	23
co10	19.1	700	rim	26
co11	20.1	700	rim	31
co12	19.9	731	int	44
co13	21.9	725	rim	33
co14	19.4	667	rim	24
co15	17.7	674	int	6
co16	19.4	708	rim	11
co18	19.3	699	rim	34
co19	18.9	702	rim	12
co23	20.2	687	int	28
co22	19.3	693	rim	30
co20	19.7	675	rim	24
co21	18.6	695	rim	10

Holbrook (L6)

pair	Fayalite %	Tc (Celsius)	spot position	dist to nearest edge (µm)
co1	27.3	757	int	12
co3	26.7	719	int	8
co4	27.2	703	int	6
co7	26.9	729	core	11
co12	26.9	708	int	12
co13	26.7	729	int	9
co16	27.3	718	int	7
co23	27.4	692	rim	8
co22	27.0	708	int	10
co20	27.4	693	core	12
co21	26.7	683	rim	7
co26	26.7	684	rim	5
co27	26.6	697	int	9

Kernouve (H6)

pair	Fayalite %	Tc (Celsius)	spot position	dist to nearest edge (µm)
co4	19.4	706	rim	29
co6	19.7	713	int	50
co7	18.5	702	rim	21
co9	19.9	694	int	17
co9	19.3	688	int	17
co9a	19.2	657	rim	17

co10	19.7	680	int	24
co11	19.4	680	rim	10
co11	19.7	683	int	35
co12	19.1	689	rim	8
co12	19.3	692	int	24
co13	19.0	713	rim	21
co14	19.7	702	core	54
co14	19.5	699	rim	9
co15	19.3	685	rim	23
co16	19.2	701	rim	14

Leedey (L6)

pair	Fayalite %	Tc (Celsius)	spot position	dist to nearest edge (µm)
co1	24.6	694	rim	12
co2	25.5	680	rim	22
co3	23.3	682	rim	13
co4	25.0	712	rim	9
co5	25.4	708	rim	21
co6	25.3	695	rim	15
co22	25.3	707	rim	7

Morrow County (L6)

pair	Fayalite %	Tc (Celsius)	spot position	dist to nearest edge (µm)
co2	25.6	709	rim	12
co2	25.6	709	int	23
co6	25.0	700	core	58
co6	24.6	696	core	56
co8	24.5	689	core	44
co8	24.4	688	rim	18
co7	25.3	684	int	13
co7	25.3	684	core	19
co9	24.5	682	rim	12
co10	25.5	707	int	48
co11	25.1	711	rim	20
co14	24.3	702	core	17
co15	24.7	717	avg	27
co15	24.8	718	int	17
co15	24.6	715	rim	54
co12	25.1	709	int	49
co16	26.1	705	int	41

co17	25.5	701	rim	13
co18	25.7	708	int	71

Portales Valley (H6)

pair	Fayalite %	Tc (Celsius)	spot position	dist to nearest edge (µm)
co5	19.5	686	core	42
co1	18.6	694	rim	15
co4	19.4	681	rim	19
co6	20.2	702	rim	16
co6	19.7	696	rim	8
co9	19.7	703	rim	29
co15	19.3	688	rim	15
co13	19.8	707	rim	25
co16	19.8	694	rim	31
co17	20.4	696	int	31

Queen's Mercy (H6)

pair	Fayalite %	Tc (Celsius)	spot position	dist to nearest edge (µm)
co1	18.3	658	int	6
co1	18.3	658	int	5
co2	19.8	668	rim	3
co5	18.5	678	rim	11
co5	18.1	673	int	10
co6	19.1	669	int	29
co7	18.9	690	int	3
co7	19.1	694	int	3
co8	17.7	664	rim	3
co8	17.5	662	rim	3
co8	18.1	668	int	2
co9	18.7	673	rim	8
co9	18.9	675	rim	11
co10	18.6	654	core	18
co10	19.4	663	int	13
co11	19.5	654	rim	7
co12	18.4	680	rim	7
co12	18.1	677	rim	4
co12	19.2	689	core	45
co13	18.8	683	rim	13
co13	19.0	684	core	52
co13	18.8	682	core	83

APPENDIX D: Chromite data

This appendix contains compositional data measured from chromite grains for each sample. Closure temperatures calculated according to the Wlotzka (2005) method are presented also, as well as the position of the spot datum within the grain and the distance to the nearest edge of the grain in microns from the spot datum. All concentrations are given as stoichiometrically normalized to 4 oxygens. Si is close to the SEM's detection limit for most measurements for chromite.

Bruderheim (L6)

pair	Si	Ti	Al	Cr	Fe^{2+}	Mn	Mg	Tc (Celsius)	spot position	dist to nearest edge (μm)
co4	0.002	0.071	0.244	1.586	0.922	0.013	0.114	678	rim	10
co5	0.009	0.059	0.247	1.590	0.933	0.013	0.102	670	rim	6
co7	0.017	0.057	0.249	1.582	0.909	0.014	0.125	701	core	10
co9	0.006	0.073	0.243	1.570	0.938	0.013	0.117	704	rim	2
co10	0.005	0.074	0.240	1.574	0.928	0.014	0.124	693	int	11
co11	0.003	0.080	0.232	1.574	0.921	0.014	0.125	713	rim	10

Butsura (H6)

pair	Si	Ti	Al	Cr	Fe^{2+}	Mn	Mg	Tc (Celsius)	spot position	dist to nearest edge (μm)
co1	0.004	0.052	0.283	1.584	0.875	0.019	0.137	666	rim	4
co1	0.003	0.060	0.269	1.591	0.857	0.018	0.150	688	int	21
co2	0.003	0.062	0.263	1.593	0.858	0.018	0.156	699	int	19
co2	0.004	0.056	0.275	1.581	0.870	0.018	0.149	685	rim	2
co3	0.003	0.058	0.274	1.584	0.869	0.022	0.142	679	rim	14
co3	0.003	0.062	0.262	1.598	0.861	0.019	0.147	689	core	41
co4	0.003	0.055	0.276	1.579	0.892	0.020	0.131	658	core	6
co6	0.003	0.028	0.275	1.633	0.882	0.017	0.119	650	core	6
co8	0.003	0.055	0.280	1.579	0.888	0.019	0.129	652	core	10
co10	0.003	0.061	0.263	1.592	0.858	0.021	0.152	695	rim	12
co11	0.005	0.061	0.265	1.589	0.864	0.022	0.145	687	int	21
co12	0.005	0.053	0.268	1.600	0.873	0.016	0.133	668	int	17

Estacado (H6)

pair	Si	Ti	Al	Cr	Fe^{2+}	Mn	Mg	Tc (Celsius)	spot position	dist to nearest edge (μm)
co2	0.006	0.060	0.264	1.576	0.863	0.028	0.159	703	int	8
co3	0.000	0.057	0.277	1.583	0.857	0.027	0.145	683	int	15
co6	0.005	0.041	0.289	1.598	0.878	0.020	0.127	657	int	5
co5	0.002	0.038	0.302	1.579	0.887	0.029	0.121	644	core	6
co4	0.000	0.048	0.284	1.601	0.840	0.024	0.151	687	int	12
co7	0.000	0.058	0.261	1.598	0.854	0.024	0.158	694	int	9
co8	0.004	0.061	0.267	1.588	0.860	0.022	0.154	693	core	13
co9	0.002	0.057	0.277	1.597	0.862	0.018	0.140	680	core	20
co10	0.005	0.057	0.267	1.588	0.847	0.027	0.164	700	int	17
co11	0.003	0.055	0.263	1.599	0.855	0.023	0.153	700	rim	9

co12	0.005	0.056	0.264	1.591	0.835	0.022	0.180	731	rim	10
co13	0.000	0.059	0.270	1.593	0.845	0.024	0.158	725	int	17
co14	0.004	0.038	0.296	1.596	0.855	0.029	0.138	667	core	8
co15	0.002	0.059	0.267	1.592	0.856	0.022	0.156	674	int	23
co16	0.000	0.056	0.272	1.594	0.841	0.025	0.167	708	core	16
co18	0.003	0.058	0.275	1.594	0.839	0.025	0.159	699	int	17
co19	0.003	0.059	0.259	1.602	0.847	0.017	0.165	702	int	16
co23	0.003	0.059	0.265	1.589	0.866	0.024	0.144	687	int	9
co22	0.003	0.053	0.276	1.595	0.839	0.025	0.155	693	int	27
co20	0.000	0.054	0.268	1.603	0.875	0.015	0.140	675	int	9
co21	0.004	0.054	0.272	1.585	0.837	0.032	0.164	695	rim	7

Holbrook (L6)

pair	Si	Ti	Al	Cr	Fe^{2+}	Mn	Mg	Tc (Celsius)	spot position	dist to nearest edge (μm)
co1	0.011	0.098	0.217	1.581	0.916	0.022	0.141	757	int	15
co3	0.006	0.093	0.230	1.578	0.944	0.022	0.125	719	int	7
co4	0.003	0.099	0.212	1.589	0.962	0.024	0.111	703	int	12
co7	0.000	0.101	0.215	1.585	0.945	0.022	0.128	729	rim	11
co12	0.000	0.091	0.237	1.574	0.960	0.021	0.120	708	int	7
co13	0.004	0.093	0.216	1.590	0.940	0.023	0.129	729	rim	11
co16	0.008	0.080	0.236	1.589	0.942	0.020	0.121	718	int	8
co23	0.000	0.088	0.234	1.592	0.965	0.013	0.106	692	int	8
co22	0.003	0.093	0.228	1.580	0.964	0.011	0.118	708	rim	4
co20	0.003	0.091	0.236	1.578	0.958	0.022	0.106	693	int	6
co21	0.000	0.096	0.206	1.589	0.977	0.025	0.102	683	int	7
co26	0.003	0.090	0.236	1.582	0.959	0.024	0.105	684	int	8
co27	0.000	0.092	0.235	1.573	0.972	0.017	0.115	697	int	6

Kernouve (H6)

pair	Si	Ti	Al	Cr	Fe^{2+}	Mn	Mg	Tc (Celsius)	spot position	dist to nearest edge (µm)
co4	0.002	0.058	0.261	1.608	0.842	0.017	0.159	702	rim	11
co4	0.003	0.062	0.250	1.610	0.846	0.018	0.163	709	rim	46
co6	0.002	0.059	0.254	1.604	0.853	0.016	0.166	713	int	11
co7	0.001	0.062	0.252	1.607	0.846	0.017	0.166	700	rim	9
co7	0.004	0.062	0.251	1.610	0.839	0.014	0.168	703	int	37
co9	0.003	0.051	0.277	1.596	0.870	0.000	0.152	686	rim	12
co9	0.004	0.056	0.261	1.612	0.854	0.000	0.154	696	rim	11
co9a	0.003	0.040	0.293	1.595	0.862	0.021	0.133	657	int	10
co10	0.003	0.050	0.279	1.593	0.864	0.017	0.145	680	int	15
co11	0.002	0.050	0.280	1.589	0.872	0.017	0.145	677	rim	3
co11	0.001	0.054	0.269	1.605	0.854	0.017	0.147	686	int	20
co12	0.002	0.056	0.262	1.607	0.852	0.018	0.153	690	int	19
co13	0.002	0.061	0.251	1.611	0.837	0.017	0.170	713	int	34
co14	0.004	0.060	0.254	1.611	0.853	0.013	0.156	701	int	20
co15	0.002	0.050	0.272	1.599	0.853	0.022	0.150	685	int	11
co16	0.003	0.059	0.255	1.602	0.849	0.017	0.161	701	rim	9

Leedey (L6)

pair	Si	Ti	Al	Cr	Fe^{2+}	Mn	Mg	Tc (Celsius)	spot position	dist to nearest edge (μm)
co1	0.003	0.080	0.239	1.579	0.927	0.000	0.121	694	int	20
co2	0.003	0.079	0.234	1.582	0.947	0.000	0.107	680	int	10
co3	0.005	0.082	0.232	1.585	0.925	0.000	0.119	682	rim	6
co4	0.020	0.084	0.234	1.554	0.903	0.025	0.127	712	rim	12
co5	0.008	0.077	0.241	1.575	0.905	0.016	0.123	708	rim	10
co6	0.004	0.080	0.238	1.571	0.918	0.024	0.115	695	rim	16
co22	0.001	0.080	0.246	1.572	0.910	0.015	0.124	707	int	16

Morrow County (L6)

pair	Si	Ti	Al	Cr	Fe^{2+}	Mn	Mg	Tc (Celsius)	spot position	dist to nearest edge (μm)
co2	0.003	0.079	0.235	1.577	0.914	0.024	0.124	711	rim	8
co2	0.005	0.078	0.237	1.574	0.921	0.021	0.122	707	rim	8
co6	0.002	0.063	0.254	1.599	0.896	0.013	0.118	696	rim	10
co6	0.005	0.073	0.245	1.580	0.908	0.020	0.122	700	int	25
co8	0.002	0.056	0.259	1.595	0.904	0.018	0.115	685	rim	12
co8	0.002	0.068	0.249	1.582	0.913	0.018	0.119	691	rim	16
co7	0.003	0.068	0.256	1.565	0.934	0.020	0.114	685	rim	6
co7	0.005	0.068	0.252	1.557	0.940	0.021	0.113	683	rim	4
co9	0.002	0.064	0.250	1.587	0.923	0.024	0.114	682	rim	6
co10	0.005	0.063	0.250	1.584	0.917	0.019	0.124	707	int	14
co11	0.003	0.084	0.230	1.579	0.915	0.022	0.126	711	rim	20
co14	0.003	0.070	0.247	1.589	0.902	0.016	0.126	702	rim	8
co15	0.003	0.076	0.242	1.574	0.900	0.021	0.133	717	int	23
co13	0.002	0.074	0.243	1.582	0.908	0.018	0.124	716	int	17
co12	0.006	0.080	0.233	1.572	0.917	0.020	0.125	709	rim	16

co16	0.003	0.071	0.253	1.573	0.914	0.020	0.119	705	int	18
co17	0.005	0.068	0.244	1.580	0.919	0.016	0.119	701	rim	5
co18	0.006	0.077	0.244	1.569	0.908	0.024	0.121	708	int	16

Park (L6)

pair	Si	Ti	Al	Cr	Fe^{2+}	Mn	Mg	Tc (Celsius)	spot position	dist to nearest edge (µm)
co1	0.003	0.077	0.242	1.577	0.902	0.010	0.142	743	int	9
co4	0.003	0.074	0.245	1.578	0.903	0.016	0.134	728	int	15
co5	0.003	0.082	0.233	1.575	0.885	0.013	0.161	774	rim	10
co5	0.003	0.084	0.229	1.582	0.875	0.012	0.164	782	int	22
co6	0.003	0.072	0.243	1.577	0.904	0.014	0.140	731	rim	6
co6	0.003	0.078	0.241	1.575	0.890	0.015	0.147	744	int	17
co8	0.003	0.074	0.245	1.581	0.897	0.014	0.132	710	int	13
co9	0.003	0.080	0.237	1.576	0.893	0.012	0.153	763	rim	8
co10	0.003	0.084	0.231	1.579	0.893	0.013	0.146	742	int	13
co16	0.002	0.082	0.232	1.584	0.887	0.010	0.154	765	rim	12
co15	0.003	0.080	0.233	1.578	0.902	0.013	0.142	748	rim	11
co14	0.003	0.077	0.238	1.579	0.893	0.014	0.150	759	core	21
co17	0.004	0.077	0.242	1.581	0.888	0.013	0.143	745	int	18

Portales Valley (H6)

pair	Si	Ti	Al	Cr	Fe^{2+}	Mn	Mg	Tc (Celsius)	spot position	dist to nearest edge (μm)
co5	0.009	0.054	0.267	1.600	0.848	0.024	0.147	686	int	13
co1	0.000	0.048	0.270	1.614	0.837	0.020	0.162	694	int	13
co4	0.000	0.052	0.273	1.594	0.863	0.024	0.148	681	int	11
co6	0.003	0.056	0.275	1.601	0.847	0.018	0.155	699	int	14
co9	0.004	0.052	0.270	1.593	0.849	0.022	0.160	703	int	15
co15	0.003	0.054	0.270	1.599	0.853	0.019	0.152	688	int	11
co13	0.003	0.057	0.267	1.599	0.842	0.022	0.161	707	core	38
co16	0.003	0.053	0.270	1.608	0.847	0.024	0.151	694	int	23
co17	0.005	0.051	0.267	1.605	0.854	0.020	0.148	696	int	28

Queen's Mercy (H6)

pair	Si	Ti	Al	Cr	Fe^{2+}	Mn	Mg	Tc (Celsius)	spot position	dist to nearest edge (μm)
co1	0.005	0.053	0.283	1.573	0.880	0.020	0.143	656	rim	3
co1	0.004	0.054	0.279	1.574	0.879	0.019	0.144	659	rim	2
co2	0.003	0.041	0.303	1.582	0.862	0.021	0.139	668	rim	4
co5	0.005	0.057	0.270	1.584	0.864	0.020	0.152	674	rim	4
co5	0.003	0.060	0.267	1.591	0.857	0.019	0.153	677	int	19
co6	0.003	0.043	0.302	1.573	0.862	0.022	0.146	669	int	6
co7	0.005	0.049	0.299	1.557	0.863	0.018	0.167	691	int	2
co7	0.008	0.049	0.303	1.552	0.859	0.014	0.169	693	int	2
co8	0.003	0.057	0.274	1.577	0.867	0.021	0.152	666	rim	9
co8	0.003	0.057	0.278	1.579	0.865	0.019	0.150	664	rim	8
co9	0.002	0.058	0.270	1.589	0.866	0.020	0.145	672	int	21
co9	0.002	0.057	0.271	1.588	0.865	0.019	0.149	676	int	21
co10	0.004	0.031	0.293	1.583	0.893	0.018	0.135	651	rim	3
co10	0.003	0.043	0.287	1.583	0.875	0.019	0.143	665	int	5
co11	0.002	0.029	0.303	1.594	0.875	0.020	0.131	654	int	4
co12	0.003	0.058	0.278	1.582	0.854	0.019	0.158	685	int	29
co12	0.003	0.055	0.279	1.574	0.868	0.017	0.157	680	rim	4
co13	0.003	0.057	0.279	1.580	0.856	0.018	0.156	685	core	21
co13	0.003	0.056	0.282	1.576	0.857	0.019	0.157	685	int	10
co13	0.003	0.048	0.286	1.585	0.857	0.020	0.153	679	rim	5

APPENDIX E: Metallographic data

This appendix contains compositional and grain size data from linescans gathered from zoned taenite grains for each sample, as well as associated errors. Closure temperatures from rims and cores are found using the P-free sub-solidus Fe-Ni phase diagram of Reisener and Goldstein (2003a).

Bruderheim (L6)

linescan #	grain radius (μm)	grain radius error (μm)	core Ni wt%	core Ni wt% error	rim Tc (Celsius)	core Tc (Celsius)
ls 2	46.0	3.0	29.0	0.5	113	527
ls 5b1	14.5	0.5	31.5	0.6	343	508
ls 5b2	8.5	1.5	31.8	0.5	381	506
ls 9	19.5	1.5	32.7	0.6	393	499
ls 10	59.5	3.5	29.8	0.5	402	521
ls 11	28.0	2.0	20.7	1.2	113	589
ls 12a	38.5	2.5	32.7	0.5	381	507
ls 12b	35.5	2.5	31.6	0.6	391	506

Butsura (H6)

linescan #	grain radius (μm)	grain radius error (μm)	core Ni wt%	core Ni wt% error	rim Tc (Celsius)	core Tc (Celsius)
ls 2	19.0	3.0	31.9	0.7	352	505
ls 5	37.5	2.5	34.1	0.4	306	486
ls 6	37.5	1.5	33.2	0.6	373	494
ls 7	48.5	2.5	25.2	0.3	409	556
ls 15	17.0	3.0	32.0	0.5	405	504
ls 18	25.0	3.0	31.4	0.6	410	509
ls 21	11.0	3.0	42.5	0.2	286	408
ls 22	35.0	3.0	30.1	0.7	402	519
ls 23	39.5	2.5	27.2	0.9	408	541
ls 24	35.0	3.0	29.1	0.5	408	527
ls 28	31.5	3.5	30.6	0.5	409	516
ls 33	23.0	2.0	31.1	0.8	113	512
ls 34	21.0	4.0	31.2	0.5	407	511
ls 35	21.0	2.0	36.6	0.7	113	462
ls 45	26.0	4.0	35.0	0.4	155	477
ls 46	18.0	3.0	36.2	1.1	113	466
ls 48	21.0	2.0	33.1	0.5	409	495

Estacado (H6)

linescan #	grain radius (μm)	grain radius error (μm)	core Ni wt%	core Ni wt% error	rim Tc (Celsius)	core Tc (Celsius)
ls 1a	29.0	2.0	32.7	0.7	383	499
ls 1b	18.0	1.0	37.7	0.5	283	448
ls 2d	5.5	1.5	41.4	0.4	375	409
ls 3	26.5	1.5	34.6	0.6	351	481
ls 4a1	12.0	2.0	38.3	0.5	377	441
ls 4a2	18.5	2.5	34.6	0.9	327	481
ls 6a	10.5	1.5	38.1	0.4	393	444
ls 7b	29.0	1.0	34.6	0.6	326	481
ls 9	51.5	1.5	33.2	0.6	312	502
ls 10	78.0	2.0	30.3	0.8	374	518

Holbrook (L6)

linescan #	grain radius (μm)	grain radius error (μm)	core Ni wt%	core Ni wt% error	rim Tc (Celsius)	core Tc (Celsius)
ls 2	14.0	1.5	31.5	0.4	426	508
ls 7	29.3	1.9	24.3	0.6	419	563
ls 9	16.8	3.0	33.0	0.2	458	496
ls 10	24.5	2.5	25.5	0.4	459	554
ls 15	17.1	2.1	31.4	0.2	452	509
ls 18	12.5	2.3	29.3	0.5	472	526
ls 19	36.6	3.9	24.8	0.4	461	559
ls 20	25.4	4.0	29.2	0.8	408	526
ls 21	87.8	2.8	15.7	1.0	401	633
ls 22	41.5	2.3	22.2	0.5	445	577
ls 23	19.8	2.7	24.5	0.6	499	561
ls 26	49.8	2.6	20.4	0.7	464	591
ls 27	35.4	3.9	24.5	0.5	475	561
ls 28	41.2	1.5	24.7	0.6	409	559
ls 31	36.5	2.4	23.0	0.7	409	572
ls 32	43.7	1.9	25.4	0.5	449	554
ls 33	23.4	3.4	28.5	0.3	489	532
ls 36	30.0	2.4	24.4	0.4	478	561
ls 38	44.2	3.5	23.0	0.4	472	572
ls 40	30.9	2.8	26.2	0.4	445	548
ls 44	28.3	2.9	35.4	0.1	448	474
ls 49	24.1	2.9	29.1	0.2	474	527
ls 50	14.9	1.3	29.4	0.4	441	525
ls 53	59.0	3.1	24.2	0.5	445	563

ls 54	55.8	2.5	23.4	0.6	408	569
ls 55	29.4	3.1	27.2	0.5	482	541

Kernouve (H6)

linescan #	grain radius (μm)	grain radius error (μm)	core Ni wt%	core Ni wt% error	rim Tc (Celsius)	core Tc (Celsius)
ls 1	33.0	2.0	32.1	0.8	113	503
ls 3	36.5	1.5	32.3	0.5	405	501
ls 5	50.0	2.0	29.8	0.7	284	522
ls 8	11.0	1.0	38.3	0.4	394	443
ls 9	62.5	2.5	29.3	0.6	376	526
ls 13	6.0	1.0	40.9	0.4	259	411
ls 16	25.0	2.0	39.9	0.4	255	423
ls 20	16.0	1.0	38.4	0.6	208	442
ls 21	68.5	3.5	32.0	0.5	387	504
ls 22	61.5	2.5	29.8	0.5	401	522
ls 23	13.5	2.5	38.6	0.6	113	439

Leedey (L6)

linescan #	grain radius (μm)	grain radius error (μm)	core Ni wt%	core Ni wt% error	rim Tc (Celsius)	core Tc (Celsius)
ls 1	54.0	3.0	30.8	0.8	381	514
ls 3	36.0	2.0	33.1	0.6	385	495
ls 4	45.0	2.0	26.5	2.0	362	547
ls 9	35.0	3.0	31.3	0.6	394	510
ls 14	49.5	2.5	30.3	0.8	238	518
ls 15	54.5	2.5	30.9	0.4	428	513
ls 16	37.0	3.0	33.1	0.4	404	495
ls 17	24.5	3.5	36.0	0.6	331	467
ls 18	27.5	2.5	33.8	0.4	400	489
ls 19	11.0	2.0	39.9	0.5	189	424
ls 20	51.0	2.0	30.5	0.7	384	516
ls 21	71.0	4.0	30.7	0.6	404	514
ls 22	46.0	3.0	32.7	0.7	298	497
ls 25	51.5	3.5	30.7	0.5	409	514
ls 26	58.5	4.5	35.6	0.3	407	472
ls 27	59.0	4.0	29.4	0.6	404	524
ls 29	50.5	2.5	31.1	0.8	113	511
ls 31	83.5	3.5	32.8	0.5	370	497
ls 32	49.0	4.0	31.9	0.7	329	504

Morrow County (L6)

linescan #	grain radius (μm)	grain radius error (μm)	core Ni wt%	core Ni wt% error	rim Tc (Celsius)	core Tc (Celsius)
ls 5	91.0	12.0	23.9	0.4	516	566
ls 6	36.0	7.0	27.0	1.0	469	542
ls 7	31.0	4.0	29.2	0.4	447	526
ls 10	16.5	2.5	31.2	0.3	450	511
ls 35	92.0	6.0	26.0	0.6	489	550
ls 36	68.5	9.5	25.5	0.4	491	554
ls 37	30.0	5.0	27.0	0.5	498	542
ls 39	30.5	8.5	26.1	0.5	494	550
ls 45	23.0	4.0	32.0	0.5	470	505
ls 46	40.0	8.0	27.2	0.5	484	541
ls 49	24.0	6.0	27.9	0.4	480	536

Park (L6)

linescan #	grain radius (μm)	grain radius error (μm)	core Ni wt%	core Ni wt% error	rim Tc (Celsius)	core Tc (Celsius)
ls 1	33.5	1.5	17.4	0.5	503	617
ls 2a	24.5	1.5	21.1	0.5	441	587
ls 2b	32.5	1.5	17.8	0.6	498	614
ls 3a	35.5	2.5	16.6	0.7	435	625
ls 3c	13.5	1.5	22.3	0.5	492	577
ls 4a	90.0	4.0	14.9	0.4	545	643
ls 4b1	25.5	1.5	18.7	0.7	470	606
ls 4b2	37.0	1.0	16.4	0.5	540	628
ls 4c	19.5	1.5	19.9	0.7	461	596
ls 4d	22.0	1.0	19.9	0.4	491	596
ls 4e	21.5	1.5	20.2	0.3	526	593
ls 5	83.5	4.5	14.5	0.5	455	646
ls 6b1	40.0	3.0	17.7	0.8	423	615
ls 6b2	16.0	2.0	20.3	0.6	476	593
ls 6e	40.0	4.0	16.3	0.7	454	628
ls 6f	46.0	2.0	15.6	0.6	521	636
ls 6g	18.0	2.0	20.1	0.5	529	594

Portales Valley (H6)

linescan #	grain radius (μm)	grain radius error (μm)	core Ni wt%	core Ni wt% error	rim Tc (Celsius)	core Tc (Celsius)
ls 5	14	2	39.8	0.4	298	424
ls 8	13.5	1.5	39.5	0.5	170	428
ls 9	27	2	32.2	0.7	389	502
ls 14	19	2	33.6	0.9	113	490
ls 15	21.5	2.5	33.6	0.9	307	490
ls 16	22	2	32.9	0.7	385	496
ls 17	11	2	39.8	0.6	113	494
ls 19a	12	2	37.3	0.4	402	454
la 19b	13.5	3.5	39.2	0.3	338	432
ls 20	42	2	30.3	0.7	402	518
ls 27	100	4	26.4	0.8	408	547
ls 29	10	2	39.3	0.1	298	443
ls 30	14	2	38.2	0.6	303	456
ls 31	31.5	3.5	34.2	0.4	390	486
ls 32	16.5	1.5	35.8	0.5	327	469
ls 34	11.5	4.5	38.8	0.2	292	437
ls 35	41	2	28.7	1.0	402	530
ls 37	59.5	3.5	29.6	0.5	404	523
ls 39	39.5	3.5	31.8	1.0	204	506
ls 41	45	2	29.0	0.7	404	528

Queen's Mercy (H6)

linescan #	grain radius (μm)	grain radius error (μm)	core Ni wt%	core Ni wt% error	rim Tc (Celsius)	core Tc (Celsius)
ls 5	13.5	1.5	38.2	0.7	113	444
ls 7	14.0	1.0	37.2	0.7	113	456
ls 8	19.5	1.5	35.9	0.6	287	469
ls 9	26.5	1.5	34.2	0.8	222	485
ls 10	25.5	1.5	34.3	0.6	326	484
ls 12	36.5	1.5	32.2	0.6	367	502
ls 15	66.0	3.0	33.0	0.6	295	496
ls 16a	24.0	2.0	34.5	0.6	235	482
ls 16b	10.0	2.0	41.1	0.5	267	410
ls 17	55.5	2.5	32.3	0.3	406	501

APPENDIX F: Wood plots

Shown here are metallographic cooling rate plots with data from the individual metal grains from each sample. Cooling rate isolines are taken from Wood (1967) as modified by Willis and Goldstein (1981).

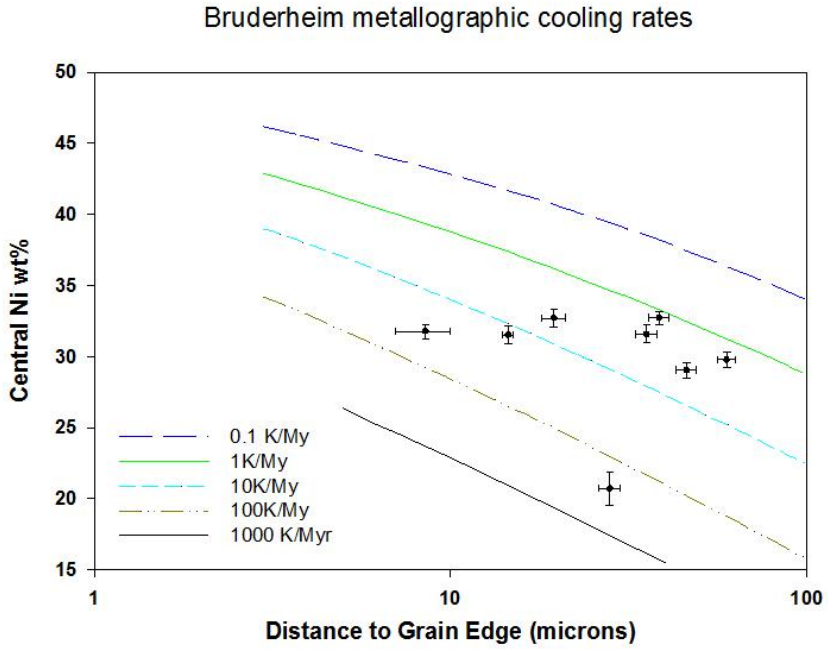

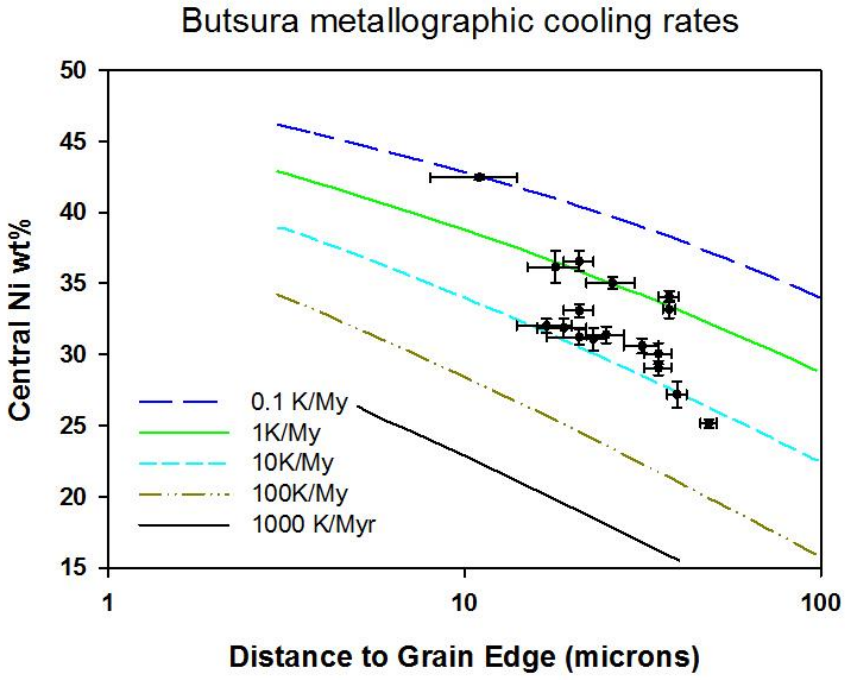

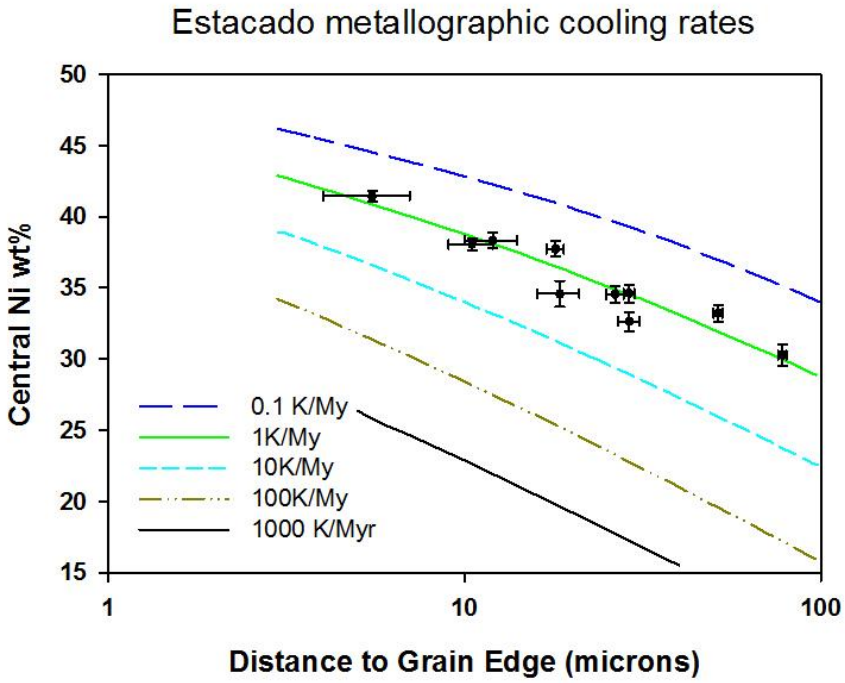
Estacado metallographic cooling rates
Central Ni wt%
50
45
40
35
30
25
20
15
1
10
100
Distance to Grain Edge (microns)
0.1 K/My
1K/My
10K/My
100K/My
1000 K/Myr

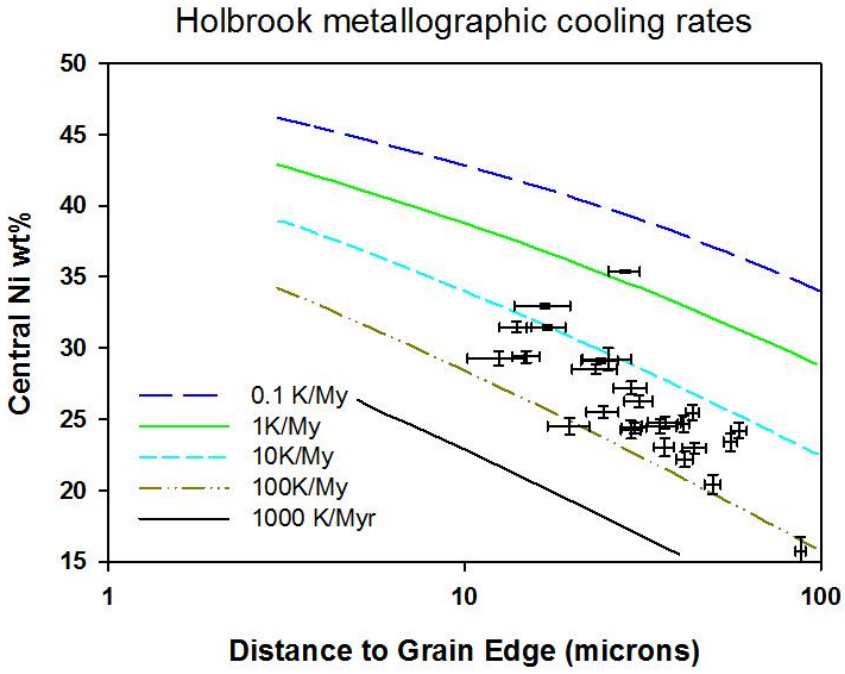
Holbrook metallographic cooling rates
Central Ni wt%
50
45
40
35
30
25
20
15
1
10
100
Distance to Grain Edge (microns)
0.1 K/My
1K/My
10K/My
100K/My
1000 K/Myr

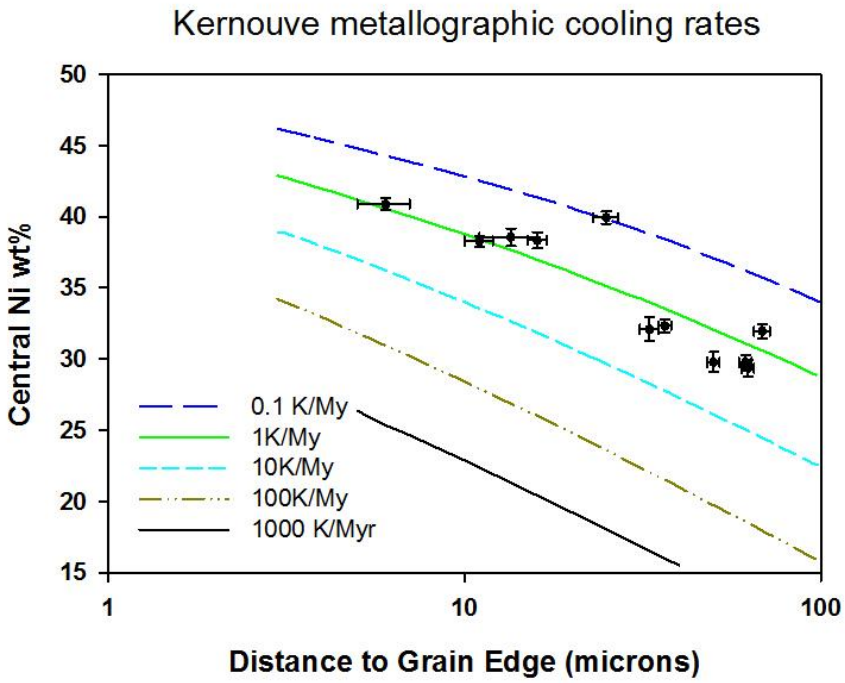
Kernouve metallographic cooling rates
Central Ni wt%
50
45
40
35
30
25
20
15
1
10
100
Distance to Grain Edge (microns)
0.1 K/My
1K/My
10K/My
100K/My
1000 K/Myr

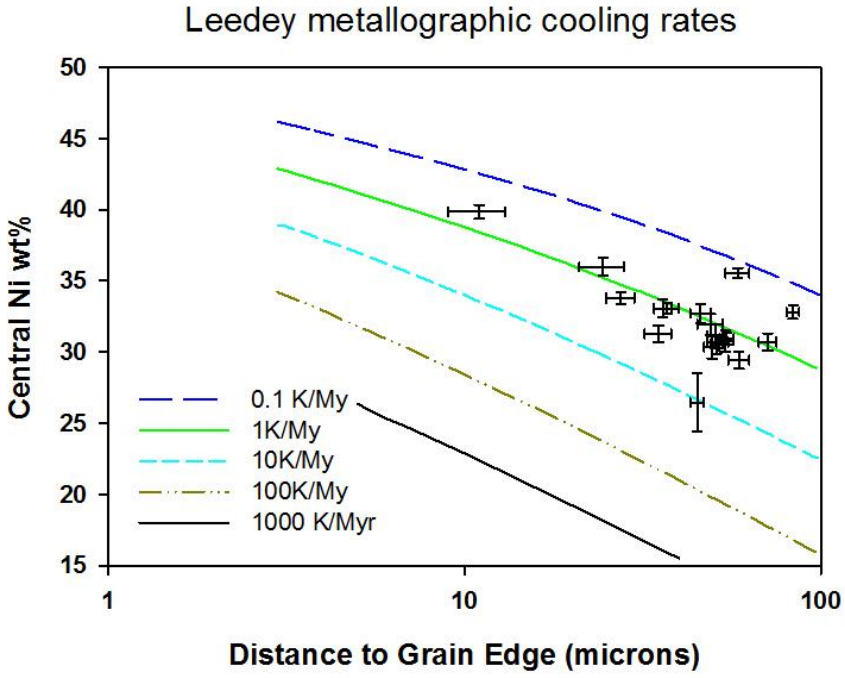
Leedey metallographic cooling rates
Central Ni wt%
50
45
40
35
30
25
20
15
1
10
100
Distance to Grain Edge (microns)
0.1 K/My
1K/My
10K/My
100K/My
1000 K/Myr

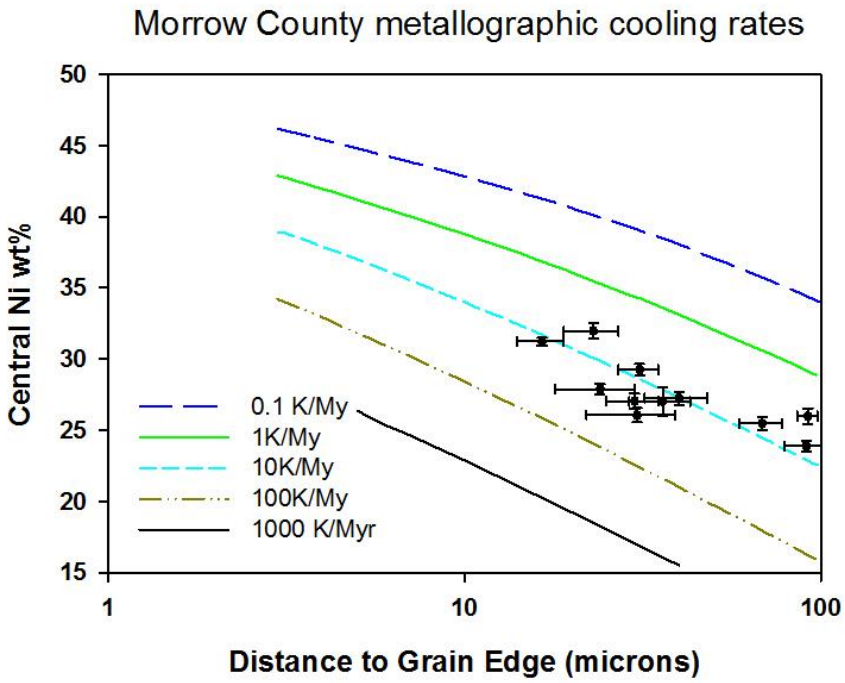
Morrow County metallographic cooling rates
Central Ni wt%
50
45
40
35
30
25
20
15
1
10
100
Distance to Grain Edge (microns)
0.1 K/My
1K/My
10K/My
100K/My
1000 K/Myr

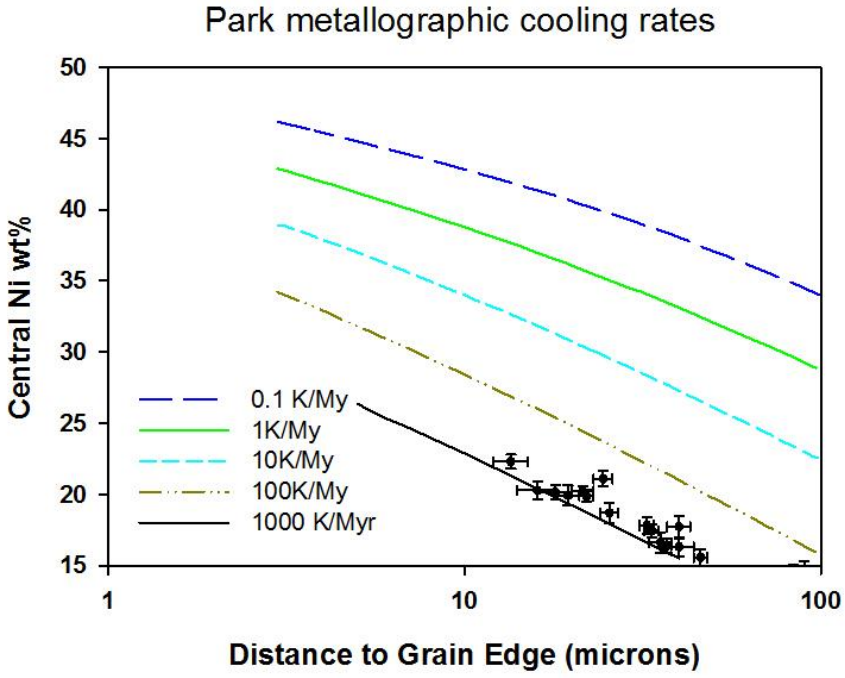
Park metallographic cooling rates
Central Ni wt%
50
45
40
35
30
25
20
15
1
10
100
Distance to Grain Edge (microns)
0.1 K/My
1K/My
10K/My
100K/My
1000 K/Myr

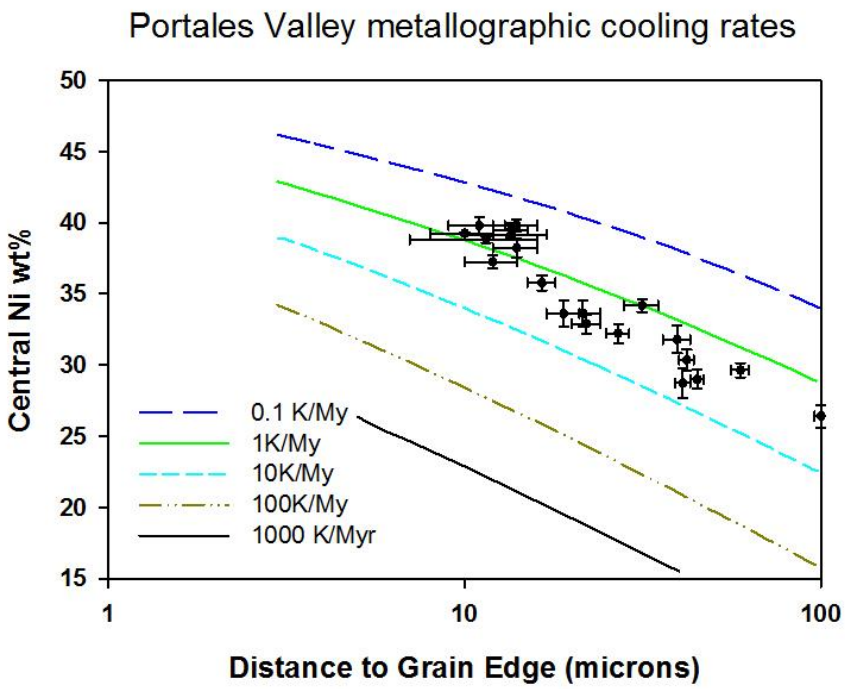
Portales Valley metallographic cooling rates
Central Ni wt%
50
45
40
35
30
25
20
15
1
10
100
Distance to Grain Edge (microns)
0.1 K/My
1K/My
10K/My
100K/My
1000 K/Myr

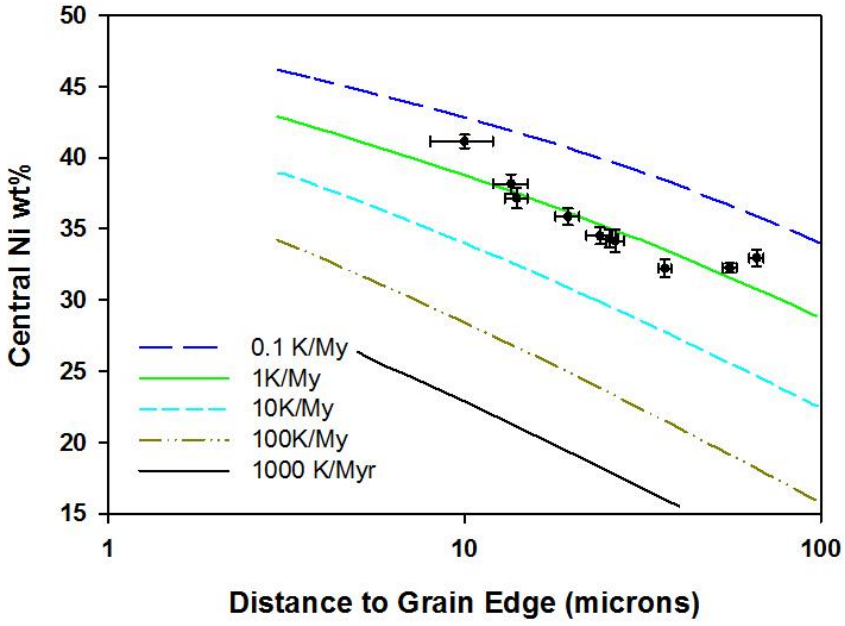
Queen's Mercy metallographic cooling rates
Central Ni wt%
50
45
40
35
30
25
20
15
1
10
100
Distance to Grain Edge (microns)
0.1 K/My
1K/My
10K/My
100K/My
1000 K/Myr

APPENDIX G: Cooling rate plots

This appendix contains three closure temperature vs. cooling rate plots for each sample. For each sample, the first two are two plots calculated using the Dodson (1973) formulation as modified by Ganguly and Tirone (1999) using two different starting temperatures, which are specified in the plot header. The closure temperatures and mineral compositions (where applicable for the calculation of diffusion coefficients) are averages of the values from their respective grain positions (rim, intermediate, or core). Cooling rates are calculated from these averages. For metallographic cooling rates, averages of cooling rate, rim and core closure temperatures are used. The third plot for each sample shows cooling rates calculated from the original Dodson (1973) formula for each individual mineral pair, with representative error bars for each system except metals.

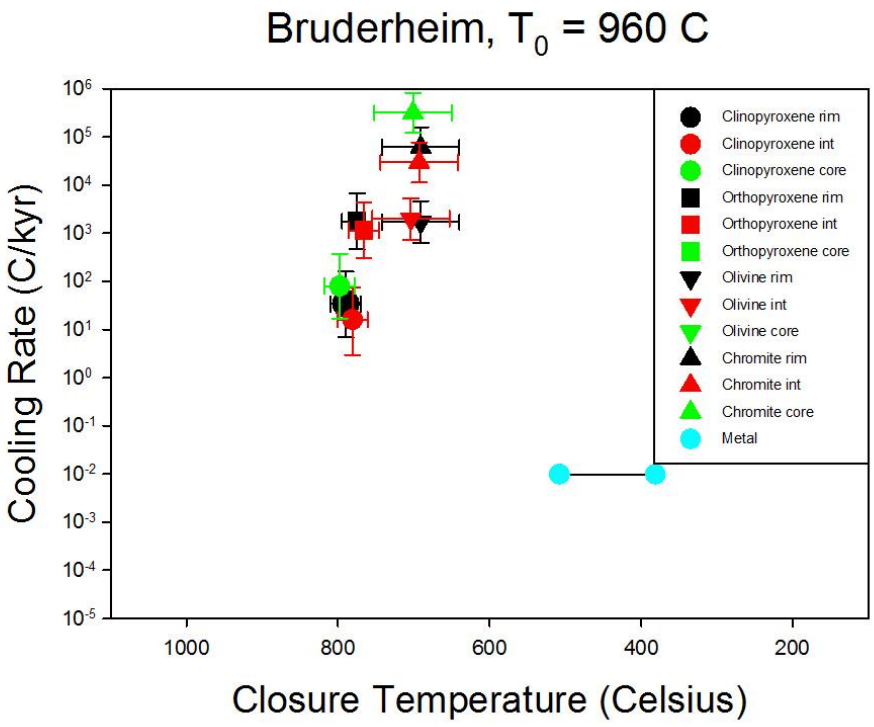

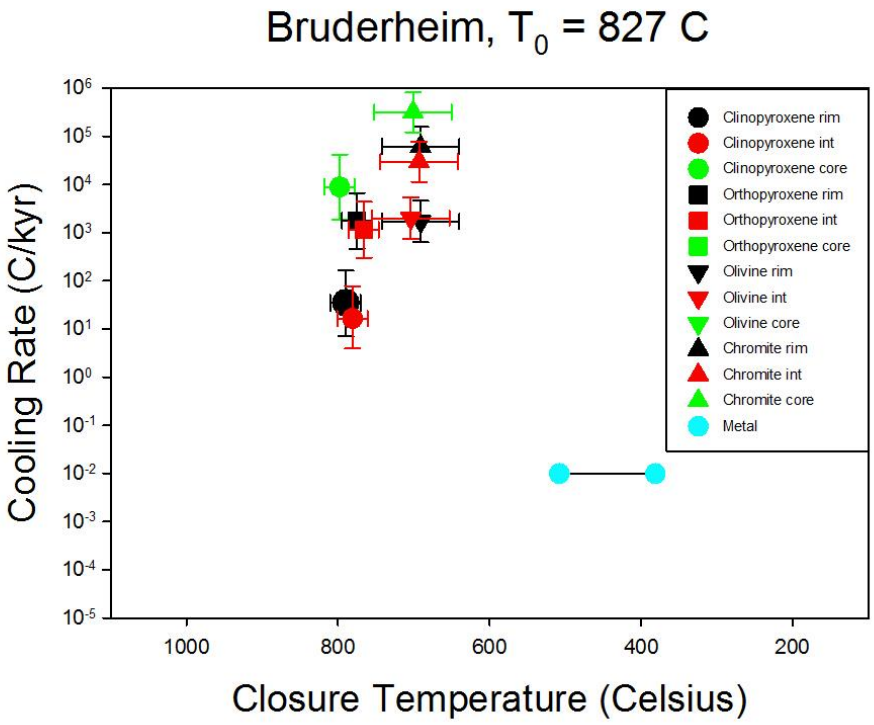
Bruderheim, T_0 = 827 C
Cooling Rate (C/kyr)
10^6
10^5
10^4
10^3
10^2
10^1
10^0
10^{-1}
10^{-2}
10^{-3}
10^{-4}
10^{-5}
1000
800
600
400
200
Closure Temperature (Celsius)
Clinopyroxene rim
Clinopyroxene int
Clinopyroxene core
Orthopyroxene rim
Orthopyroxene int
Orthopyroxene core
Olivine rim
Olivine int
Olivine core
Chromite rim
Chromite int
Chromite core
Metal

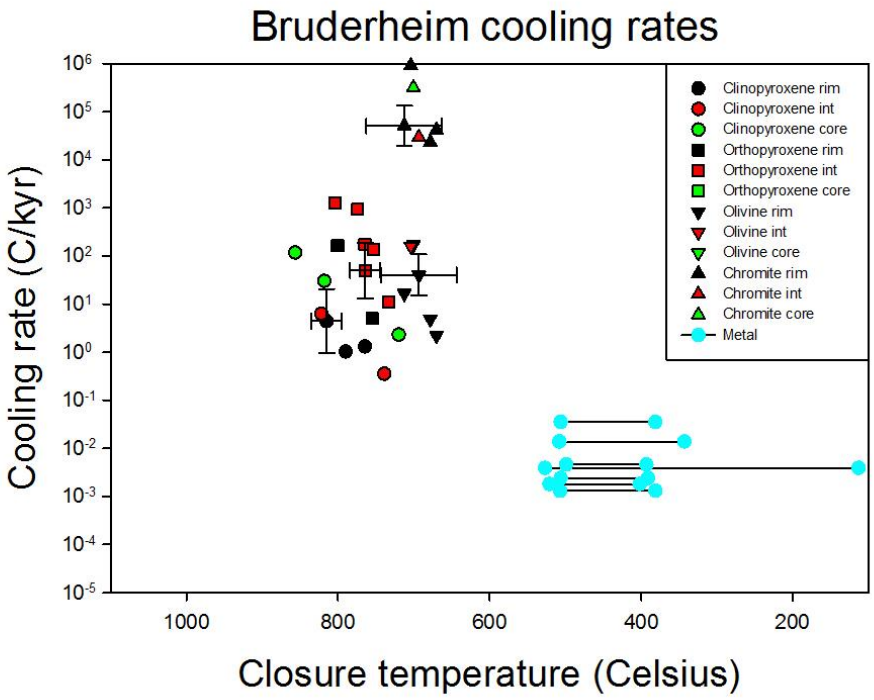
Bruderheim cooling rates
Cooling rate (C/kyr)
10^6
10^5
10^4
10^3
10^2
10^1
10^0
10^{-1}
10^{-2}
10^{-3}
10^{-4}
10^{-5}
1000
800
600
400
200
Closure temperature (Celsius)
Clinopyroxene rim
Clinopyroxene int
Clinopyroxene core
Orthopyroxene rim
Orthopyroxene int
Orthopyroxene core
Olivine rim
Olivine int
Olivine core
Chromite rim
Chromite int
Chromite core
Metal

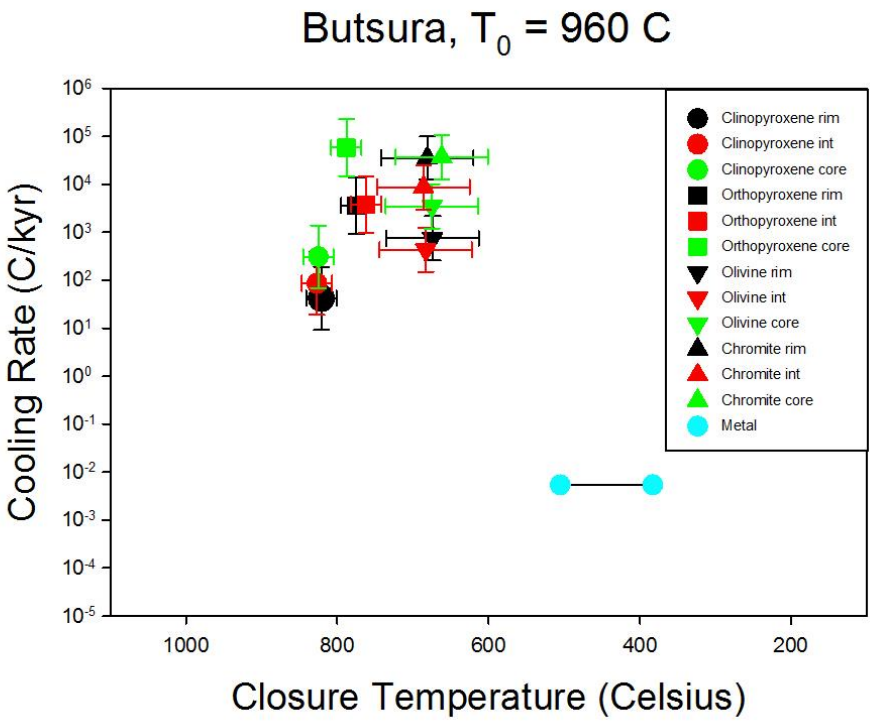
Butsura, T_0 = 960 C
Cooling Rate (C/kyr)
10^6
10^5
10^4
10^3
10^2
10^1
10^0
10^{-1}
10^{-2}
10^{-3}
10^{-4}
10^{-5}
1000
800
600
400
200
Closure Temperature (Celsius)
Clinopyroxene rim
Clinopyroxene int
Clinopyroxene core
Orthopyroxene rim
Orthopyroxene int
Orthopyroxene core
Olivine rim
Olivine int
Olivine core
Chromite rim
Chromite int
Chromite core
Metal

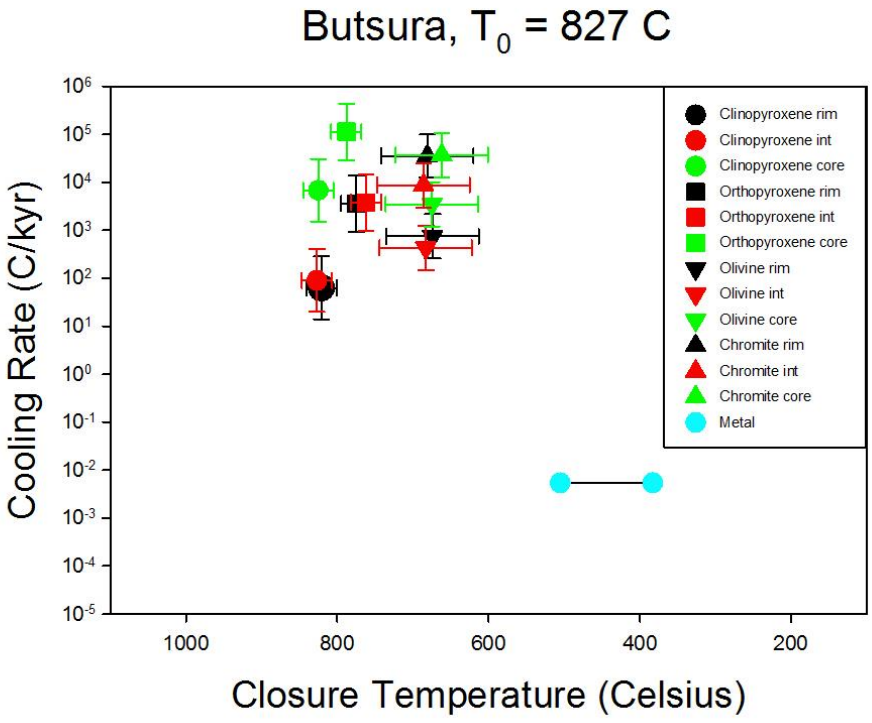
Butsura, T_0 = 827 C
Cooling Rate (C/kyr)
10^6
10^5
10^4
10^3
10^2
10^1
10^0
10^{-1}
10^{-2}
10^{-3}
10^{-4}
10^{-5}
1000
800
600
400
200
Closure Temperature (Celsius)
Clinopyroxene rim
Clinopyroxene int
Clinopyroxene core
Orthopyroxene rim
Orthopyroxene int
Orthopyroxene core
Olivine rim
Olivine int
Olivine core
Chromite rim
Chromite int
Chromite core
Metal

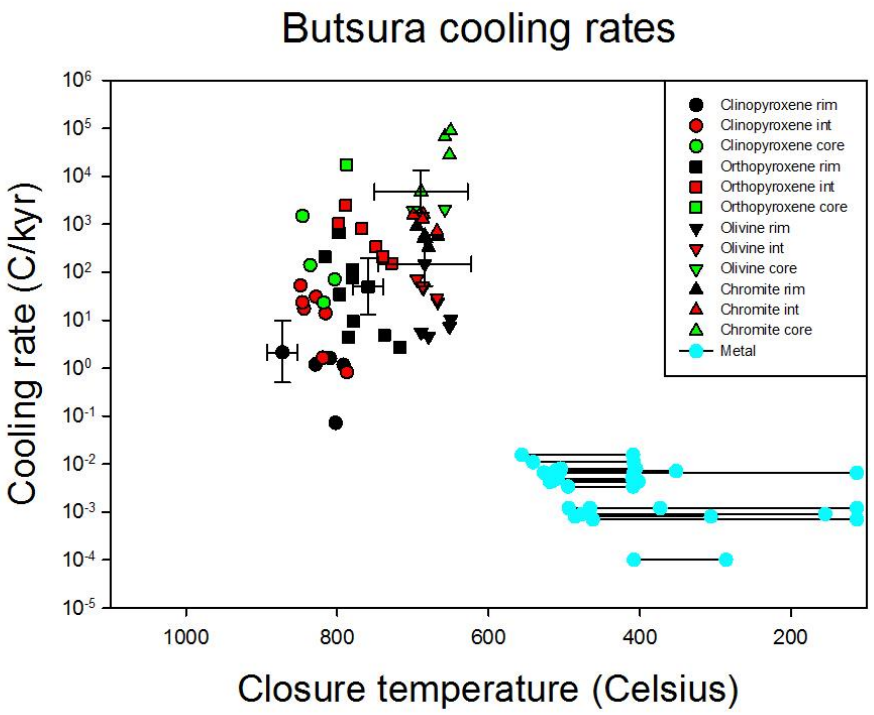
Butsura cooling rates
Cooling rate (C/kyr)
Closure temperature (Celsius)
Clinopyroxene rim
Clinopyroxene int
Clinopyroxene core
Orthopyroxene rim
Orthopyroxene int
Orthopyroxene core
Olivine rim
Olivine int
Olivine core
Chromite rim
Chromite int
Chromite core
Metal

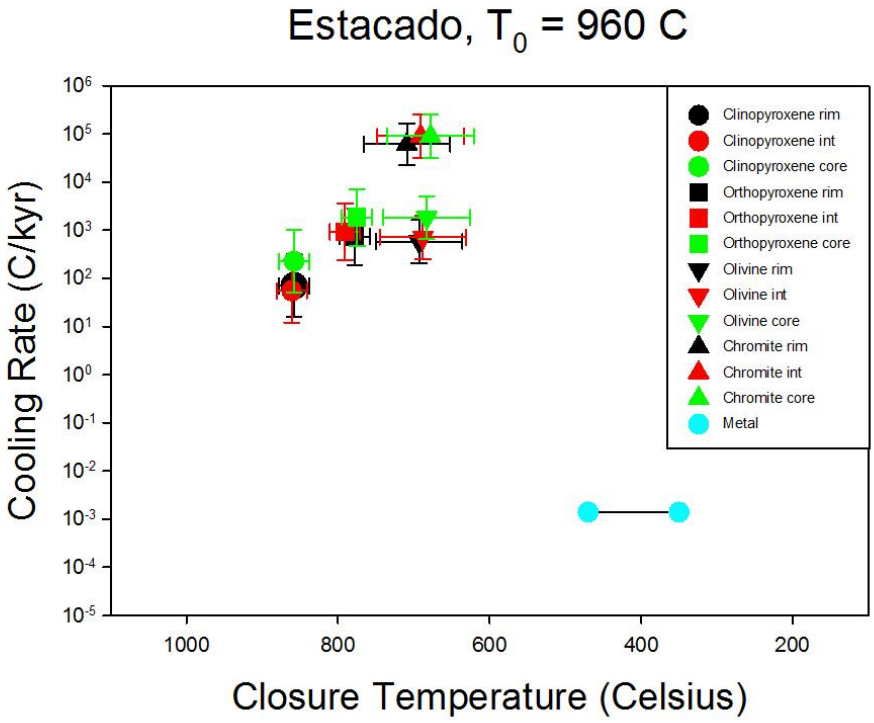
Estacado, T0 = 960 C
Cooling Rate (C/kyr)
Closure Temperature (Celsius)
Clinopyroxene rim
Clinopyroxene int
Clinopyroxene core
Orthopyroxene rim
Orthopyroxene int
Orthopyroxene core
Olivine rim
Olivine int
Olivine core
Chromite rim
Chromite int
Chromite core
Metal

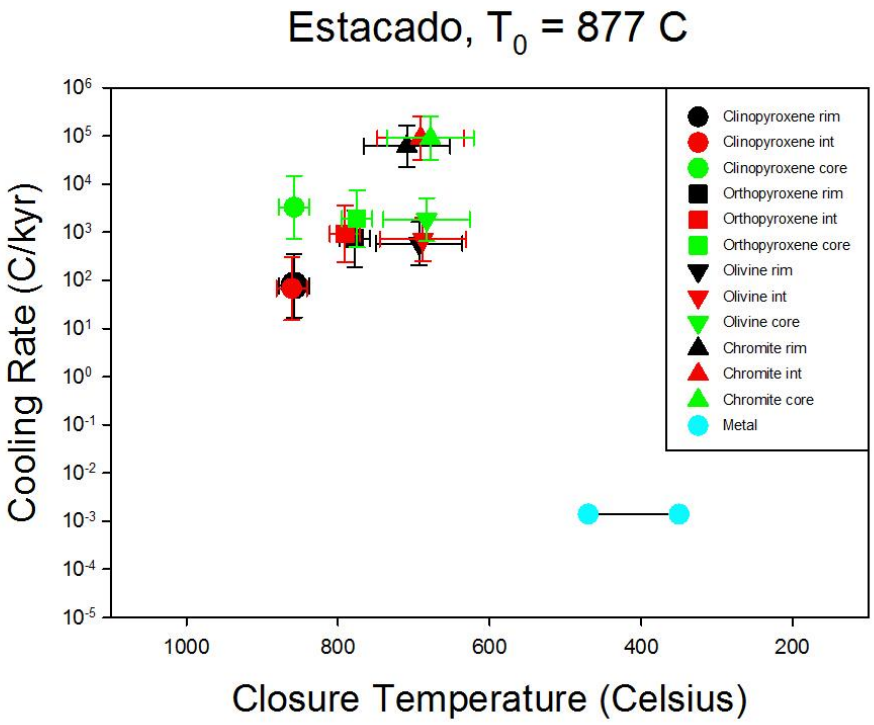
Estacado, T_0 = 877 C
Cooling Rate (C/kyr)
10^6
10^5
10^4
10^3
10^2
10^1
10^0
10^{-1}
10^{-2}
10^{-3}
10^{-4}
10^{-5}
1000
800
600
400
200
Closure Temperature (Celsius)
Clinopyroxene rim
Clinopyroxene int
Clinopyroxene core
Orthopyroxene rim
Orthopyroxene int
Orthopyroxene core
Olivine rim
Olivine int
Olivine core
Chromite rim
Chromite int
Chromite core
Metal

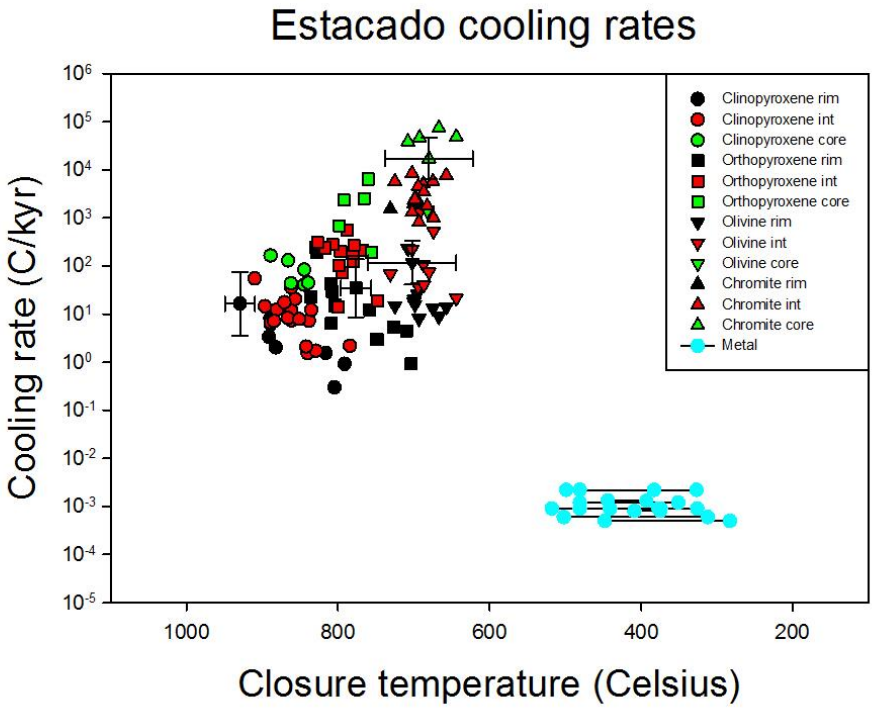
Estacado cooling rates
Cooling rate (C/kyr)
10^6
10^5
10^4
10^3
10^2
10^1
10^0
10^{-1}
10^{-2}
10^{-3}
10^{-4}
10^{-5}
1000
800
600
400
200
Closure temperature (Celsius)
Clinopyroxene rim
Clinopyroxene int
Clinopyroxene core
Orthopyroxene rim
Orthopyroxene int
Orthopyroxene core
Olivine rim
Olivine int
Olivine core
Chromite rim
Chromite int
Chromite core
Metal

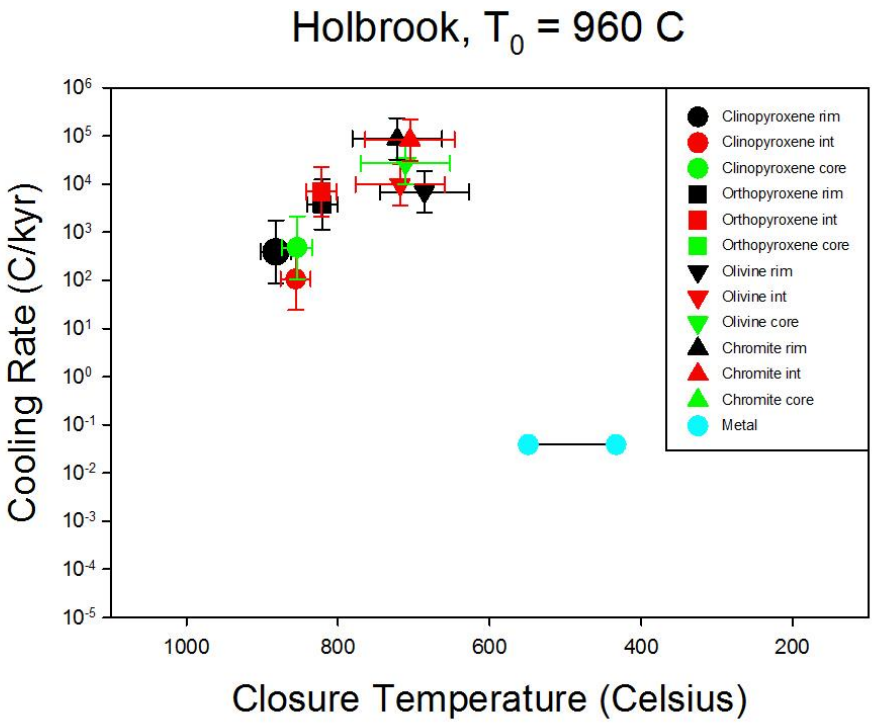
Holbrook, T_0 = 960 C
Cooling Rate (C/kyr)
10^6
10^5
10^4
10^3
10^2
10^1
10^0
10^{-1}
10^{-2}
10^{-3}
10^{-4}
10^{-5}
1000
800
600
400
200
Closure Temperature (Celsius)
Clinopyroxene rim
Clinopyroxene int
Clinopyroxene core
Orthopyroxene rim
Orthopyroxene int
Orthopyroxene core
Olivine rim
Olivine int
Olivine core
Chromite rim
Chromite int
Chromite core
Metal

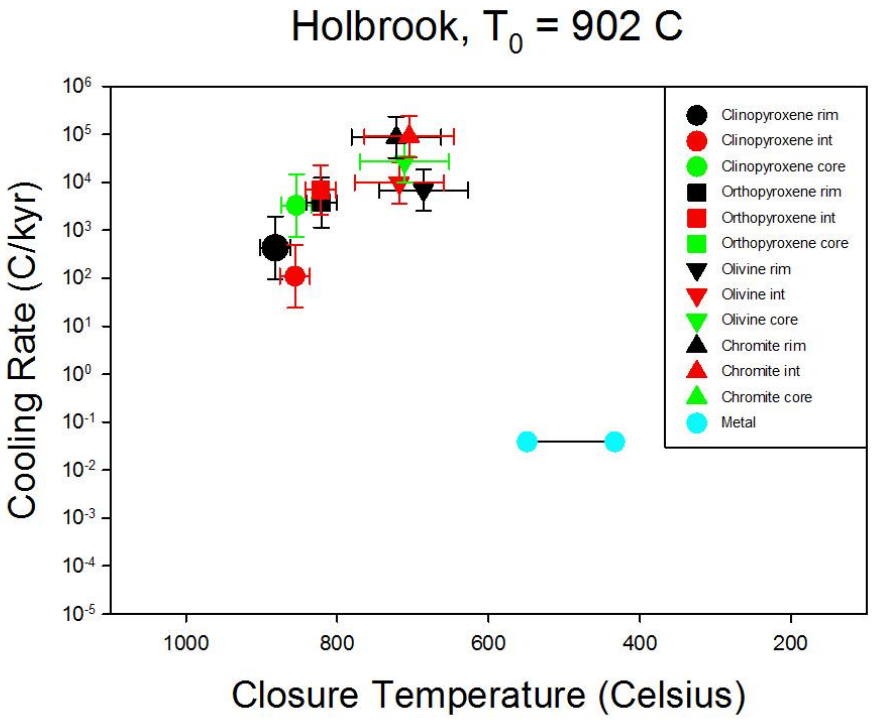
Holbrook, T_0 = 902 C
Cooling Rate (C/kyr)
10^6
10^5
10^4
10^3
10^2
10^1
10^0
10^{-1}
10^{-2}
10^{-3}
10^{-4}
10^{-5}
1000
800
600
400
200
Closure Temperature (Celsius)
Clinopyroxene rim
Clinopyroxene int
Clinopyroxene core
Orthopyroxene rim
Orthopyroxene int
Orthopyroxene core
Olivine rim
Olivine int
Olivine core
Chromite rim
Chromite int
Chromite core
Metal

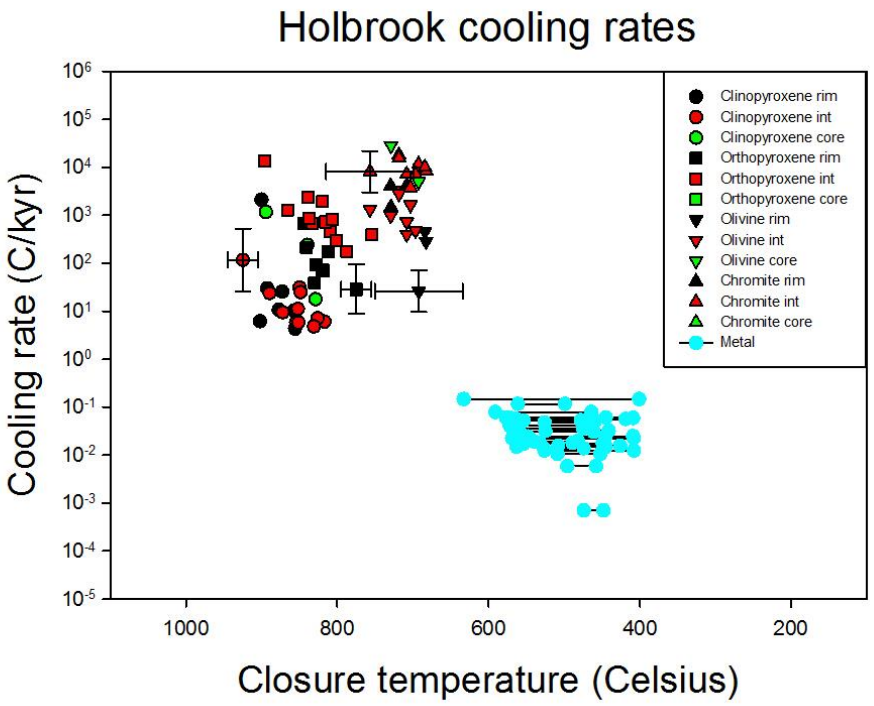
Holbrook cooling rates
Cooling rate (C/kyr)
Closure temperature (Celsius)
Clinopyroxene rim
Clinopyroxene int
Clinopyroxene core
Orthopyroxene rim
Orthopyroxene int
Orthopyroxene core
Olivine rim
Olivine int
Olivine core
Chromite rim
Chromite int
Chromite core
Metal

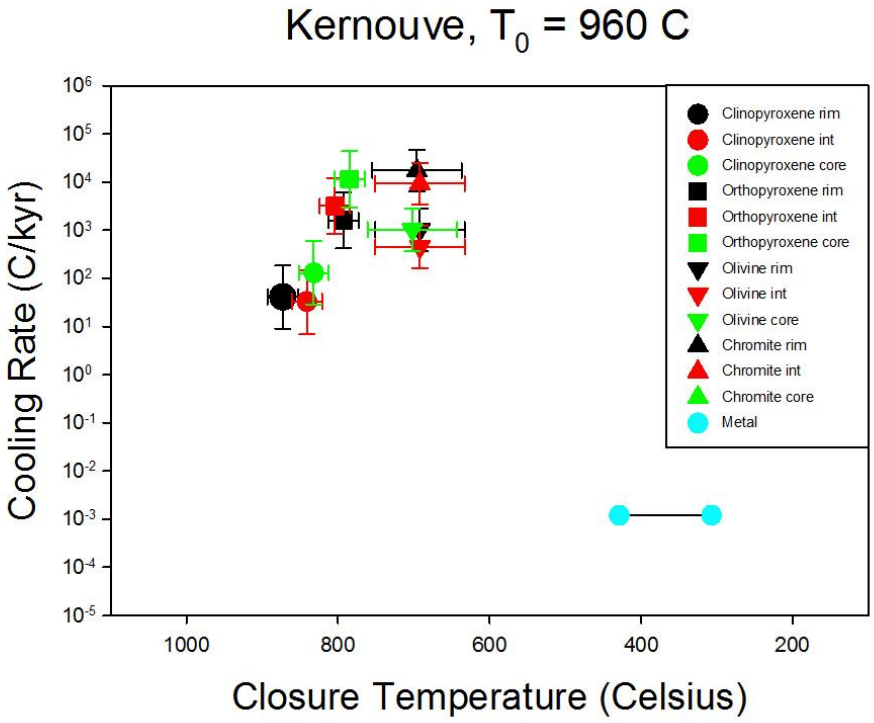
Kernouve, T0 = 960 C
Cooling Rate (C/kyr)
Closure Temperature (Celsius)
Clinopyroxene rim
Clinopyroxene int
Clinopyroxene core
Orthopyroxene rim
Orthopyroxene int
Orthopyroxene core
Olivine rim
Olivine int
Olivine core
Chromite rim
Chromite int
Chromite core
Metal

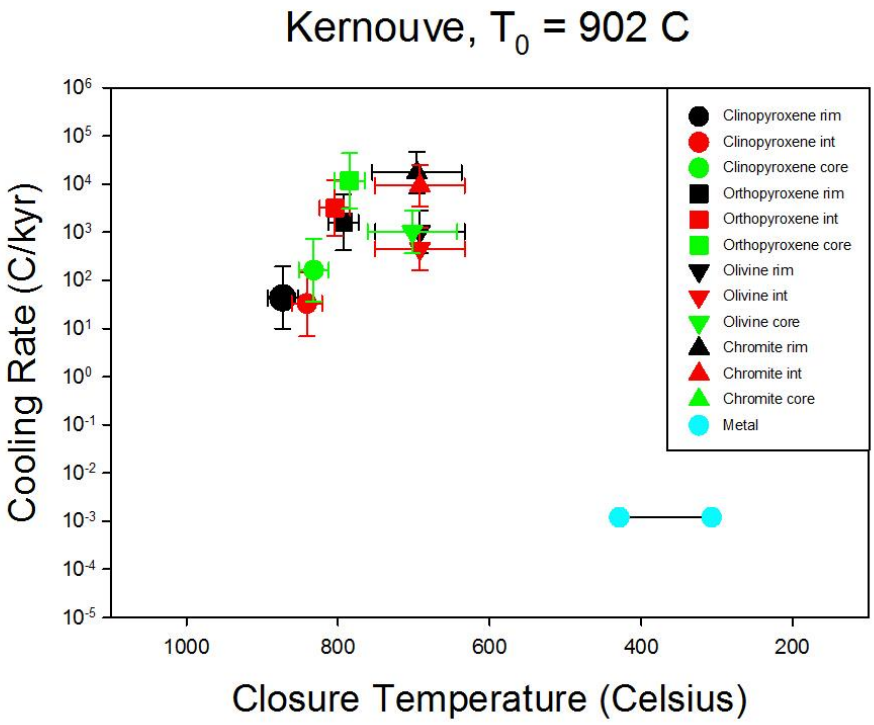
Kernouve, T_0 = 902 C
Cooling Rate (C/kyr)
10^6
10^5
10^4
10^3
10^2
10^1
10^0
10^{-1}
10^{-2}
10^{-3}
10^{-4}
10^{-5}
1000
800
600
400
200
Closure Temperature (Celsius)
Clinopyroxene rim
Clinopyroxene int
Clinopyroxene core
Orthopyroxene rim
Orthopyroxene int
Orthopyroxene core
Olivine rim
Olivine int
Olivine core
Chromite rim
Chromite int
Chromite core
Metal

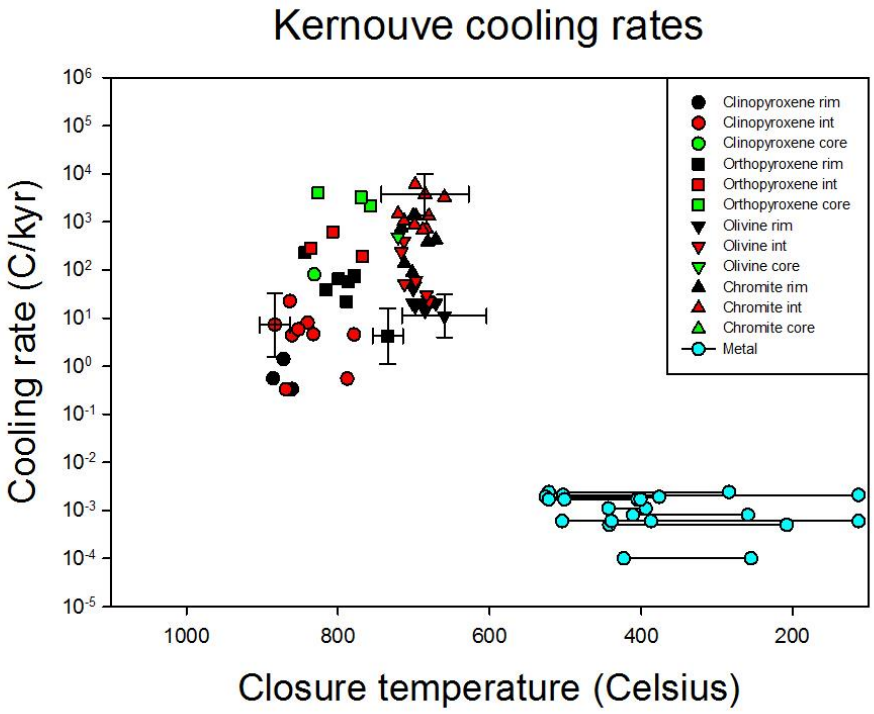
Kernouve cooling rates
Cooling rate (C/kyr)
10^6
10^5
10^4
10^3
10^2
10^1
10^0
10^{-1}
10^{-2}
10^{-3}
10^{-4}
10^{-5}
1000
800
600
400
200
Closure temperature (Celsius)
Clinopyroxene rim
Clinopyroxene int
Clinopyroxene core
Orthopyroxene rim
Orthopyroxene int
Orthopyroxene core
Olivine rim
Olivine int
Olivine core
Chromite rim
Chromite int
Chromite core
Metal

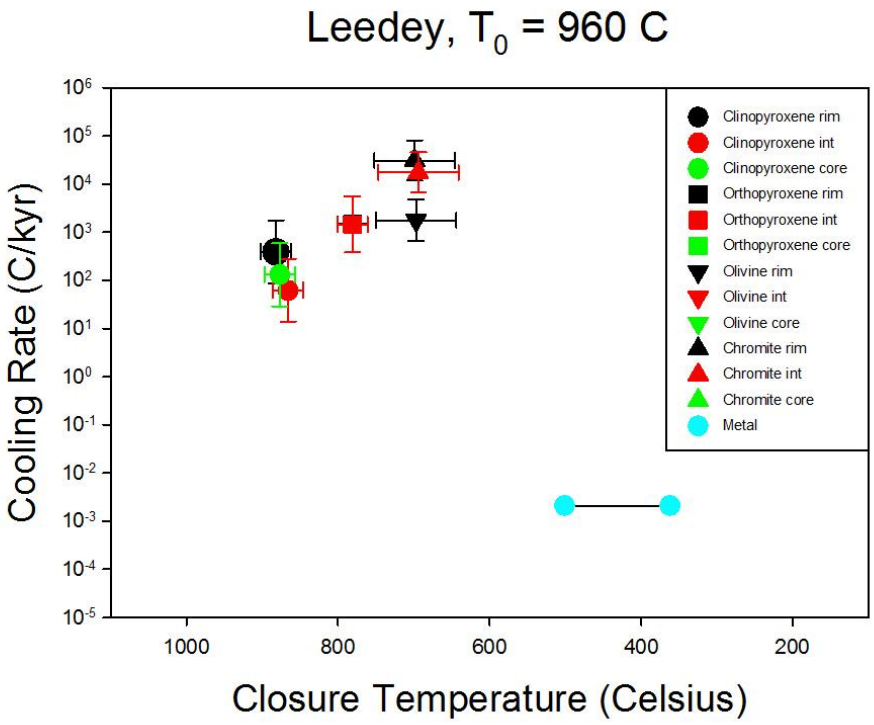
Leedey, T_0 = 960 C
Cooling Rate (C/kyr)
10^6
10^5
10^4
10^3
10^2
10^1
10^0
10^{-1}
10^{-2}
10^{-3}
10^{-4}
10^{-5}
1000
800
600
400
200
Closure Temperature (Celsius)
Clinopyroxene rim
Clinopyroxene int
Clinopyroxene core
Orthopyroxene rim
Orthopyroxene int
Orthopyroxene core
Olivine rim
Olivine int
Olivine core
Chromite rim
Chromite int
Chromite core
Metal

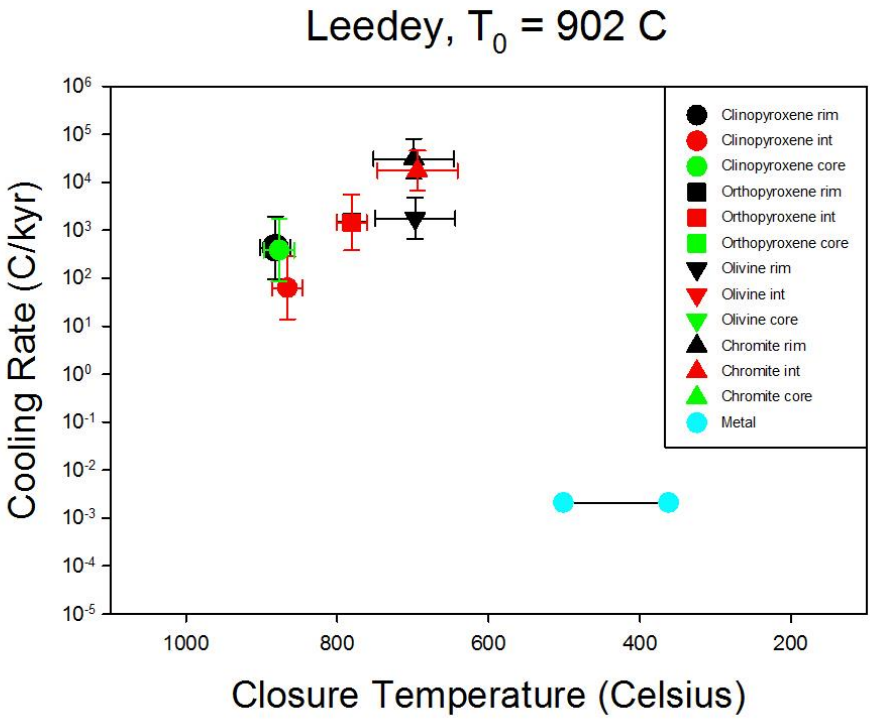
Leedey, T_0 = 902 C
Cooling Rate (C/kyr)
10^6
10^5
10^4
10^3
10^2
10^1
10^0
10^{-1}
10^{-2}
10^{-3}
10^{-4}
10^{-5}
1000
800
600
400
200
Closure Temperature (Celsius)
Clinopyroxene rim
Clinopyroxene int
Clinopyroxene core
Orthopyroxene rim
Orthopyroxene int
Orthopyroxene core
Olivine rim
Olivine int
Olivine core
Chromite rim
Chromite int
Chromite core
Metal

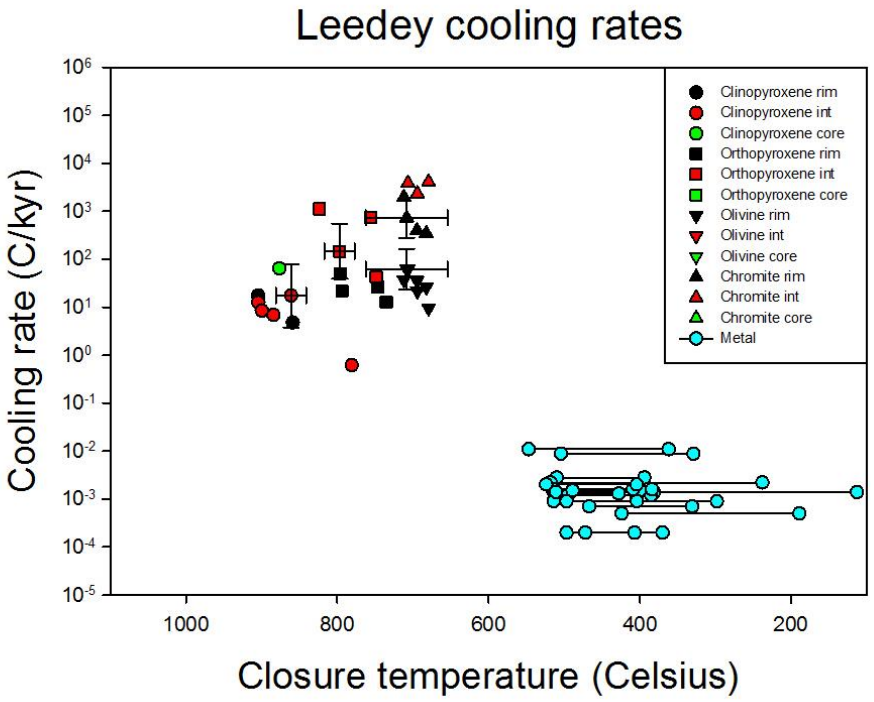
Leedey cooling rates
Cooling rate (C/kyr)
Closure temperature (Celsius)
Clinopyroxene rim
Clinopyroxene int
Clinopyroxene core
Orthopyroxene rim
Orthopyroxene int
Orthopyroxene core
Olivine rim
Olivine int
Olivine core
Chromite rim
Chromite int
Chromite core
Metal

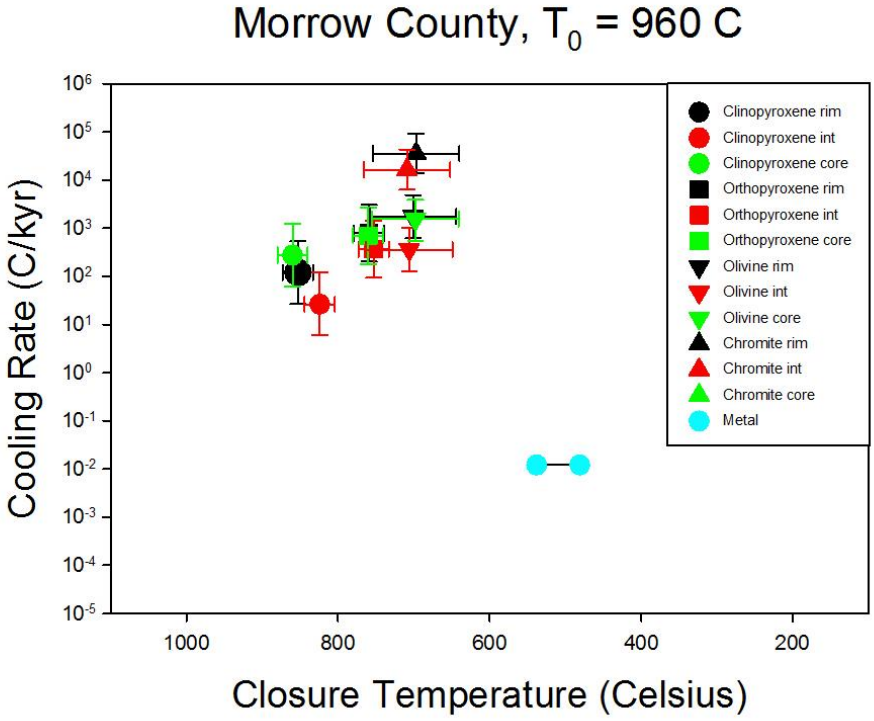
Morrow County, T0 = 960 C
Cooling Rate (C/kyr)
Closure Temperature (Celsius)
Clinopyroxene rim
Clinopyroxene int
Clinopyroxene core
Orthopyroxene rim
Orthopyroxene int
Orthopyroxene core
Olivine rim
Olivine int
Olivine core
Chromite rim
Chromite int
Chromite core
Metal

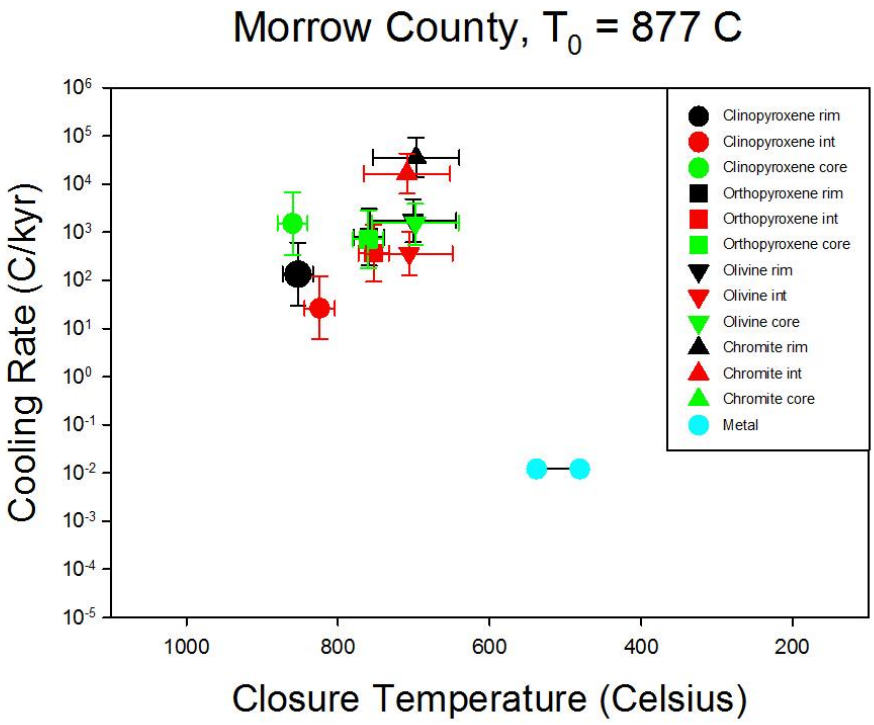
Morrow County, T_0 = 877 C
Cooling Rate (C/kyr)
10^6
10^5
10^4
10^3
10^2
10^1
10^0
10^{-1}
10^{-2}
10^{-3}
10^{-4}
10^{-5}
1000
800
600
400
200
Closure Temperature (Celsius)
Clinopyroxene rim
Clinopyroxene int
Clinopyroxene core
Orthopyroxene rim
Orthopyroxene int
Orthopyroxene core
Olivine rim
Olivine int
Olivine core
Chromite rim
Chromite int
Chromite core
Metal

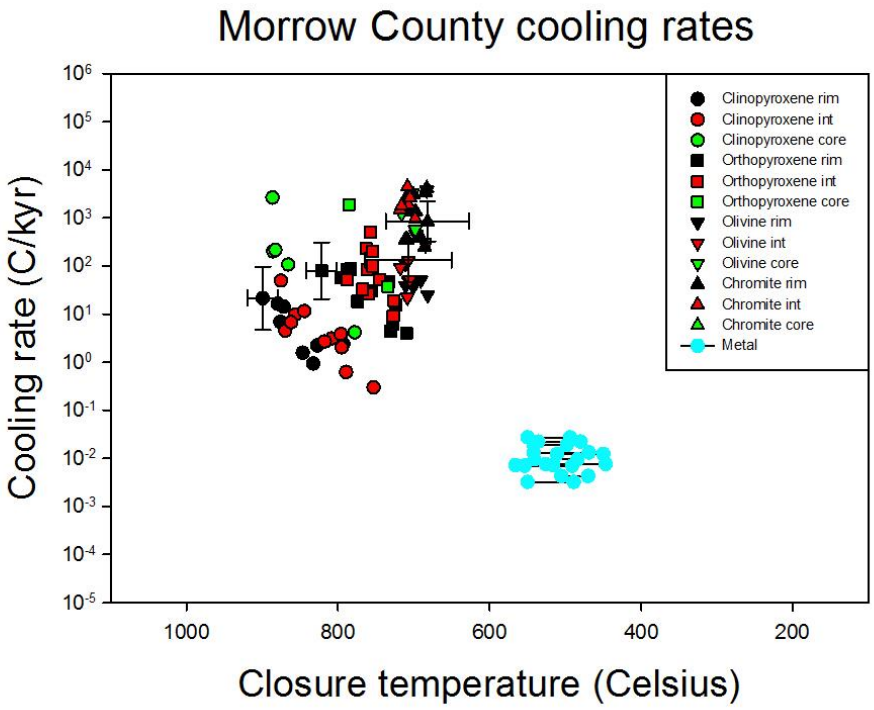
Morrow County cooling rates
Cooling rate (C/kyr)
10^6
10^5
10^4
10^3
10^2
10^1
10^0
10^{-1}
10^{-2}
10^{-3}
10^{-4}
10^{-5}
1000
800
600
400
200
Closure temperature (Celsius)
Clinopyroxene rim
Clinopyroxene int
Clinopyroxene core
Orthopyroxene rim
Orthopyroxene int
Orthopyroxene core
Olivine rim
Olivine int
Olivine core
Chromite rim
Chromite int
Chromite core
Metal

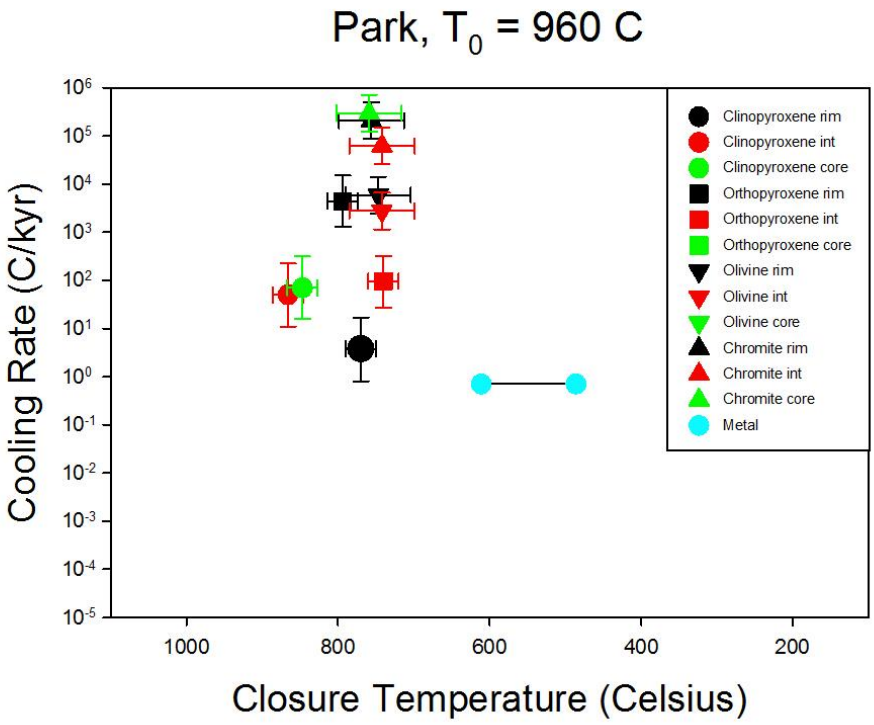
Park, T_0 = 960 C
Cooling Rate (C/kyr)
10^6
10^5
10^4
10^3
10^2
10^1
10^0
10^{-1}
10^{-2}
10^{-3}
10^{-4}
10^{-5}
1000
800
600
400
200
Closure Temperature (Celsius)
Clinopyroxene rim
Clinopyroxene int
Clinopyroxene core
Orthopyroxene rim
Orthopyroxene int
Orthopyroxene core
Olivine rim
Olivine int
Olivine core
Chromite rim
Chromite int
Chromite core
Metal

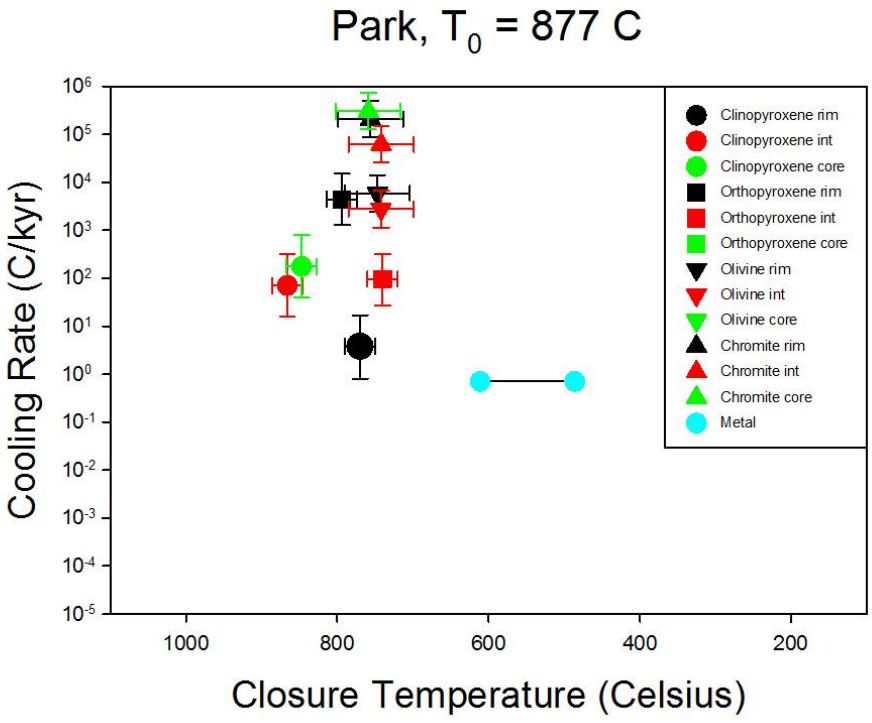
Park, T_0 = 877 C
Cooling Rate (C/kyr)
10^6
10^5
10^4
10^3
10^2
10^1
10^0
10^{-1}
10^{-2}
10^{-3}
10^{-4}
10^{-5}
1000
800
600
400
200
Closure Temperature (Celsius)
Clinopyroxene rim
Clinopyroxene int
Clinopyroxene core
Orthopyroxene rim
Orthopyroxene int
Orthopyroxene core
Olivine rim
Olivine int
Olivine core
Chromite rim
Chromite int
Chromite core
Metal

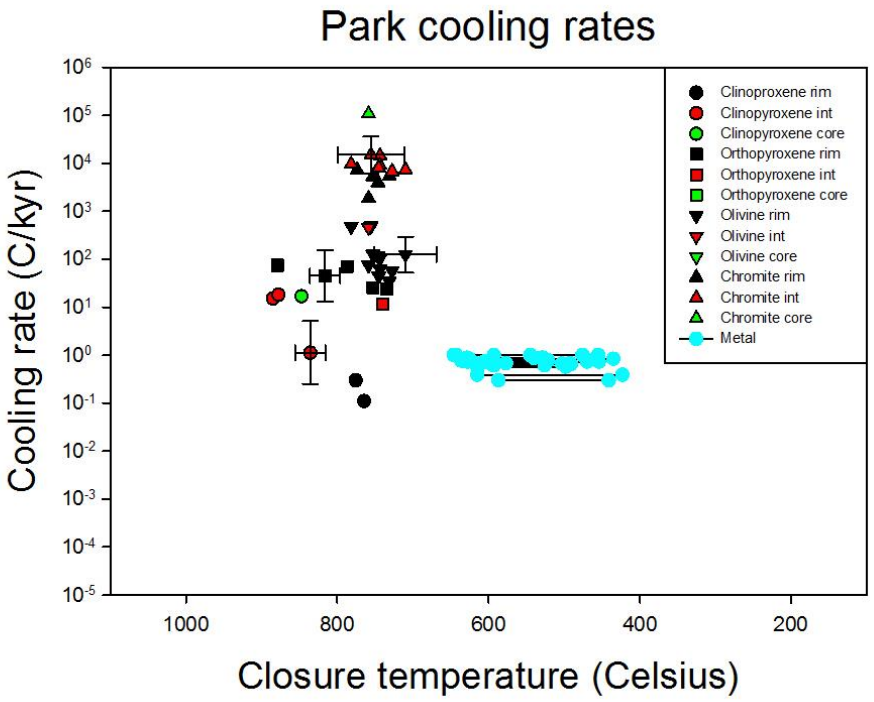
Park cooling rates
Cooling rate (C/kyr)
Closure temperature (Celsius)
Clinoproxene rim
Clinopyroxene int
Clinopyroxene core
Orthopyroxene rim
Orthopyroxene int
Orthopyroxene core
Olivine rim
Olivine int
Olivine core
Chromite rim
Chromite int
Chromite core
Metal

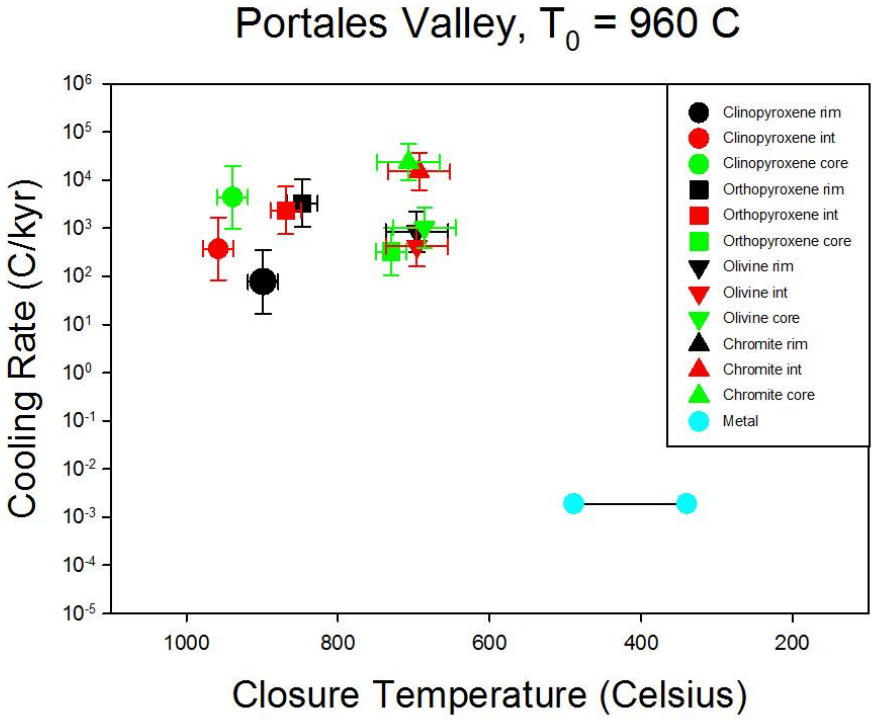
Portales Valley, T0 = 960 C
Cooling Rate (C/kyr)
Closure Temperature (Celsius)
Clinopyroxene rim
Clinopyroxene int
Clinopyroxene core
Orthopyroxene rim
Orthopyroxene int
Orthopyroxene core
Olivine rim
Olivine int
Olivine core
Chromite rim
Chromite int
Chromite core
Metal

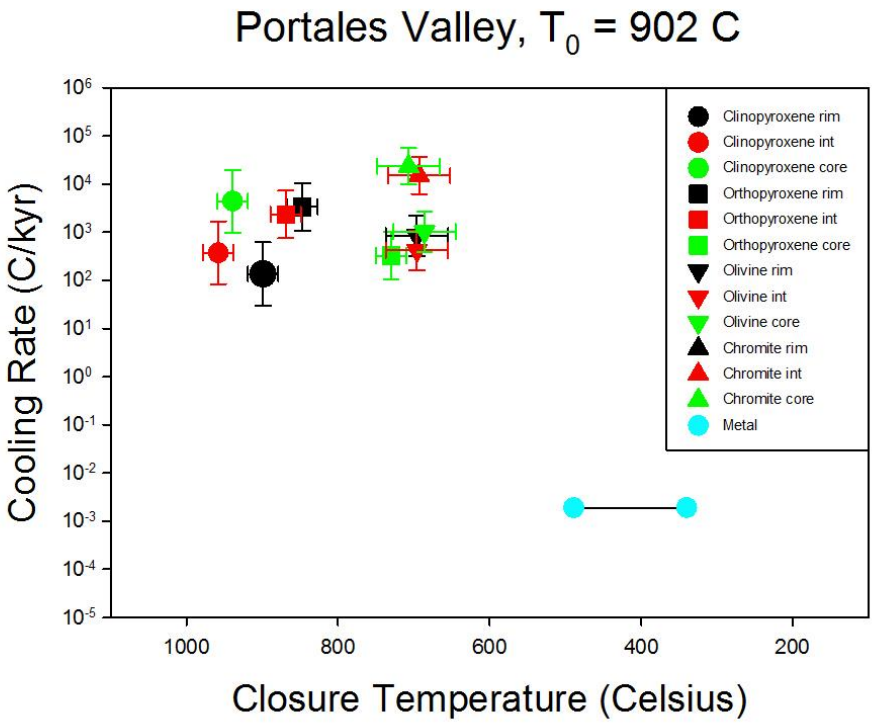
Portales Valley, T_0 = 902 C
Cooling Rate (C/kyr)
Closure Temperature (Celsius)
Clinopyroxene rim
Clinopyroxene int
Clinopyroxene core
Orthopyroxene rim
Orthopyroxene int
Orthopyroxene core
Olivine rim
Olivine int
Olivine core
Chromite rim
Chromite int
Chromite core
Metal

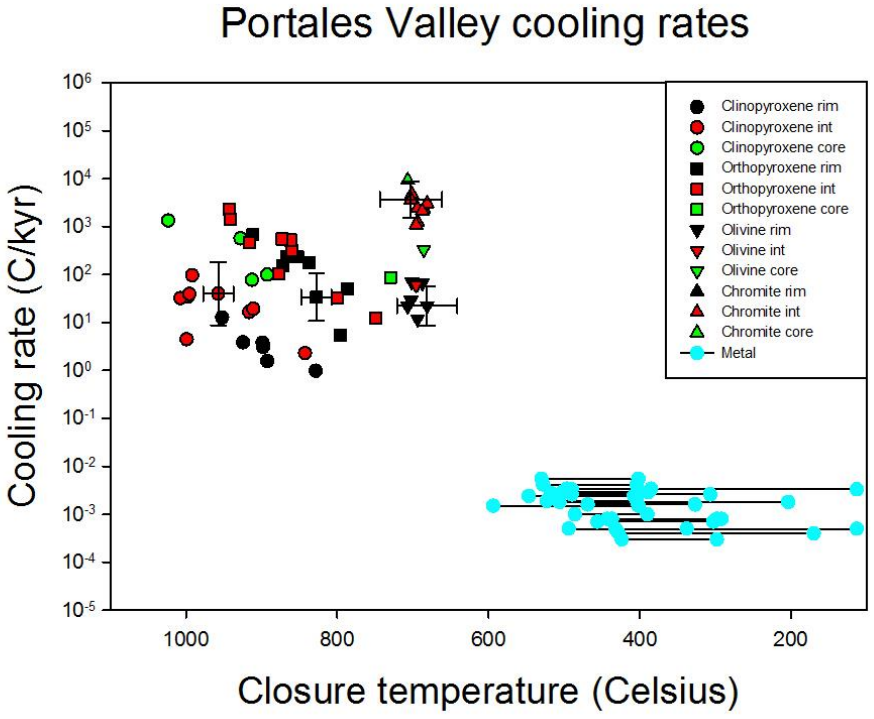
Portales Valley cooling rates
Cooling rate (C/kyr)
Closure temperature (Celsius)
Clinopyroxene rim
Clinopyroxene int
Clinopyroxene core
Orthopyroxene rim
Orthopyroxene int
Orthopyroxene core
Olivine rim
Olivine int
Olivine core
Chromite rim
Chromite int
Chromite core
Metal

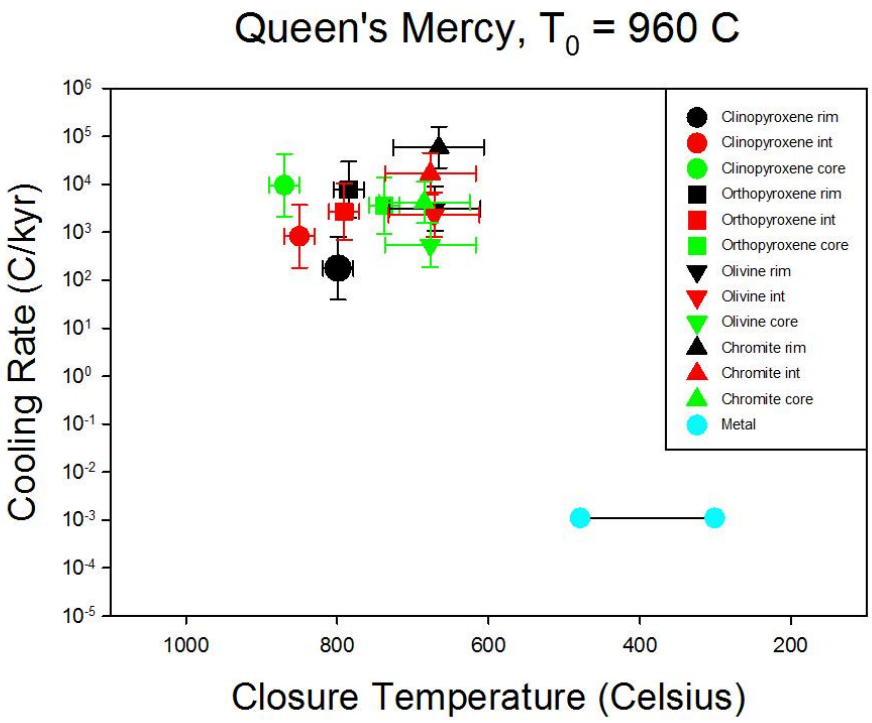
Queen's Mercy, T_0 = 960 C
Cooling Rate (C/kyr)
10^6
10^5
10^4
10^3
10^2
10^1
10^0
10^{-1}
10^{-2}
10^{-3}
10^{-4}
10^{-5}
1000
800
600
400
200
Closure Temperature (Celsius)
Clinopyroxene rim
Clinopyroxene int
Clinopyroxene core
Orthopyroxene rim
Orthopyroxene int
Orthopyroxene core
Olivine rim
Olivine int
Olivine core
Chromite rim
Chromite int
Chromite core
Metal

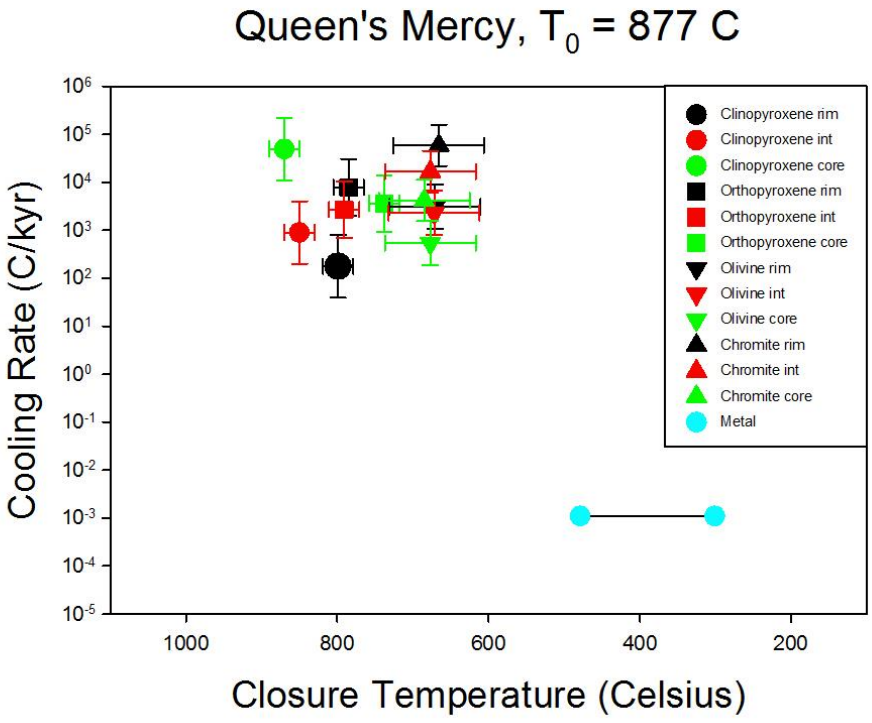
Queen's Mercy, T_0 = 877 C
Cooling Rate (C/kyr)
10^6
10^5
10^4
10^3
10^2
10^1
10^0
10^{-1}
10^{-2}
10^{-3}
10^{-4}
10^{-5}
1000
800
600
400
200
Closure Temperature (Celsius)
Clinopyroxene rim
Clinopyroxene int
Clinopyroxene core
Orthopyroxene rim
Orthopyroxene int
Orthopyroxene core
Olivine rim
Olivine int
Olivine core
Chromite rim
Chromite int
Chromite core
Metal

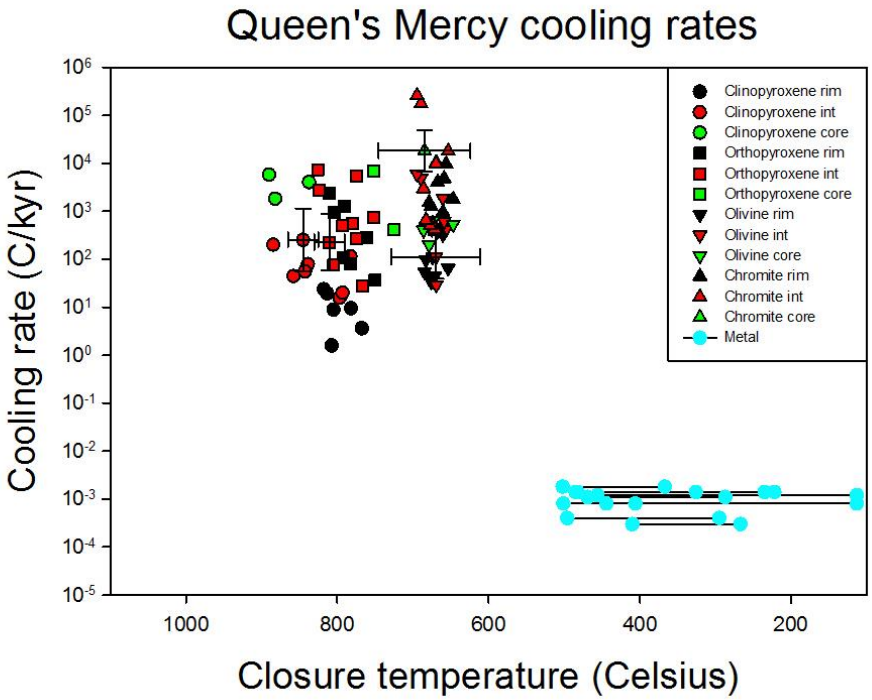
Queen's Mercy cooling rates
Cooling rate (C/kyr)
Closure temperature (Celsius)
Clinopyroxene rim
Clinopyroxene int
Clinopyroxene core
Orthopyroxene rim
Orthopyroxene int
Orthopyroxene core
Olivine rim
Olivine int
Olivine core
Chromite rim
Chromite int
Chromite core
Metal

APPENDIX H: Pyroxene zoning plots

This appendix contains plots showing variation in enstatite and wollastonite content (as normalized using the Nakamuta et al. (2017) formulation) in orthopyroxene and clinopyroxene with the distance from the grain rim for each spot datum. Percentages are given as from the normalized pyroxene ternary, e.g. $Enstatite = 100 * \frac{En}{En+Fs+Wo}$.

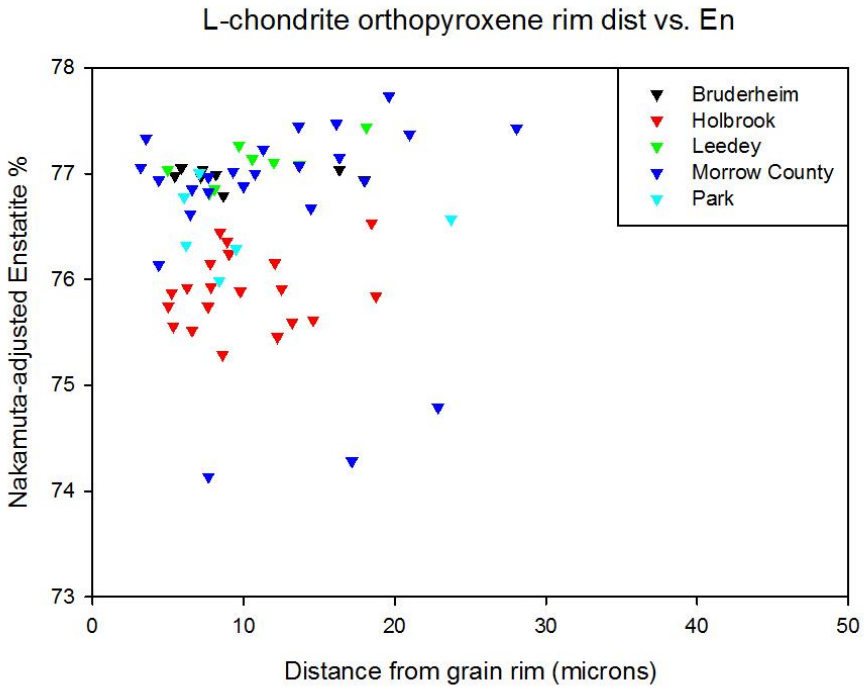

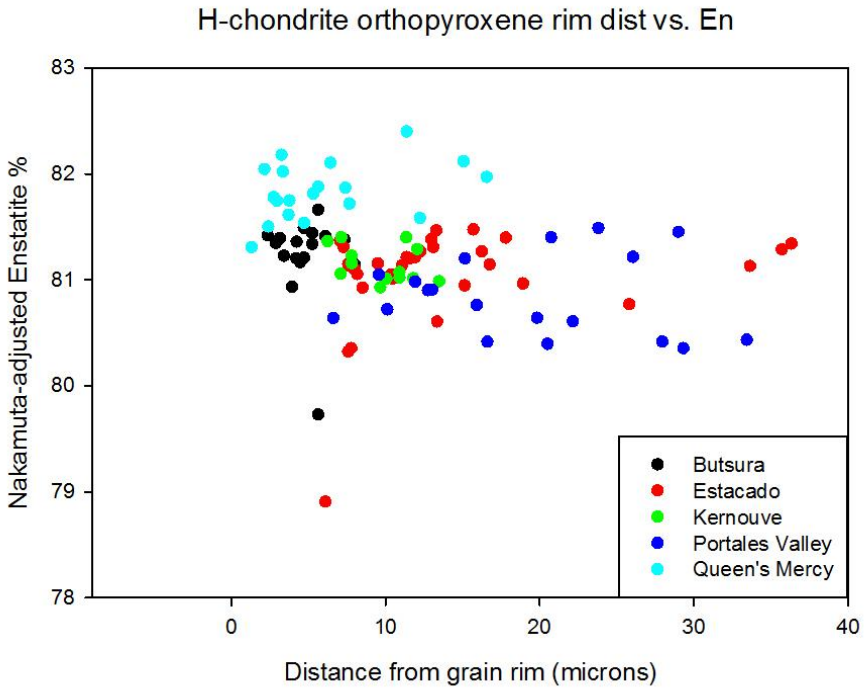
H-chondrite orthopyroxene rim dist vs. En
Nakamuta-adjusted Enstatite %
83
82
81
80
79
78
0
10
20
30
40
Distance from grain rim (microns)
Butsura
Estacado
Kernouve
Portales Valley
Queen's Mercy

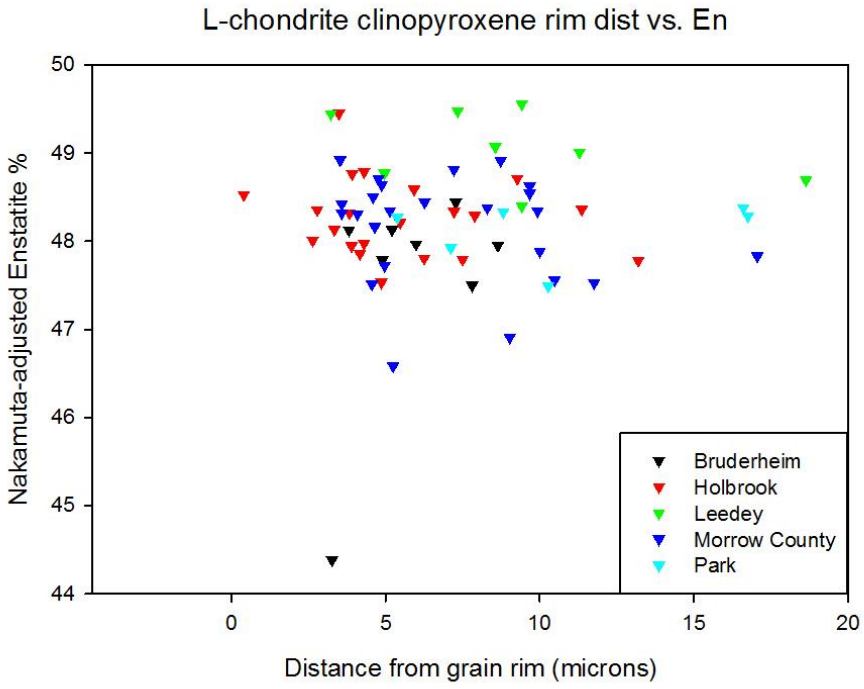
L-chondrite clinopyroxene rim dist vs. En
Nakamuta-adjusted Enstatite %
50
49
48
47
46
45
44
0
5
10
15
20
Distance from grain rim (microns)
Bruderheim
Holbrook
Leedey
Morrow County
Park

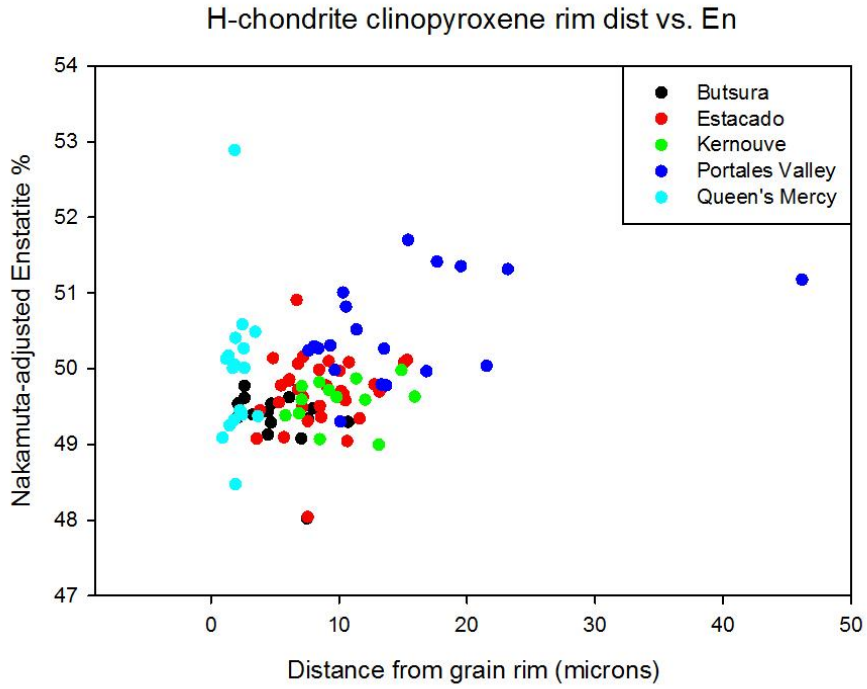
H-chondrite clinopyroxene rim dist vs. En
Nakamuta-adjusted Enstatite %
Distance from grain rim (microns)
Butsura
Estacado
Kernouve
Portales Valley
Queen's Mercy
54
53
52
51
50
49
48
47
0
10
20
30
40
50

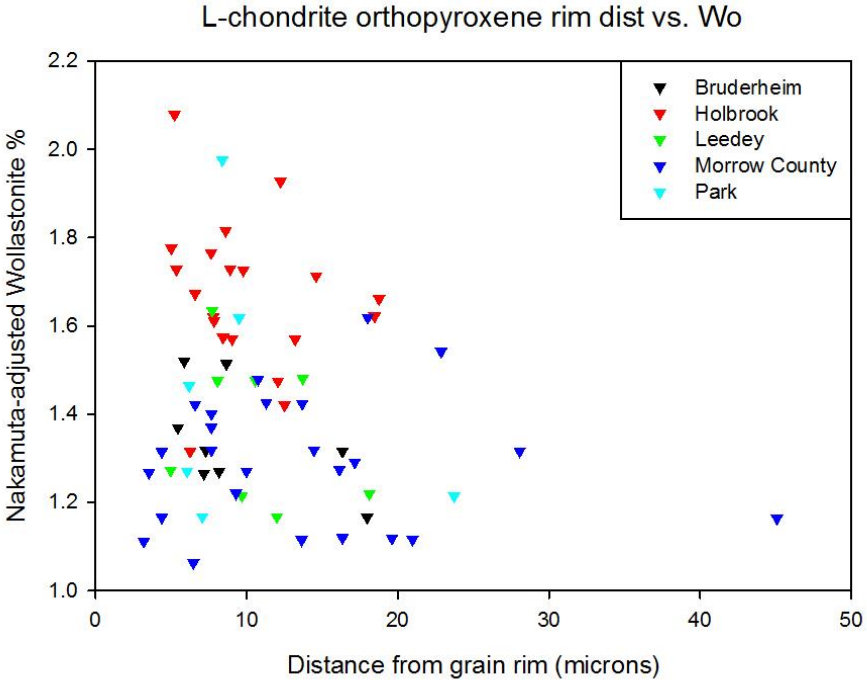
L-chondrite orthopyroxene rim dist vs. Wo
Nakamuta-adjusted Wollastonite %
Distance from grain rim (microns)
Bruderheim
Holbrook
Leedey
Morrow County
Park
2.2
2.0
1.8
1.6
1.4
1.2
1.0
0
10
20
30
40
50

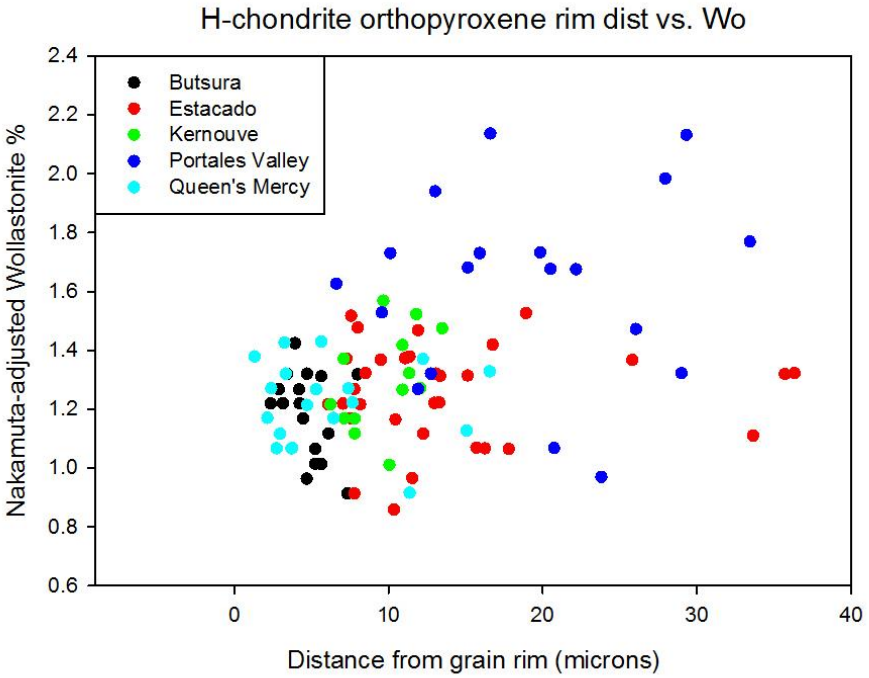
H-chondrite orthopyroxene rim dist vs. Wo
Butsura
Estacado
Kernouve
Portales Valley
Queen's Mercy
Nakamuta-adjusted Wollastonite %
Distance from grain rim (microns)
2.4
2.2
2.0
1.8
1.6
1.4
1.2
1.0
0.8
0.6
0
10
20
30
40

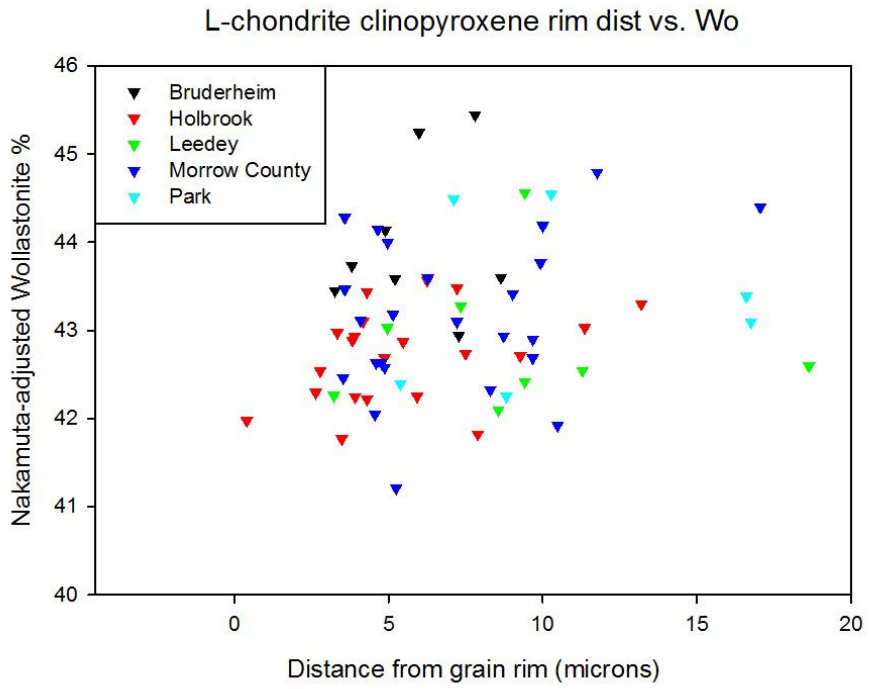
L-chondrite clinopyroxene rim dist vs. Wo
Bruderheim
Holbrook
Leedey
Morrow County
Park
Nakamuta-adjusted Wollastonite %
Distance from grain rim (microns)
46
45
44
43
42
41
40
0
5
10
15
20

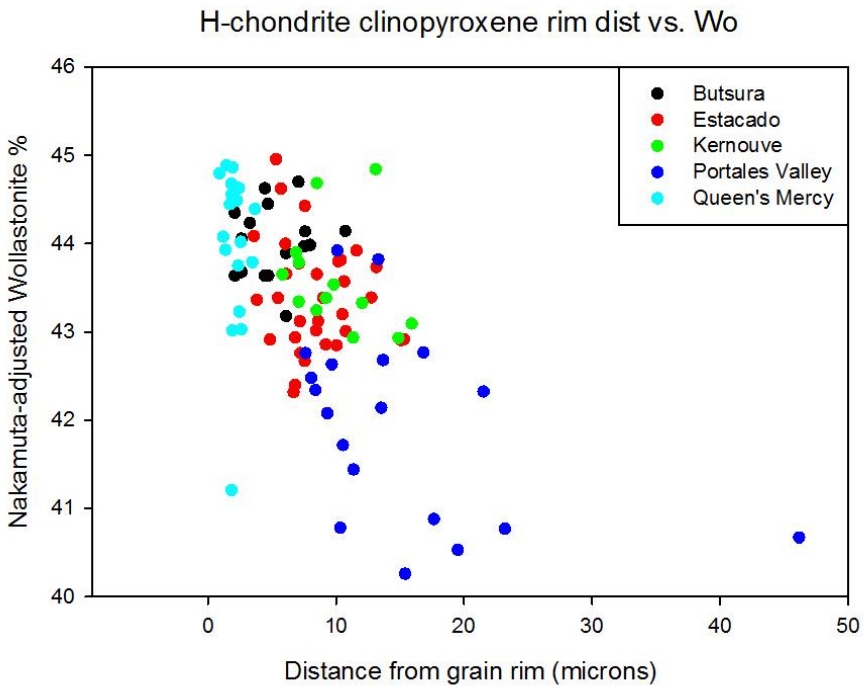
H-chondrite clinopyroxene rim dist vs. Wo
Nakamuta-adjusted Wollastonite %
Distance from grain rim (microns)
Butsura
Estacado
Kernouve
Portales Valley
Queen's Mercy
46
45
44
43
42
41
40
0
10
20
30
40
50